METAL-ASSISTED GROWTH OF III-V NANOWIRES BY MBE

METAL-ASSISTED GROWTH OF III-V NANOWIRES BY MOLECULAR BEAM EPITAXY

By

MARTIN CHARLES PLANTE, B.Appl.Sc., M.Sc.

A Thesis
Submitted to the School of Graduate Studies
in Partial Fulfilment of the Requirements
for the Degree
Doctor of Philosophy

McMaster University

DOCTOR OF PHILOSOPHY (2009) McMaster University
(Department of Engineering Physics) Hamilton, Ontario

TITLE: Metal-Assisted Growth of III-V Nanowires by Molecular Beam Epitaxy
AUTHOR: Martin Charles Plante, B.Appl.Sc., M.Sc. (Université Laval)
SUPERVISOR: Dr. Ray R. LaPierre
NUMBER OF PAGES: xviii, 171

Abstract

The mechanisms operating during the metal-assisted growth of III-V nanowires (NWs) by molecular beam epitaxy on (1 1 1)B substrates were investigated through a series of experiments aimed at determining the influence of growth conditions on the morphology and crystal structure. Using GaAs as the principal material system for these studies, it is shown that a good control of these two characteristics can be achieved via a tight control of the temperature, V/III flux ratio, and Ga flux. Low and intermediate growth temperatures of 400°C and 500°C resulted in a strongly tapered morphology, with stacking faults occurring at an average rate of 0.1 nm^{-1}. NWs with uniform diameter and the occurrence of crystal defects reduced by more than an order of magnitude were achieved at 600°C, a V/III flux ratio of 2.3, and a Ga impingement rate on the surface of 0.07 nm/s, and suggest the axial growth is group V limited. Increasing the flux ratio favored uniform sidewall growth, thus making the process suitable for the fabrication of core-shell structures. Further observation of steps on the sidewall surface of strongly tapered NWs suggests that radial growth of the shell proceeds in a layer-by-layer fashion, with the edge progressing in a step-flow mode toward the tip.

From the experimental considerations, an analytical description of the growth is proposed, based on a simple material conservation model. Direct impingement of growth species on the particle, coupled to their diffusion from the sidewall and the substrate surface, are considered in the derivation of expressions for the time evolution of both axial and radial growths. Factors that take into account the non-unity probability of inclusion of group III adatoms in the axially growing crystal are introduced. Moreover, a step-mediated growth is included to describe the axial evolution of the shell.

Acknowledgements

I am greatly indebted to my friend and, during business hours, supervisor Dr. Ray LaPierre. When I decided to embark on this crazy Ph.D. adventure, he did not hesitate one second to take me under his wing and guide me through a field full of unknowns. This was not always easy, but his dedication and patience were truly inspiring, and without his constant support this thesis would have never seen the day. Many thanks also go to the members of my supervisory committee, Drs. Adrian Kitai and Gianluigi Botton, who patiently reviewed my progress along the way, and provided valuable advice.

Such an endeavour is of course not a one-person effort, and without the help of the research engineers and technical people keeping the laboratories running, it would be an impossible task. I am most extremely grateful to Dr. Brad Robinson, who fabricated all my MBE samples, and taught me a great deal about this fascinating growth technique. His in-depth knowledge on various technological (and a bunch of other!) topics, coupled to a committed enthusiasm toward trying new things, forced me to always think outside of the box (I know it sounds so cliché, but I could not find another formulation), and make "strategic" decisions in planning my various experiments. A big "thank you" to the CEDT staff: Doris, Graham, Zhilin, and Linda, for making my life easier on so many instances. A significant part of my research time was spent doing electron microscopy, and I want to thank all the people at the CCEM for their precious help and their generosity in teaching me how to work these instruments out: Glynis, Steve, Fred, Christian, Andy, Chris, and Julia. Many thanks also go to the administrative staff within the department of Engineering Physics: Marilyn, and Fran, who were always there to help when I needed assistance.

I would have probably gone insane a long time ago if it was not for the fantastic people I met over these years. First and foremost, Hanna, my first labmate with whom I formed the original version of "Team LaPierre": I am so grateful for your friendship, my "little Hannabanana". To my colleagues, who over time also became my friends: Chris (and Ashley), Subir, Parsian, Nuzhat, I am simply lucky to have found you on my way. My deepest thanks and appreciation are extended to my long standing friends: Amanda, Grant, Malca, Mike (!!!). Thanks for all your support and encouragements; you guys (and gals) are the best, and I feel privileged to have such friends.

I was very fortunate to be able to count on the love and support of my mother: thank you for believing in me when I announced I was going back to school at the age of 32. Your trust was elemental in going through all this. (*Merci maman, pour simplement avoir cru en moi, et ce sans aucune restriction, lorsque je t'ai annoncé que je retournais à l'école à l'âge de 32 ans. Je n'aurais pas pu passer au travers de tout ça sans ta confiance et tes encouragements.*) Thanks also to my brother Nicolas and my sister-in-law Annik. (*They don't need the translation!!! hehehe...*)

Finally, I would like to thank the department of Engineering Physics at McMaster University, the Ontario Graduate Scholarships, the Natural Sciences and Engineering Research Council of Canada, and the Ontario Photonics Consortium for the financial support they provided, and which allowed me to devote myself completely to my research.

to my father

Table of Contents

List of Figures

List of Tables

Chapter 1

Background

The growth of crystals is a very captivating area of solid state physics, not only requiring a thorough understanding of thermodynamic and kinetic theories, but also an extensive experience with the fabrication apparatus. Finding the "right recipe" (i.e., the proper combination of growth conditions) in order to obtain the desired structure can often prove to be challenging. The discovery of a new growth mechanism therefore constitutes a major milestone, as it pushes the discipline forward and opens up new opportunities. This is precisely the case of the Vapour-Liquid-Solid (VLS) mechanism, a vapour-based process developed in the early 1960's for the growth of whisker crystals initiated from metal seed particles. Close to fifty years after its inception, it is now deemed, along with its derived techniques, to be the most successful mode to generate large quantities of nanowires (NWs) with single crystalline structures [1].

In this chapter, the reader will be provided with an introduction on the various aspects related to the fabrication of semiconductor NWs. After a brief historical review in Section 1.1, the emphasis is put on the description of the metal-assisted growth technique in Section 1.2. The motivation behind the present work is then presented in Section 1.3, where the scope of the study is also defined. We finally conclude in Section 1.4 by giving an overview of the topics that will be treated in this thesis.

1.1 From Whiskers to Nanowires

A whisker is defined as any material, metallic or non-metallic, that is: (a) a single crystal, and (b) of an elongated filamentary form, with a minimum length to maximum average transverse dimension ratio of at least 10:1 [2]. Initially meant to describe structures having a maximum cross-sectional area of 5.1×10^{-4} cm^2 (corresponding to a circular cross-section of $\sim$250 μm in diameter), the primary interest of such crystals resided in their ultra-high strength (on the order of 1 million psi) compared to their bulk counterpart [2]. Their role as strengthener in the elaboration of various composite materials, in which they can act as the principal load bearing element [3], was a major area of research and development as early as the late 1940's. In the same time period, the first semiconductor whiskers were synthesized by a group at DuPont, who used the reduction of $SiCl_4$ with Zn vapour to produce high purity Si crystals that were 250 μm in diameter and 1 cm in length [4]. A few years later, Johnson and Amick refined the previous procedure by diluting the silicon tetrachloride with a carrier gas (such as argon or hydrogen), which resulted in structures of 1 μm in diameter (while the length was maintained at 1 cm) [5].

Prior to the 1960's, one of the models widely used to describe the crystal growth from the vapour phase was based on the presence of an initial dislocation at the growth surface. In a paper dated from 1949, Frank laid the foundations of a theory [6] that was to be developed in greater details two years later [7]. It was then proposed that the growth of crystals under the relatively low supersaturations experimentally attainable could only be explained on the basis of the inherent imperfections of surfaces. A "screw dislocation" (i.e., a dislocation that has a component of displacement vector normal to the crystal face at which it emerges, as schematically represented in Figure 1.1) was thus deemed to provide a self-perpetuating step for the addition of new

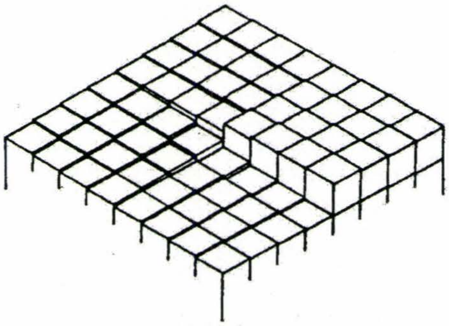

Figure 1.1: Representation of a screw dislocation emerging normally at the face of a simple cubic crystal. (Adapted from [6].)

layers, without the need for "fresh" two-dimensional (2D) nucleation events, and to result in elongated crystals, due to an enhanced growth in the direction of the defect.

This mechanism was widely accepted initially, as various experimental observations supported its assertions [8–10]. Detailed analytical solutions for the growth rate (length of the whisker as a function of deposition time) and supersaturation ratio as a function of whisker length were derived by Blakely and Jackson [11], while Ruth and Hirth were the first to treat the diffusion of growth species from the substrate surface as a direct contribution to the axial growth [12]. The universality of the dislocation-mediated growth was however questioned in the late 1950's, following the work from Webb and co-workers [13], who found evidence of a single axial dislocation in only one out of nine different materials studied. Subsequent investigations were undertaken by Wagner and his collaborators at Bell Laboratories on Si whiskers grown by chemical vapour deposition (CVD) process [14–16], which further emphasized that other mechanisms could be at the origin of such structures. Originating from micron-size Au "impurities" placed on a Si {1 1 1} substrate, filamentary crystals grew perpendicular to the heated surface from the reaction of the precursor (mixture of hydrogen and $SiCl_4$) with the impurity droplets that formed on the surface upon heating. Post growth-characterization not only revealed the absence of any axial dislocation, but also the presence of a "liquid-like" globule at the tip of the crystals. These pioneering efforts laid the foundations for the now well-established VLS mechanism, which is at the heart of the current work, and will be further described in the next section.

Following the fundamental contributions by Givargizov and co-workers in the 1970's [17,18], who provided the first exhaustive VLS analytical description, it is only twenty years later that an interest in the mechanism was again generated. A team at Hitachi led by Kenji Hiruma then reported on the first nanometer-scale (10-200 nm in diameter) semiconductor whiskers, now known as NWs, grown by VLS [19, 20]. For the major part of the 1990's, their work on III-V materials provided insightful information, notably on the crystal structure of the NWs [21,22], revealing transitions from zincblende to wurtzite. Furthermore, they demonstrated the practical aspects of such structures, highlighting the optical properties of p-n junctions incorporated in the NWs [23]. A few years later Westwater and co-workers were the first to report on VLS-grown Si NWs by CVD, this time using silane gas (SiH_4) diluted with 10% helium [24]. Structure as thin as 10 nm in diameter were obtained. Their study further revealed a strong relationship between the NW morphology (in particular the presence of kinks) and the growth conditions (temperature, silane partial pressure). In the late 1990's/early 2000's, two major research groups emerged in the field of NW fabrication: one from Harvard University, supervised by Charles Lieber, and another one from Lund University (Sweden), led by Lars Samuelson. Both played (and continue to play to this day) a major role in the developmental aspects of VLS technology, from fundamentals to applications [25–36].

Other approaches have been developed to fabricate NWs, such as templated substrates, growth from solution, and oxide-assisted growth, but these will not be discussed in details within the framework of this thesis. The interested reader could refer to the excellent topical review paper by Xia and co-workers [37], or the more recent one by Wang and co-workers [38].

1.2 Crystal Growth from Metal Seed Particles

1.2.1 Qualitative Description

Wagner and Ellis were the first to describe, in the early 1960's, the filamentary growth of crystals via a novel theory [14] that diverged from the more classical vapour-solid (VS) approach that prevailed until then, and which was described in the preceding section. Their VLS mechanism emphasizes the role of metallic "impurities" on the substrate surface as precursors for the preferential deposition of growth species. In the process, the surface is heated, thus inducing the impurities to alloy and liquefy. The effect of a liquid phase (layer or droplets) on the surfaces of crystals growing from the vapour was not totally unknown in the middle of the 20th century. Already in 1955 (almost a decade before the first report on VLS), Brewer and Kane [39] reported that the evaporation rate of a given material (phosphorous and arsenic in this case) increased significantly when a liquid (thallium) was covering the evaporation surface (vapour pressures 30 times greater than the ones measured without the liquid catalyst). As was mentioned previously, solidified globules had also been observed at the tips of certain whiskers (Al_2O_3 [10], BeO [40]), but without a clear understanding of their nature, let alone of the mechanisms at their origin. The initial VLS model, as schematically depicted in Figure 1.2, is therefore based on a liquid layer (resulting from the alloying of the metallic particle, i.e., the "impurity", with the substrate and the surrounding vapour) situated between the vapour and the growing crystal (hence the name Vapour-Liquid-Solid) that has a large accom-

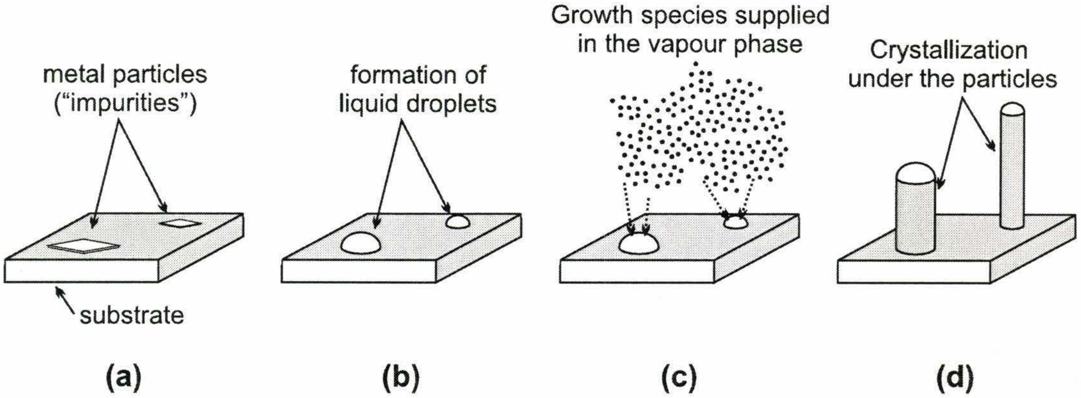

Figure 1.2: Illustration of the VLS mechanism. (a) "Impurities" (metallic particles) are initially present on a substrate surface. (b) The system is heated above the eutectic temperature to form the liquid alloy droplets. (b) Atoms directly supplied from the vapour phase get preferentially deposited on the liquid droplets. (IV) Supersaturation of the liquid causes precipitation at the liquid-solid interface, and crystal growth follows.

modation coefficient compared to the surrounding materials, and therefore becomes a preferred site for deposition. As growth species are continually supplied from the vapour on the surface of the substrate, the liquid becomes eventually supersaturated, and nucleation occurs at the liquid-solid interface as a result of precipitation. The radial size of the resulting crystal is dictated by the size of the liquid droplet, while the length primarily depends on the growth duration.

Various requirements for the selection of metal particle were initially established for the VLS mechanism to operate [16]. First and foremost, it must be possible for the selected metallic agent to form a solution at the deposition temperature with the crystalline material to be grown. The vapour pressure of the agent over the liquid alloy must also be relatively small. This is motivated by the desire to have a good size and shape uniformity of the crystal grown: evaporation of the seed particle material would not necessarily change the composition, but would change the droplet volume, and therefore the cross section of the liquid-solid interface (and of the crystal). Moreover, the wetting characteristics of the liquid alloy, arising from the different interfacial energies (vapour-solid, vapour-liquid, liquid-solid), will also have a direct influence on the shape of the growing crystal. Finally, the particle material and the deposition temperature must be chosen to avoid the formation of an intermediate solid phase of the particle with one of the constituents of the vapour.

The liquid phase of the seed particle as the growth proceeds has been the topic of some debates in recent years. Using *in-situ* energy dispersive X-ray spectrometry (EDX) to measure the composition of heated particles, Persson and co-workers were the first to postulate a vapour-solid-solid (VSS) mechanism operating during the Au-assisted growth of GaAs NWs by chemical beam epitaxy (CBE) [34]. Conflicting results have even been reported by different groups studying the same material system (InAs initiated from Au seed particles) and using similar growth apparatus (metal-organic vapour phase epitaxy (MOVPE)). Via an argument based on the temperature dependence of the NW growth rate, Dick and co-workers concluded that growth occurs only within a range where the particle forms a solid alloy with the supplied In [35,41], while Dayeh and co-workers did not find any evidence of the VSS mechanism, attributing the difference in the growth rate and cessation temperature to the variation in the input V/III flux ratio, as opposed to the difference in the melting temperatures of the Au-In particle alloy at the tip of the NW [42].

The description of the VLS mechanism is now completed by discussing the growth direction of the crystals. It is well known, and was even recognized at the initial stage, that Si whiskers/NWs synthesized by the VLS mechanism grow in the $\langle 1\ 1\ 1 \rangle$ direction [16,24,43,44]. This has an importance in the selection of the substrate for the case of epitaxial growth of whiskers/NWs, as their orientation on the surface (i.e., the angle they make with the normal to the latter) will be a direct consequence of that choice. Interestingly, the growth direction appears to depend on the growth

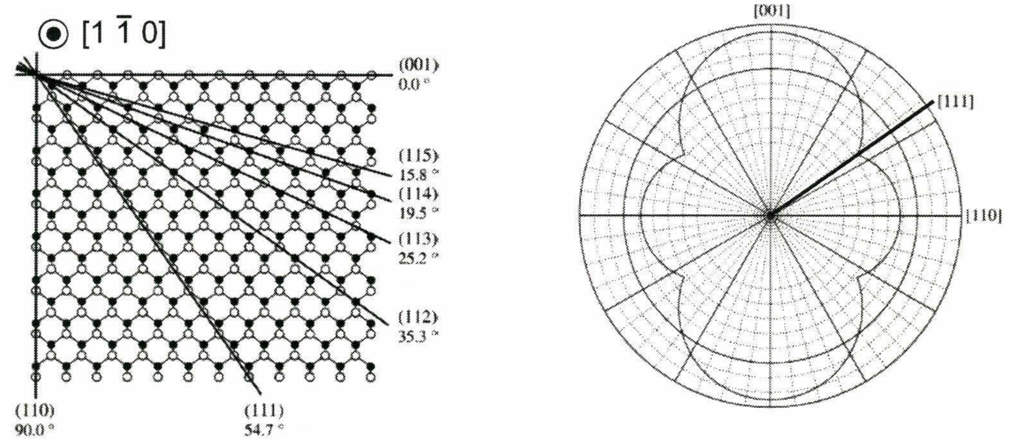

(a) (b)

Figure 1.3: An explanation for the preferential growth orientation of the NWs. (a) 2D illustration of some planes of the zincblende crystal structure. (b) Polar plot of the surface free energy, obtained by counting the areal density of broken bonds when the crystal is cut perpendicularly to the respective orientation. The light dotted circles represent the level of surface free energy, the radial lines the directions, and the "flower-like" curve is the calculated surface free energy. (Adapted from [47])

method: the same silicon NWs, grown by oxide-assisted laser ablation technique [45], are mainly oriented along the $\langle 1\ 1\ 2 \rangle$ direction, sometimes the $\langle 1\ 1\ 0 \rangle$ one, but never $\langle 1\ 1\ 1 \rangle$. In a model proposed by Tan and co-workers, the role of specific dislocations is emphasized (along with surface stability) to explain this "preference" [46]. This proposal is along the same lines as the screw dislocation mechanism introduced in the previous section, but in this case the dislocation was just assumed, and its presence was not verified experimentally. Another simple, yet effective, approach consists in counting the areal density of broken bonds to determine the surface free energy of particular planes of the zincblende crystal structure [47]. From the polar representation of the surface free energy shown in Figure 1.3b, it can be seen that the latter is minimum in the case where the growth front of the crystal is parallel to the (1 1 1) face.

1.2.2 Review of Models

The qualitative description of the metal-assisted growth presented above is here further substantiated through a review of some of the major theoretical models that have been proposed over the years.

1.2.2.1 Wagner and Ellis

In the original kinetic treatment proposed by Wagner and Ellis [16], and illustrated in Figure 1.2, the process occurs in two basic steps: deposition of growth species from the vapour phase directly on a liquid solution, followed by precipitation from the supersaturated solution at the liquid-solid interface. From the kinetic theory of gases, the condensation flux J (in atoms/unit area/unit time) can be estimated as:

$$J = \frac{\alpha \sigma p_o}{\sqrt{2\pi mkT}}, \tag{1.1}$$

where k is the Boltzmann constant (8.62×10^{-5} eV/K), α is the accommodation (or sticking) coefficient (i.e., the probability that an impinging atom is adsorbed regardless of where it strikes on a surface [48]), and σ the supersaturation of the vapour (defined as $(p - p_o)/p_o$, with p being the vapour pressure and p_o the equilibrium vapour pressure at the temperature T). The authors thus proposed that, since the value of α depends on the perfection of the surface and the supersaturation σ, for perfect (defect-free) and imperfect (i.e., with screw dislocations) crystal surfaces the accommodation would be equal to zero below a certain critical supersaturation (i.e., $J = 0$ when $\sigma < \sigma_c$, as shown in Figure 2 of reference [16]). In the case of a clean liquid surface, the unity accommodation ($\alpha = 1$) would result from its "ideal roughness": following a theory elaborated by Hirth and Pound [49,50], this type of surface can be assimilated to a series of steps and ledges that are only interatomic distances apart, so accommodation sites exist over its entire area. In sum, the filamentary morphology of the crystals growing in the VLS mechanism occurs due to the preferential accommodation of impinging atoms on the liquid droplets. Note that, while being a good qualitative argument to explain the experimental observations, the assumption $\alpha = 1$ for the liquid is not representative of the reality. It is known that the accommodation coefficient on the liquid surface in the case of CVD is significantly less than unity (e.g., 10^{-3} for Si and Ge). However, this value is still larger than the accommodation coefficient on the crystal surface (e.g., 10^{-5} for Si and Ge) [51].

Having a liquid phase of the seed particle is however not sufficient for the VLS mechanism to operate. An essential condition is that the liquid solution be stable in its own vapour. This translates into a limitation on the minimum diameter of the crystal (whisker) that is to be grown. As previously mentioned, the latter depends strongly on the size of the liquid droplet. Assuming a spherical droplet of radius R, the minimum critical radius R_{min} is given by (Gibbs-Thomson relation):

$$R_{min} = \frac{2\gamma_{LV}\Omega}{kT\ln\sigma}, \tag{1.2}$$

where γ_{LV} is the surface tension at the liquid-vapour interface, Ω is the atomic volume of the crystal species in the droplet, and σ is the supersaturation defined earlier. According to this expression, stable droplets at the sub-micron scale can be achieved by an appropriate increase in supersaturation of all components of the liquid.

1.2.2.2 Givargizov-Chernov Model

Following on the footsteps of Wagner and Ellis, Givargizov and Chernov (GC) conducted in the early 1970's a thorough study on the kinetics of Si whiskers grown by VLS using CVD [17, 18]. Emphasis was then placed on the dependence of the growth rate on the whisker diameter and the role of the liquid phase in the process. They derived their model by combining the Gibbs-Thomson equation and some of the well established kinetic laws of growth.

Their experiments led to the observation of two major elements. First, as was expected from the model derived by Wagner and Ellis, whiskers with a diameter below a critical value did not grow. Second, a drastic decrease of the growth rate occurred as the whisker radius decreased. These indicate an increasing vapour pressure and lowered solubility of the material deposited (Si) as the whisker diameter becomes smaller (the Gibbs-Thomson effect). In this model, the driving force for crystallization is the vapour supersaturation $\Delta\mu/(kT)$, with $\Delta\mu$ being the effective difference between the chemical potential of whisker material in the vapour phase and in the whisker crystal. Accounting for the Gibbs-Thomson effect for a whisker of radius R, the latter is defined as:

$$\Delta\mu = \Delta\mu_o - \frac{2\Omega\gamma_{VS}}{R}, \tag{1.3}$$

where $\Delta\mu_o$ is the effective difference between the chemical potential of whisker materials in the vapour phase and in the whisker at a plane boundary (i.e., in the case of $R \to \infty$), γ_{VS} the specific free energy of the whisker surface (i.e., the vapour-solid interface). A semi-empirical expression for the whisker axial growth rate dH_w/dt (in unit lenght/unit time), where H_w is the whisker height measured from the substrate surface, was then obtained:

$$\frac{dH_w}{dt} = b\left[\frac{\Delta\mu_o}{kT} - \frac{2\Omega\gamma_{VS}}{kT}\frac{1}{R}\right]^2, \tag{1.4}$$

with b being a kinetic coefficient independent of supersaturation.

The linear dependence of $\sqrt{dH_w/dt}$ with $1/R$ was observed not only in the case of Si, but also for other materials such as Ge, GaAs, SiC, GaP, CdSe, ZnS, and ZnSe. While the value of b can be obtained by measuring the slope of the $\sqrt{dH_w/dt}$ vs. $1/R$ curve (provided γ_{VS} is known), Equation 1.4 also reveals that no growth will occur (i.e., $dH_w/dt = 0$) for whiskers having a radius lower than a critical value R_c:

$$R_c = \frac{2\gamma_{VS}\Omega}{\Delta\mu_o}. \tag{1.5}$$

1.2.2.3 Modern Approaches

The preceding model proposed by Givargizov and Chernov accurately described the observations made on the growth of whiskers in the 1970's, which had diameters in the range of several micrometers. It was then reasonable to assume a polycenter regime of nucleation, i.e., many islands arising in one layer that grow and coalesce to form a continuous monolayer [52]. This might not necessarily be true for NWs having diameters at least two orders of magnitude smaller.

Building on the GC model, Dubrovskii and Sibirev (DS) developed (almost thirty years later) a very detailed and generic expression for the growth rate of the whiskers/NWs growing via the VLS mechanism [52]. These authors were the first to consider that the condensing phase was the liquid, so the driving force of the phase transition in their model is the supersaturation of the liquid alloy (not the vapour). They also took into account both the curvature of the whisker and the droplet, as well as the transition from polynucleation (whisker) to mononucleation (NW). Their treatment includes a comparison of the growth rate of the whisker/NW (via VLS) and the film grown on the non-metal-covered surface (via VS), and demonstrates that the crystal grows faster under the liquid droplet than on the (non-metal-covered) substrate surface due to the lower interfacial energy of the liquid-solid boundary compared to the vapour-solid one. At a given vapour supersaturation, it is therefore "easier" to form the nuclei from the liquid alloy.

In the previous two models (GC and DS), the whisker/NW height H_w increases with the radius. A different behaviour was however observed by Schubert and co-workers on Si NWs seeded by Au particles, and grown by MBE [53]: instead of the expected VLS dependence, they found something closer to $H_w \propto 1/R$. This latter relationship, which was also observed in our early studies on MBE-grown GaAs NWs [54], is typical of the diffusion-induced growth of filamentary crystals [12, 55]. Dubrovskii and co-workers [56], simultaneously to Johansson and co-workers [57], developed analytical expressions describing the NW axial growth rate resulting from both the direct impingement on the seed particle and adatom diffusion from the substrate surface toward the particle, which have the following form:

$$\frac{dH_w}{dt} = A + \frac{B}{R}, \tag{1.6}$$

where A and B are parameters that depend on the growth conditions. Johansson and co-workers even demonstrated in a quantitative manner why the Gibbs-Thomson effect, as included in the GC model, does not operate under certain experimental conditions [57, 58]. In a subsequent publication, Dubrovskii and co-workers further refined the theoretical description by combining the classical adsorption-induced VLS mechanism (i.e., the GC model) with the diffusion-induced nucleation-mediated (at the liquid-solid interface) growths [59]. This unified model was the first to predict a minimum in the H_w vs. R curve (which we were the first to experimentally observe [54]), resulting from the competition between the Gibbs-Thomson effect and the diffusion-induced contributions [60].

1.3 Motivations and Scope of the Research

With the continuing miniaturization of electronic devices, the practical shortcomings of traditional top-down fabrication techniques are becoming more prevalent. Resolution limitations of photolithography (caused by diffraction, reduced depth of field, and even chemistry of photoresists) are pushing the industry to explore new avenues (such as nanoimprinting and parallel processing electron beam lithography), but economics could slow down, or even break, the progression of this technology [61]. The potential offered by a bottom-up, or self-assembly, approach like the above described VLS could thus constitute an important cornerstone in the development of the next generation of devices.

The downscaling in the size of crystals that can be synthesized via this technique further opens the door to structures that are not practically feasible in 2D epitaxial growth, such as highly mismatched heterostructures incorporated in the NWs [31,62]. Moreover, monolithic integration of III-V structures on group IV substrates [63,64] now becomes a viable path not only for performance enhancement of existing devices, but also incorporation of new functionalities. As a result, it is now well recognized within the research community and the semiconductor industry (see for instance the International Technology Roadmap for Semiconductors [65]) that one-dimensional structures will play a major role in the efforts towards device miniaturization and the development of novel applications. Already, semiconductor NWs have successfully demonstrated their potential in electronics [66,67], photonics [68,69], renewable energy [70,71], and biosensors [72,73].

Despite these tremendous achievements, the details surrounding the exact nature of the mechanisms involved during NW growth are still not fully understood, and are the subject of numerous investigations. These efforts are essential in the determination of the optimum deposition conditions that will yield predictable and consistent structures (e.g., core-shell vs. axial heterostructures). The majority of the work reported in the literature of metal-assisted growth of III-V NWs apply to MOVPE. While not as largely studied, molecular beam epitaxy (MBE) techniques have also successfully been employed in the same manner for the fabrication of 1D structures in various material systems [53, 54, 74–76]. The ultra-high vacuum conditions that prevail during MBE growth are beneficial not only in yielding high purity crystals, but they also enable in situ monitoring of the surface as the growth proceeds. For instance, the state of the seed particle can be investigated using reflection high energy electron diffraction (RHEED) [77]. Additionally, the low growth rate achievable with this type of system allows the fabrication of heterostructure NWs with very abrupt interfaces [78].

The purpose of the present work was thus to develop, through the variation of growth conditions, a better understanding of the mechanisms (kinetics, thermodynamics) involved in the self-assembly of III-V NWs seeded by Au particles during MBE growth. The practical goal behind this exercise was twofold. First, it was desired to eliminate, or at least minimize, crystal defects (stacking faults) in the NWs. Second, control on the geometry (i.e., pure axial growth vs. combination of axial and radial growth) was targeted in order to establish the fabrication guidelines for future studies. The majority of the experiments were done with GaAs, a material we found well-suited for this kind of work: not only does it play a major role in the development of electronic and optoelectronic applications due to its inherent properties, but it is also a material that has a fairly wide growth temperature window, thus enabling a large variety of growth condition combinations. Characterization of the NWs was limited to their morphological and structural properties.

Chapter 2

Growth and Characterization Techniques

This chapter provides a generic description of the experimental methods that have been used throughout this thesis, from the formation of Au nanoparticles on the semiconductor surfaces and growth by molecular beam epitaxy (MBE), to the analysis of the resulting specimens by electron microscopy. While numerous authors already have extensively described these latter techniques, the emphasis will be given here to their specific application to semiconductor NWs.

2.1 Synthesis of Au Nanoparticles by Thermal Annealing

A variety of methods have been employed to form Au nanoparticles on the surfaces as precursors for the VLS growth of NWs, including colloidal solutions [84,85], direct deposition through shadow masks formed by nanochannel alumina templates [86], as well as electron-beam (e-beam) lithography [87]. While these result in good size distributions, they also come with their limitations, such as the higher level of contamination often associated with the approach of colloid chemistry [88], the complicated size selection and particle delivery of aerosol deposition [89], and the high cost and low throughput of e-beam writing processes. A simple and less costly alternative consists in exploiting the instability of very thin (< 10 nm) films of Au at elevated temperatures to induce the self-assembly of nanoparticles on the underlying substrate. This method was used in various semiconductor NW studies (for example the work presented in References [56, 77, 90], but can result in a broad size distribution, with particle diameters varying between 20 and 800 nm (for an initial 4 nm-thick Au film on a GaAs (111)B surface, as will be seen in Chapter 3) depending on the conditions.

In this section, a brief description of the technique that was used throughout this thesis to obtain Au nanoparticles on the semiconductor substrates is presented. It is based on the results of a study that we performed in order to better understand the principles behind the formation of the nanoparticles, and the role played by the surface preparation. For a complete description of the experiments and all associated results, the interested reader is invited to consult our article already published in Applied Surface Science [79]. Note that a rapid thermal annealer (RTA) furnace was then used to simplify the process, and the results most likely differ from a heat treatment within the MBE chamber (as for actual growth of NWs), but it is believed that the generic operating principles remain similar.

All specimens discussed in this thesis were grown on epi-ready n-type GaAs (1 1 1)B substrates supplied by AXT Inc. [91]. Prior to growth, the surfaces were first cleaned following a standard process, beginning with a UV/ozone treatment in a UVOCS [92] reactor for 20 minutes in order to remove any contamination from hydrocarbons and grow a thin layer of oxides (on the order of 3 nm in thickness [93]). The latter was then etched in a 10% buffered HF solution for 30 seconds, and rinsed with deionized (DI) water (typically for 10 minutes). Following this surface treatment, the substrates were transported in ambient air to an e-beam evaporation system, where a Au film was deposited at room temperature, at an average rate of 0.1 nm per second as determined by a quartz crystal monitor (thickness will be specified within the context of each specific experiment reported in the thesis).

For the purpose of the annealing study, 1 and 4 nm films were deposited. The samples were then heat-treated in a nitrogen environment using a AG Associates Mini-

Pulse RTA furnace at a temperature of 500°C for 5 minutes (typical ramp rate of 1°C per second). During annealing the GaAs substrates were capped with GaAs (1 0 0) pieces to minimize the loss of As due to possible desorption. Note that subsequent studies by Ghosh and co-workers revealed that proximity caps play no significant role during annealing treatment at 500°C of Au-covered GaAs (1 0 0)-oriented surfaces, and that deterioration was always observed [94]. This could potentially explain discrepancies with specimens annealed in the MBE chamber, where an As_2 overpressure is applied to ensure stoichiometry is conserved, but such an investigation falls outside the scope of the present work.

Figure 2.1 illustrates the effect of annealing 1 and 4 nm-thick films of Au on GaAs (1 1 1)B at 500°C. Atomic force microscopy (AFM) was used to characterize the pre-annealed specimens, since scanning electron microscopy (SEM) did not prove efficient to resolve the fine details on the surfaces. While such small amounts of Au do not yield uniform films, no significant clustering can be noticed prior to any heat treatment (Figure 2.1a and c). Heating the surfaces, on the other hand, promoted the formation of Au islands (Figures 2.1b and d). The size distribution remains however quite broad in both cases, as shown in the graphics of Figure 2.2, as obtained from the processing of SEM images such as the ones in Figures 2.1b and d, using the ImageJ software [95]. Information on average island size and density is summarized in Table 2.1. Clearly, a thinner film results in smaller islands, with a concomitant increase in their density.

The shape of the island size distribution can be indicative of the diffusion processes occurring during heat treatment. Two different mechanisms to describe particle sintering are typically proposed: Ostwald ripening, and particle migration and coalescence. In Ostwald ripening, a migration of atoms or small clusters takes place that forms larger particles or islands from smaller ones without the islands having to be in

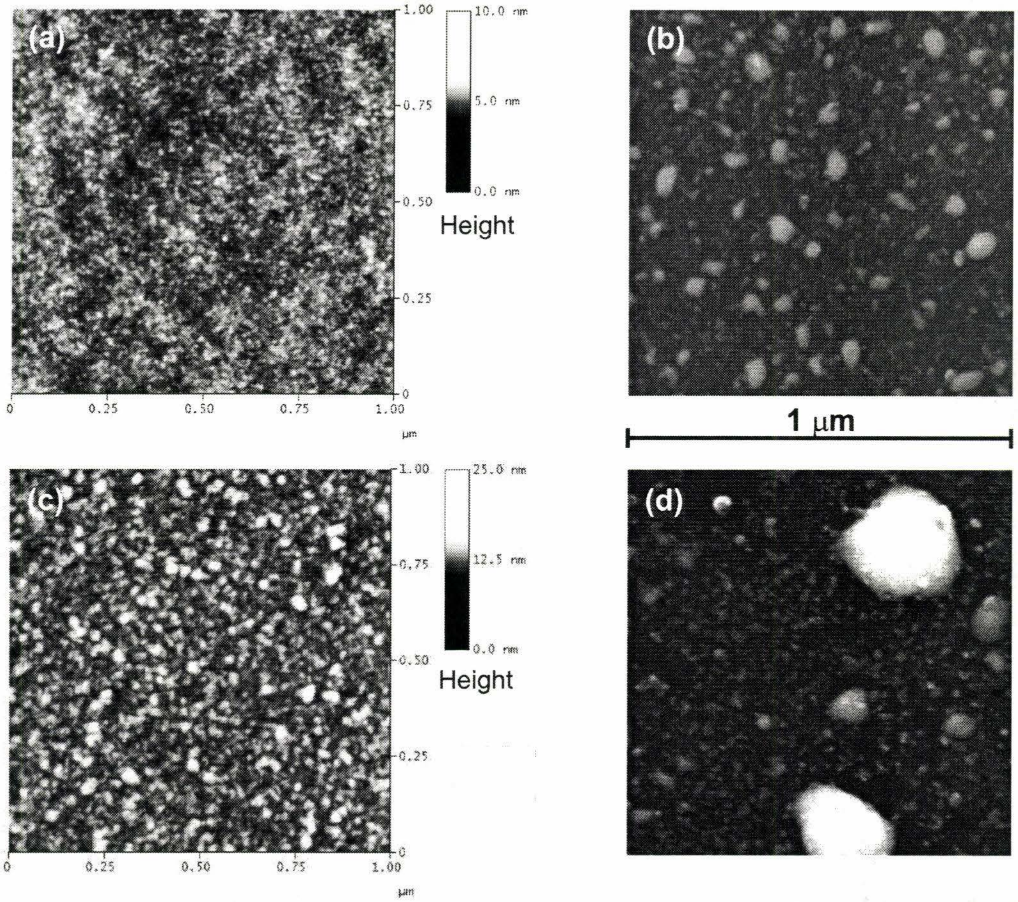

Figure 2.1: Effect of thermal annealing on a thin Au film deposited on a GaAs (1 1 1)B substrate. (a,c) AFM detail of a 1 nm (a) and 4 nm (c) as-deposited film. (b,d) SEM top view of the surfaces after a 5-minute anneal at 500°C; (b) 1 nm and (d) 4 nm film.

Table 2.1: Average Au particle size and density as a function of initial film thickness

Au film thickness nm	Average island size[a] nm	Island density $\times 10^9$ cm^{-2}
4	68 (15 – 587)	1.4
1	29 (10 – 90)	13

[a] The heat treatment resulted in non-Gaussian distributions; the average particle size is therefore provided along with the total size range (in brackets) that was measured

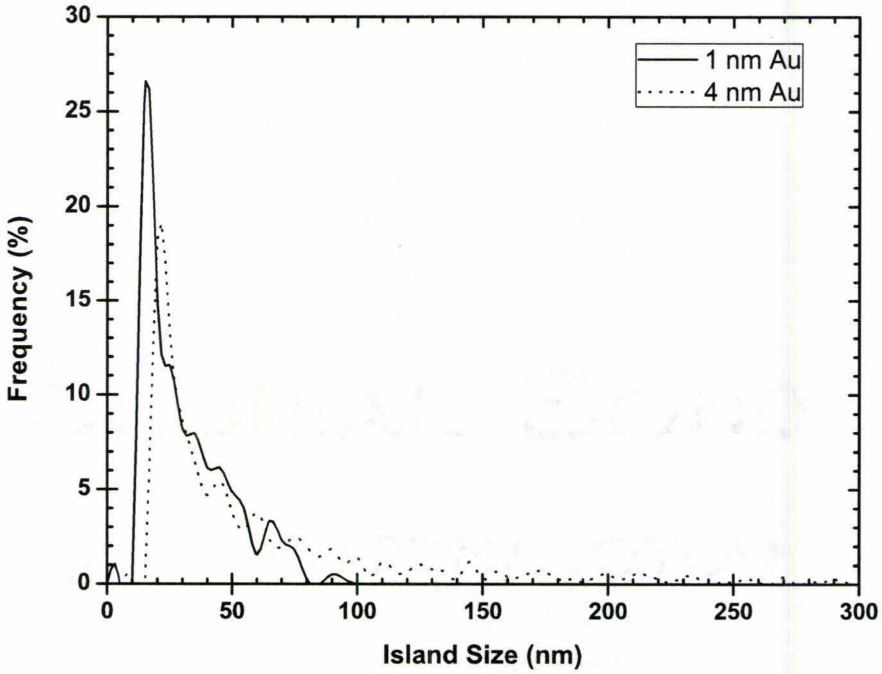

Figure 2.2: Size distributions of Au particles on GaAs (1 1 1)B surfaces after 5 minutes annealing at 500°C for a 1 and a 4 nm Au deposit.

direct contact (i.e., larger clusters grow at the expense of smaller ones due to diffusion of individual adatoms from the latter toward the former). This process results in a size distribution usually skewed toward smaller particles. In particle migration and coalescence, the Au islands or particles are assumed to be mobile, and coalescence results from the collisions between separate islands. A size distribution skewed toward larger particles is usually observed [96,97].

The island size distributions obtained for the two film thicknesses studied (Figure 2.2) have the same characteristic shape: a rapid ascension to a peak followed by a long tail, which would therefore suggest Au migration and coalescence as the operative mechanism for island formation. On the other hand, recent studies by Datye and co-workers [97] pointed out that no such inference could be made purely on the basis of particle size distribution, since either Ostwald ripening or coalescence could yield similar size distributions under certain conditions. Self-assembly of the Au islands could possibly then involve multiple mechanisms operating concurrently. Moreover alloying of Au with the underlying substrate, as suggested by the focused ion beam (FIB) cross-sectioned island in Figure 2.3, could be established, with the particle extending approximately 35 nm below the surface (dashed line in Figure 2.3). From a quantitative point of view, energy dispersive X-ray (EDX) spectrometry performed on a large island (~600 nm in transverse size), indicated a significant content (~20 at.%) of Ga in the particle. Note that such alloying was not considered in previous models; therefore a complete description of the operative mechanisms occurring during the self-assembly process of Au islands is unclear at the moment, and would deserve further study.

In sum, the self-assembly of Au nanoparticles on the substrate results from the thermal activation of diffusion processes, and the size and density distributions can be controlled notably via the thickness of the initial Au film deposited. This constitutes

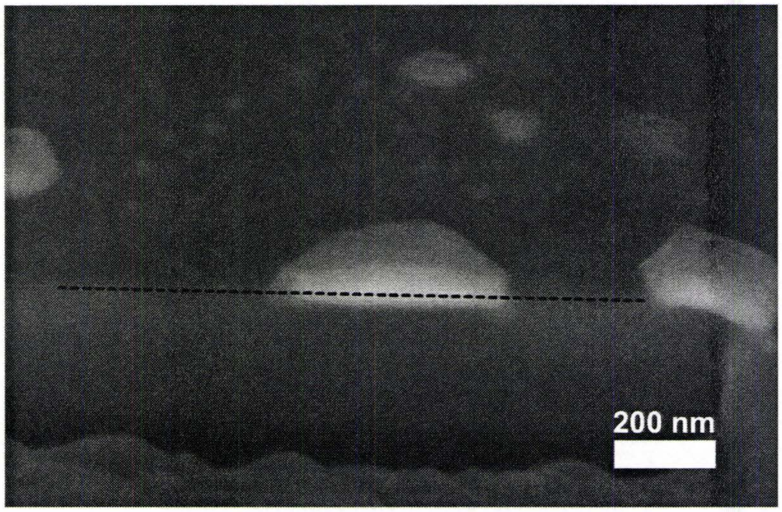

Figure 2.3: SEM picture of a FIB-sectioned particle resulting from the annealing (500°C, 5 minutes) of a 4 nm Au film on a GaAs (1 1 1)B surface.

a simple and affordable means to produce large quantities of nanoparticles, and is well suited for the purpose of the present NW studies.

2.2 Gas Source Molecular Beam Epitaxy

Epitaxy, from the Greek roots *epi* ("resting upon") and *taxis* ("arrangement"), is a crystalline film growth process in which the atoms of the growing film mimic the arrangement of the atoms of the underlying substrate [98]. As its name implies, molecular beam epitaxy (MBE) is a method to achieve high-quality single-crystal epitaxial layers. Crystallization occurs via the reactions and condensation of the constituent species that arrive at the surface of a heated substrate. These species, which are supplied in molecular or atomic form, originate from the evaporation of raw material initially placed in effusion cells, or supplied from gas sources. The ultra-high vacuum (UHV) conditions that prevail within the reactor (base pressure on the order of 10^{-9}

Torr in the system used) ensures that collisions between effusing atoms/molecules, or with residual gases, do not occur prior to reaching the substrate (i.e., the mean free path of the atoms/molecules is longer than the effusion cell – substrate distance), hence the "molecular beam" nature of the technique. A mechanically controlled shutter placed in front of each effusion cell allows rapid switching of the beams on and off, and thus enable monolayer control during the deposition (typically done at a low growth rate on the order of one monolayer per second) for the realization of sharp interfaces and/or abrupt doping transitions.

In conventional MBE growth of III-V compounds, both group III and V species initially placed in the effusion cells consist of the solid elements themselves. Upon resistance heating of the cells, the vapour pressure of the elements they contain increases so evaporation is initiated and film growth starts as the species impinge on the substrate. The type of system used at McMaster University, and which consequently was used for the fabrication of all the specimens studied in this current work, consists in a modification of this previous implementation, where the group III species still consist of the solid elements, but the group V solid source is replaced by a hydride gas that is thermally decomposed (cracked) to obtain the desired product (e.g. AsH_3 as a source of arsenic molecules, and PH_3 as a source of phosphorous molecules). This so-called gas source MBE (GS-MBE), or hydride-source MBE, technique was first proposed by Panish [99], and notably enables the rapid and precise adjustment of the group V fluxes by individual mass-flow controllers, which have a faster and more stable response than solid sources that require temperature control of the effusion cell to achieve the same purpose [100]. The hydride gases are delivered from tanks that are separated from the growth system to the single cracking cell (where mixing also occur), and effuse in the growth chamber through the same tube. Various by-products result from the hydride decomposition, including x, x_2, x_4, xH, and

H (with x being As or P), and the relative amount of each of these will depend on the temperature, pressure, and how close thermodynamic equilibrium is achieved in the cracker cell. Under the operating conditions of the McMaster system, the cell is maintained at a temperature of 950°C, which ensures a predominance of dimers (x_2). For instance, the As_2/As_4 (P_2/P_4) beam flux ratio is expected to be on the order of 10^4 (10^4), As_2/As (P_2/P) about 10^3 (10^5), As_2/AsH (P_2/PH) about 10^5 (10^6), and As_2/H (P_2/H) about 10^3 (10^3) [100]. Hydrogen is therefore always present during growth, but does not incorporate in the crystal under normal growth conditions.

Figure 2.4 shows a simplified representation of the system used for the samples fabricated for the studies presented in this thesis (all but the ones from Section 3.1, as will be specified at that point). It was built by SVT Associates [101] under the custom specifications provided by McMaster growth specialist Dr. Brad Robinson. Note the vertical geometry of the system, where the sample is held horizontally, face down, with the sources being at the bottom of the growth chamber, making an angle of ~35° with the normal of the sample. The temperature of the substrate is primarily measured with a thermocouple fixed to the stage under the substrate, which provides a relative measurement that is reliable enough for setting a desired set of conditions previously established and calibrated. A more accurate measurement of the surface temperature is obtained with an infrared pyrometer.

Each processed substrate (as per the method described in Section 2.1) was first mounted onto a holder in dust-free conditions, under a high efficiency particulate air (HEPA) filter. The holder consists of a molybdenum puck with a hole having a specific geometrical shape machined in the centre, and the substrate is simply inserted on the back, with the surface to be deposited on facing down so it is exposed to the beam once it is in the chamber. The substrate is held in place by gravity with its edges lying on a recessed ledge having the same shape as the hole, and any lateral movement is

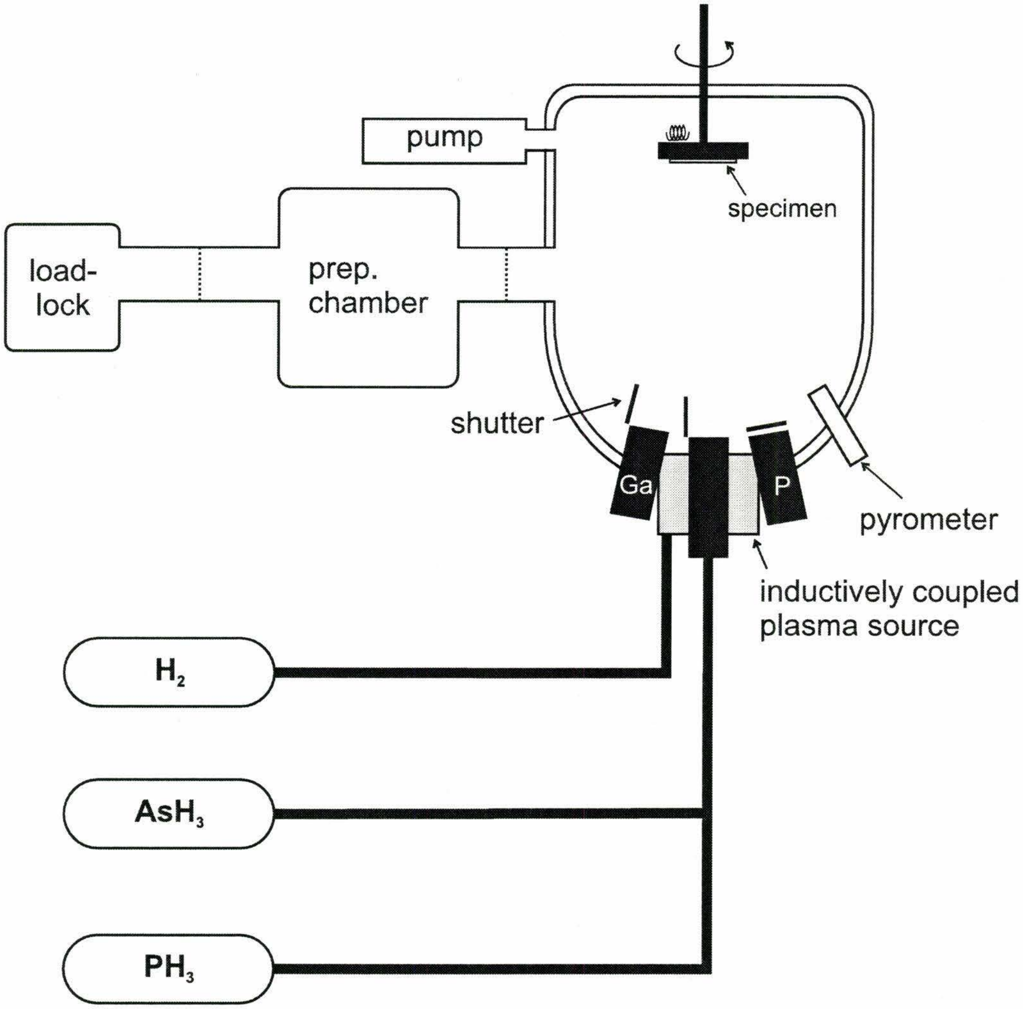

Figure 2.4: Simplified representation of the GS-MBE system used for the fabrication of all samples studied within the framework of this thesis.

prevented with small tantalum shims on the sides. Note that the substrate must have the same dimensions as the hole. A series of holders with specific hole dimensions were initially available: one for a full 3-inch wafer, one for a full 2-inch wafer, one for a 1/4-2-inch wafer, and another one for a 11-mm square. Since the surface orientation of all the samples was (1 1 1)B, it was not possible to cleave it to either a square or a 1/4-wafer. Most of the initial samples (Chapter 3, Section 5.1) were therefore either indium-mounted unto a suitable GaAs (1 0 0) substrate, or grown on a full 2-inch wafer. The small size of pieces enabled by the former technique (coupled to the waste of a sacrificial (1 0 0) substrate), and the high cost associated with the latter (when often only a small fraction of the wafer was necessary for a complete analysis) led us to design a new holder that was used for the remainder of our studies (Chapters 4 and 6, Section 5.2). Consisting of a molybdenum puck with a "pie"-shaped hole in its center, it accommodates 1/6 of a 3-inch (1 1 1)B-oriented wafer that can easily be cleaved to dimensions, and its size provides enough material for all the post-growth characterization that was required. One single wafer therefore provides enough material for six growths, and combined with optimized material utilization, reduces the overall cost per growth.

After being introduced in the system via the load-lock, the substrate was transferred *in vacuo* to the preparation chamber, where it was degassed at a typical temperature of 300°C for 15 minutes (any variation to this procedure will be specified when required in the text). It was then transferred to the main growth chamber, secured to a rotating stage, and resistance-heated to the appropriate temperature for Au nanoparticle formation and oxide desorption. The latter operation was achieved with a hydrogen plasma generated by an inductively coupled plasma (ICP) source, under an As_2 overpressure to ensure surface stoichiometry was preserved. Details on substrate temperature and duration of treatment will be provided within each section. During this final cleaning step, the Ga and/or In effusion cells were heated to the appropriate temperature in order to obtain the desired nominal growth rate, which had been previously established in calibration runs done on GaAs (1 0 0) substrates. Following oxide desorption, the substrate was brought to the proper temperature for the growth (between 400 and 600°C), and the AsH_3 and/or PH_3 flow increased to establish the desired V/III flux ratio. The Ga and/or In shutter was then opened to initiate the growth. During the growth, the sample was rotated (1 full rotation every 4 seconds) to ensure uniform distribution of the beam on the surface. After the prescribed duration (between 3 and 60 minutes), the shutter was applied in front of the group III effusion cell, and the substrate slowly cooled under the As_2 overpressure, which was turned off when the substrate temperature dropped below 350°C.

2.3 Characterization by Electron Microscopy

Two principal levels of structural information were of interest in the characterization of the as-grown samples: surface topography and morphology (distribution of the NWs on the substrate surface, their general geometrical shape, their growth direction, their dimensions), and crystal structures of the NWs (lattice type, defects, interfaces between two materials in the case of heterostructures). While the latter could be obtained via the use of the transmission electron microscope (TEM), the former was typically retrieved from the analysis by scanning electron microscope (SEM). Both methods therefore provided complementary information toward the description of the growth mechanisms. A brief summary of the underlying principles is here presented, and emphasis is after given to the experimental conditions that were used for the analysis of the semiconducting NW samples, as well as some practical considerations for length measurements and accurate characterization of the crystal structure.

2.3.1 Fundamental Concepts

The dual nature of the electron, which behaves both like a particle and a wave, is at the basis of electron microscopy. First theoretically postulated by de Broglie, and shortly thereafter verified experimentally by two independent groups [102], the particle momentum p can be related to its wavelength λ via the Planck's constant h (6.626×10^{-34} J s) by the following relation:

$$\lambda = \frac{h}{p}. \tag{2.1}$$

By accelerating it through a difference of potential V, the electron of mass m_o gains a kinetic energy $m_o v^2/2$ (with v being the velocity) that is equal to the potential energy eV (where e is the charge of the electron), which translates into a momentum

$$p = m_o v = \sqrt{2 m_o e V}. \tag{2.2}$$

Accounting for relativistic effects, which become important for accelerating voltages of 100 kV and above, the wavelength associated with the electron then becomes

$$\lambda = \frac{h}{\sqrt{2 m_o e V \left(1 + \frac{eV}{2 m_o c^2}\right)}}, \tag{2.3}$$

with c being the speed of light. Even for small voltages electrons can already achieve wavelengths on the same order of magnitude as X-ray radiation, and that are comparable to atomic dimensions (e.g., at $V = 50$ V, $\lambda = 0.17$ nm). Increasing the electron velocity shrinks furthermore the wavelength (e.g., $\lambda = 0.010$ nm and 0.003 nm for $V = 15$ kV and 120 kV, respectively), and therefore enables imaging samples with spatial resolution significantly better than a light-optical microscope. Thus, using an appropriate set of magnetic lenses to deflect a beam of electrons unto a specimen, the different interactions of the particles with the latter can be exploited to retrieve various information on the analyzed materials.

2.3.2 SEM Analysis

Except for three instances (Figures 2.3, 5.2, and 5.8, which were taken at the University of Western Ontario with the assistance of Dr. Todd Simpson), all the SEM images reported within this thesis were produced using a JEOL [103] JSM-7000F instrument (equipped with a field emission electron gun) operated in the secondary electron mode. Supported NW samples (i.e., the NWs still attached to the substrate onto which they were grown) were prepared following a simple procedure adapted to the type of imaging desired:

- For top and tilted views, a small piece (parallelogram or triangle, ~5 mm per side) was cleaved from the as-grown substrates, always in the vicinity of the centre in order to ensure a straight comparison between different specimens. The crystal orientation was indicated directly on each piece by lightly scoring it with a scribe to mark the direction of the primary flat (i.e., $[0\ \bar{1}\ 1]$ for the $(1\ 1\ 1)$B-oriented wafers that were used). Samples were then fixed, lying flat, on the edge of a standard aluminium SEM circular stub using silver paint or carbon adhesive tape. Placing the samples on the stub edge, with even a small portion outside of the stub area as shown in Figure 2.5a, allowed to bring the sample close to the electron column when the stage was tilted.
- Because 90° stage-tilting is not possible with this microscope, the same sample as for top and tilted views could not be used for cross-sectional imaging. For this purpose, the sample was also cleaved in the vicinity of the substrate centre, but a parallelogram shape was enforced. It was then mounted on a modified

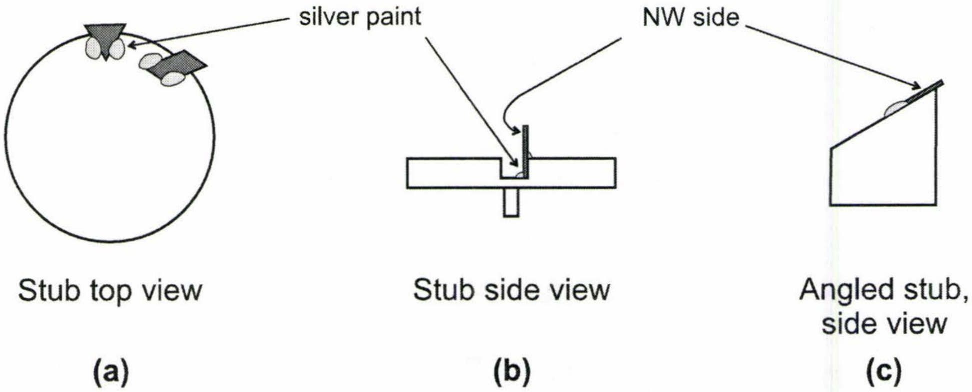

Figure 2.5: Schematic illustrating the mounting of the specimen on the stub for SEM characterization. (a) For top and tilted imaging; (b) for cross-sectional imaging; (c) alternative approach for cross-sectional imaging using an angled stub.

stub containing a notch to secure the piece in a vertical position using silver paint, as illustrated in Figure 2.5b.

- While this latter method for cross-sectional imaging worked well in the majority of cases, specimens with shorter NWs (e.g. short growth duration), and/or lower surface density, were often affected by significant background noise caused by the secondary electrons emitted from the stub and/or the silver paint. An alternative approach, depicted in Figure 2.5c, allowed us to improve the quality of the images. The sample was mounted flat, using silver paint, on an angled stub (e.g., 30° or 45°) with a straight edge tangential to the latter. Once in the microscope the stage was tilted by an amount sufficient to bring the sample vertical (e.g. by 60° for a 30° stub, or 45° for a 45° stub). Many thanks go to my colleague Subir Ghosh for this latter recommendation.

For top view imaging, the stage was always first rotated so that the top of the viewing screen was parallel to the primary flat. This ensured uniformity in the orientation of all the images produced, and prevented any confusion, notably with regards to the identification of the NW sidewall facets. An intermediate accelerating voltage of 15 kV, coupled to a short working distance (on the order of 4 mm), yielded the optimum results for this type of imaging. Notably, a clear illustration of facet transition (as the image in Figure 3.6 taken at a magnification of 250,000X) could be established under these conditions, while lower voltage and/or probe current often resulted in noisy images.

The scenario was different for tilted and cross-sectional imaging. Due to the small lateral dimension of the NWs (typically under 100 nm in diameter), very energetic electrons can easily go through the structures. The accelerating voltage was then reduced in order to get a balance between resolution and noise. A good compromise was found at a value of around 4 kV (working distance ~4 mm) for cross-sectional views, and 3 kV (working distance ~4 mm) for tilted views. Note that a careful alignment of the beam and stigmators was always necessary to optimize the image quality in all the above scenarios.

SEM images were often used for quantitative purposes, with the dimension of the features (NWs, seed particles) directly measured on the micrographs using the scale marker digitally generated by the software controlling the instrument. Note that for tilted views a correction needed to be applied to obtain an accurate measurement of the NW height due to the foreshortening effect [104], which does not occur when the electron beam is perpendicular to the feature being scanned (as in the cases of top and cross-sectional imaging). As illustrated in Figure 2.6 for a specimen tilted by an angle θ with respect to the beam, the scan excursion ℓ on a NW that grew perpendicular to the substrate surface (i.e., growth done on a (1 1 1)B substrate) is shorter than the actual NW H_w. The length measured on the micrographs must therefore be corrected by a geometrical factor to obtain the correct value:

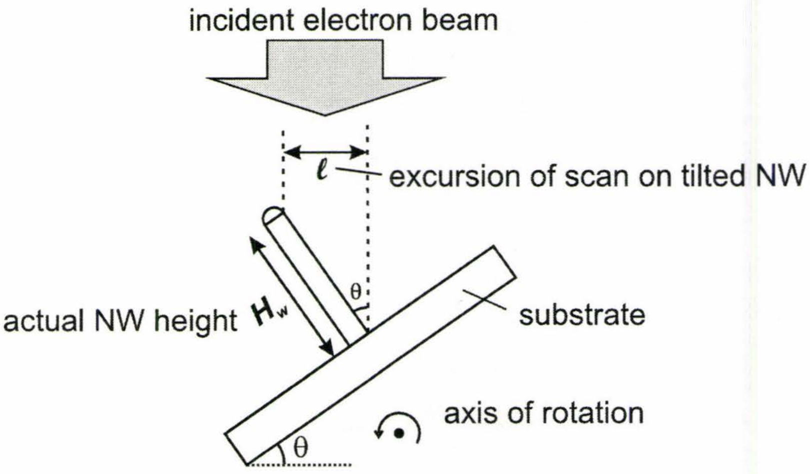

Figure 2.6: Schematic illustrating the correction to be applied for measurement of tilted specimens from SEM micrographs.

$$\text{Actual NW Height } H_w = \frac{\text{NW length measured on micrograph } \ell}{\sin\theta}. \tag{2.4}$$

2.3.3 TEM Analysis

In contrast with the SEM technique which allows for the inspection of surface features of a specimen via the collection of secondary electrons, thus enabling the collection of generic information on morphology such as the growth orientation of the NWs and their dimension, the more energetic electrons (>100 keV) generated in the TEM column can be transmitted through the specimen of interest, provided it is thin enough (i.e., <200 nm). Moreover, if the solid is crystalline, the electrons will be diffracted by the various atomic planes of the structure (similar to Bragg diffraction observed with X-rays). Collecting and focusing these transmitted electrons will thus allow the formation of an image containing structural details about the specimen, so defects, when present, will notably be visible.

Because the structures of interest (the NWs) were typically thinner than 100 nm, any mechanical polishing and ion milling required in a standard sample preparation procedure were not necessary in our case. Instead, the NWs were broken off the surface of the underlying substrate by putting a specimen in a small vial, adding acetone, and sonicating for 1–2 minutes. A small volume ($\sim$20 μl in total, by drops of 5 μl) of the solution was then typically transferred onto a standard TEM copper carbon holey grid using a mechanical micro-pipettor (Cole-Parmer [105], model # EW-21600-62). The size of the piece and quantity of acetone varied depending on the NW density on the substrate surface, but was chosen to result in good density and dispersion of NWs on the grid after solvent evaporation. The grid was then mounted on a double-tilt stage for characterization.

A Philips CM12 conventional TEM (CTEM), operated at 120 kV, was primarily used to quantify the number of defects (stacking faults) in the NWs. Note that prior to proceeding to the imaging itself, the specimen was carefully tilted so the electron beam was parallel to a $\langle\bar{2}\ 1\ 1\ 0\rangle$ direction of the NW crystal being investigated (the zone axis alignment). This adjustment was critical for the accurate characterization of the NW, since a misalignment would result in a distorted representation of the stacking faults (as, for example, is illustrated in Figure 2.7a). Due to the nature of the crystal and its defects, a stacking fault could even completely "disappear" [106] if the specimen was aligned on a $\langle\bar{1}\ 1\ 0\ 0\rangle$ zone axis (as is shown in Figure 2.7b, with the corresponding selected area electron diffraction patterns in Figure 2.7c). This is due to the fact that under that particular condition the atom stacking of the wurtzite crystal (the structure of the NW) is identical to the one of the zincblende crystal (the stacking fault structure), so no contrast can be distinguished.

Each NW was typically imaged, in bright field condition, in multiple segments at a magnification of 100,000X, and picture stitching was subsequently performed

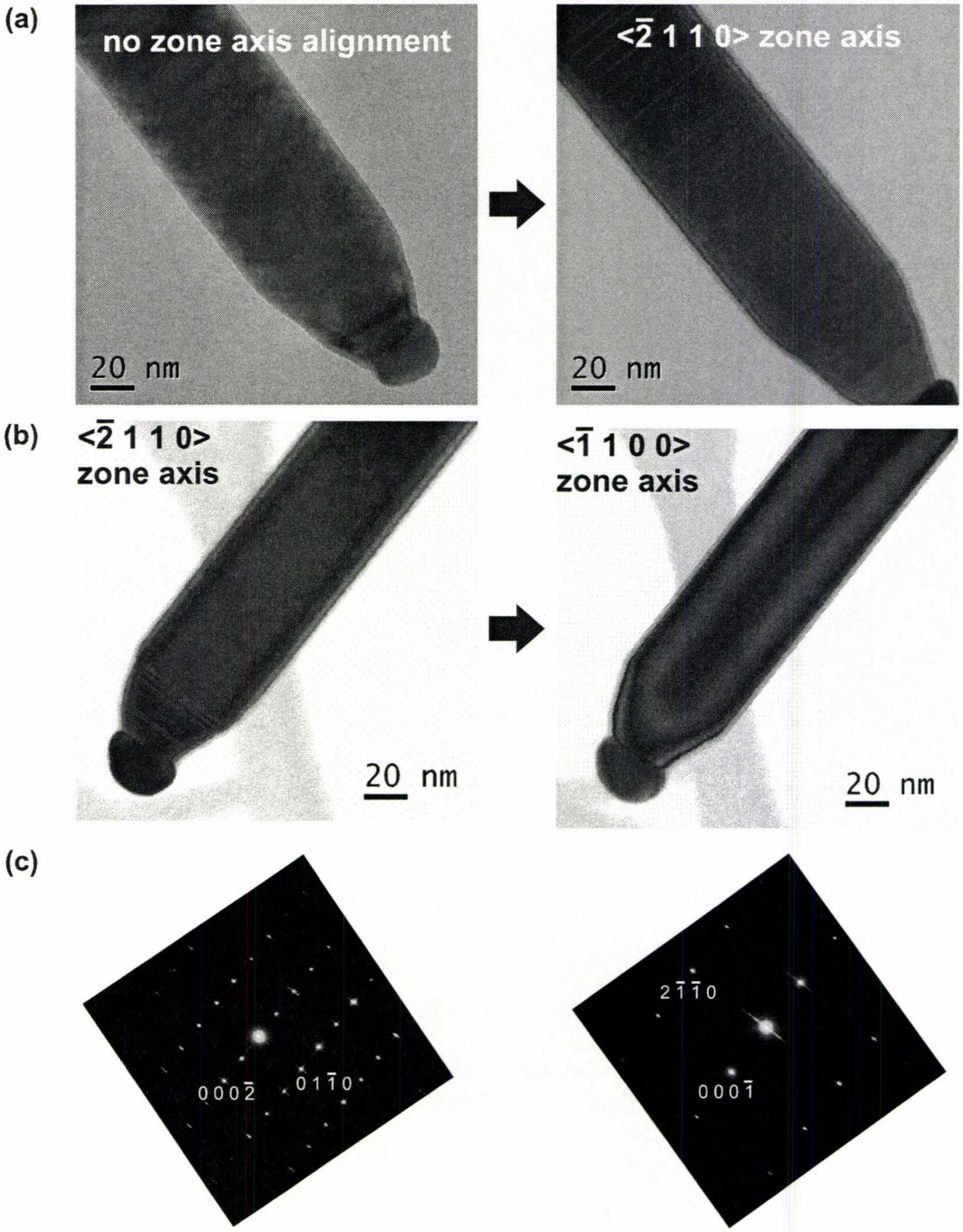

Figure 2.7: Effects of not aligning the NW on the proper zone axis for TEM characterization. (a) NW not on zone axis compared to proper alignment; (b) stacking faults "disappearing" as a result of aligning to an improper zone axis; (c) selected area electron diffraction patterns for the two zone axes in (b).

to obtain a global image of the structure. In all cases an objective aperture was inserted in the back focal plane, blocking all scattered electrons but the transmitted beam, thus enhancing the contrast of the image. To obtain the stacking fault linear density (i.e., number of stacking fault per unit length in the NW), faults were counted manually on the TEM micrographs directly.

The nature of the crystal defect was further investigated using a JEOL JEM-2010F high resolution TEM (HR-TEM), equipped with a field emission electron gun, and operated at an accelerating voltage of 200 kV. Lattice-resolved images were digitally recorded, and analyzed using the DigitalMicrograph software [107]. All the images obtained with this instrument, and presented in this thesis, were produced by instrument specialists Mr. Fred Pearson and Dr. Nadi Braidy (for Section 5.2).

2.3.4 Energy-Dispersive X-Ray Spectroscopy

To complement the structural (external *and* internal) information acquired by the two imaging techniques described above, it was at times necessary to determine the chemical composition of the specimen studied, notably for the analysis of the seed particle (as, for example, in Section 2.1) and heterostructure NWs (Chapter 5). Fortunately, some of the phenomena taking place when electrons interact with matter enable to identify the elements present in the specimen, so this analysis can often be combined with imaging.

Upon entering the specimen, a primary energetic electron has a probability to be inelastically scattered by an inner-shell electron (e.g. K- and L-shell) of the host materials, thus ejecting the latter to a higher-energy orbit, and creating a vacancy in the inner shell. The atom remains in this excited state for a very brief amount of time ($\sim 10^{-15}$ s), during which another atomic electron from a higher level makes a downward transition to fill this vacancy. One of the possible processes that can take place during this relaxation is the emission of a photon (X-ray) with an energy equal to the difference in binding energy between the upper and lower levels [108]. Since each element in the periodic table exhibits a unique set of X-ray spectral lines, the previous emission process serves to clearly identify the materials being probed. A spectrum of the emitted X-rays can thus be generated using a dispersive device to distinguish the photons based on their energy. This is the process at the origin of energy-dispersive X-ray (EDX) spectroscopy.

Within the framework of this thesis, the technique was used primarily with the JEOL 2010F, in scanning TEM mode, for linescans or elemental mapping to determine the location of interfaces in heterostructure NWs. Point measurements were also used for the compositional analysis of the seed particles. All results were quantified with the INCA software [109].

Chapter 3

Growth of GaAs Nanowires

3.1 Overview of Growth Mechanisms

In this section we present a systematic study of the morphology and kinetics of GaAs NWs grown on GaAs (111)B substrates in a GS-MBE system. Our observations show that the diffusion of adatoms from the 2D surface (substrate) to the tip of the wires is the main mechanism driving the axial growth of these structures for seed particles having a diameter smaller than a certain critical value (in the 105-180 nm range, depending on the growth conditions). For seed particles diameters larger than this critical value, a second growth regime takes over, dominated by the direct impingement of materials on the particle. The observation of this latter regime was for the first time reported by us in the Journal of Crystal Growth [54]. In addition, the change in sidewall facets with the variation of the growth conditions is discussed. Note that the results reported in this section represent our very first attempts at NW growth, and were obtained with a different GS-MBE system, now decommissioned, than the one used for the remainder of this thesis. Therefore, the temperature values quoted are to be taken within the context of this section only, as subsequent growths performed with the SVT system now in use within the department (and for the remainder of this thesis) suggest a discrepancy in temperatures on the order of 50°C when comparing NW morphologies (e.g. a temperature of 550°C in the old system corresponds to 600°C in the SVT system).

3.1.1 Experimental Details

Substrates of GaAs (1 1 1)B were first submitted to a 20-minute UV-ozone treatment in order to remove any contamination from hydrocarbons, and grow a sacrificial layer of oxide. After etching in a 10% buffered HF solution for 30 seconds and rinsing with deionized water, the samples were transported in ambient air to an e-beam evaporation system, where a 4.5 nm-thick film of Au was deposited, as measured by a quartz crystal thickness monitor. The samples with Au deposit were then transferred in ambient air to the GS-MBE growth chamber. Before the actual growth, the Au-covered substrates were heated to a temperature of 600°C for 5 minutes under an As_2 flux to form Au-Ga alloyed nanoparticles on the surface. Simultaneous desorption of native oxide was enhanced by the use of a hydrogen electron cyclotron resonance plasma source. After oxide removal and Au nanoparticle formation, the temperature of the substrate was set to the desired value, and the Ga shutter opened to initiate the NW growth. The dependence of the growth temperature on the morphology of the NWs was investigated by three growths carried out at 500°C (Growth #4388), 550°C (Growth #4387), and 600°C (Growth #4386), with a constant V/III flux ratio of 1.5 (referred to as growths A, B, and C, respectively). All growths were performed at a nominal 2D rate of 1 monolayer/second (ML/s), i.e., 0.28 nm/s, for a duration of 30 minutes.

After the growths, all samples were characterized by SEM in the secondary electron mode. The diameter of the seed particles, and the height of the NWs were obtained by measuring ~150 particles and NWs for each growth directly on the SEM images. The reported heights represent the visible part of the wires, above a 2D layer that grew simultaneously on the non-activated surface (i.e., those areas not covered by Au particles). The reported measurements for the wire height include any correction necessary to account for sample tilt during the SEM imaging.

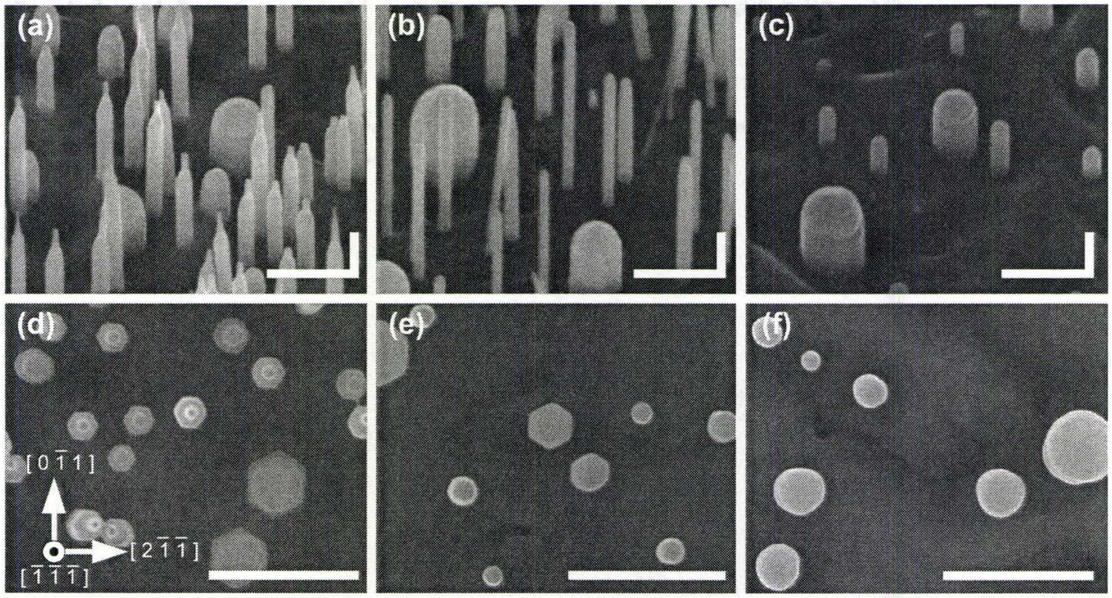

Figure 3.1: 30° tilted (a – c) and top view (d – f) SEM images of Au-seeded GaAs NWs grown at constant V/III flux ratio of 1.5 and temperature of: (a,d) 500°C, (b,e) 550°C, and (c,f) 600°C. The length bars indicate 500 nm; the axes indicating the crystalline orientation in (d) are the same for (e, f), and correspond to the substrate orientation as provided by the wafer supplier.

3.1.2 Results

Tilted and top views of the post-growth surfaces are shown in Figure 3.1. All the wires grew normal to the surface, along the $[\bar{1}\ \bar{1}\ \bar{1}]$ direction, which is the energetically favorable orientation for semiconductor NWs grown by the VLS mechanism [22]. The presence of Au at the top of the NWs was confirmed by EDX, verifying that the wires grew by the metal-assisted process described in Chapter 1.

SEM characterization further revealed that the wires are tapered when grown at low temperature (500°C). This is most evident for wires with particle diameter below ~125 nm. Note that only the top part of the wire, close to the Au particle, was tapered. The lower part, while wider than the top, appeared to be very uniform. When the temperature was raised to 550°C or above, the tapering vanished, resulting

Table 3.1: Critical diameters and diffusion lengths for the various growth conditions.

Sample	Growth Temperature °C	D_{oi}[a] nm	D_{oj}[b] nm	λ_s[c] $\times 10^3$ nm	λ_{sw}[c] $\times 10^3$ nm
A	500	125	50	4.5	7.0
B	550	180	70	7.5	10.0
C	600	105	Mixed, or no facets	4.5	7.0

[a] critical diameter for the transition in growth behavior shown in Figure 3.2.
[b] critical diameter for the transition in faceting as explained in the text.
[c] λ_s and λ_{sw} are the diffusion lengths on the substrate and sidewalls, respectively, used to fit the experimental data (solid curves in Figure 3.2).

in wires that had a filamentary shape with nearly uniform diameter along their entire length. Roughness of the surface surrounding each wire was observed, indicating that 2D growth occurred simultaneously with the Au-assisted process.

The height H_w of the NWs was measured, and plotted as a function of the seed particle diameter D in Figure 3.2. Two distinct growth regimes can be identified from the curves, depending on the size of the particle. For particles with diameter D smaller than a certain critical value D_{oi}, the average growth rate of the wires decreases with increasing D. These D_{oi}'s values are summarized in Table 3.1. A fitting on a log-log plot of the data (not shown) in the $D < D_{oi}$ region of the curve clearly indicates a 1/D dependence of the wire height H_w. The solid curves in Figure 3.2 are fits to the experimental data, and will be discussed in the next section. For $D > D_{oi}$ the situation is reversed, and wires originating from the larger particles grow slightly faster. This trend is emphasized by the dashed lines (guides to the eye) in Figure 3.2.

From the plan view images in Figure 3.1d – f, it is clear, especially in the case of 500°C, that the growth gives rise to different wire sidewall facets. The facets were predominantly $\{\bar{1}\ 1\ 0\}$ for seed particle diameters below a certain critical diameter, D_{oj}, and predominantly $\{\bar{2}\ 1\ 0\}$ above this critical diameter. Table 3.1 gives this

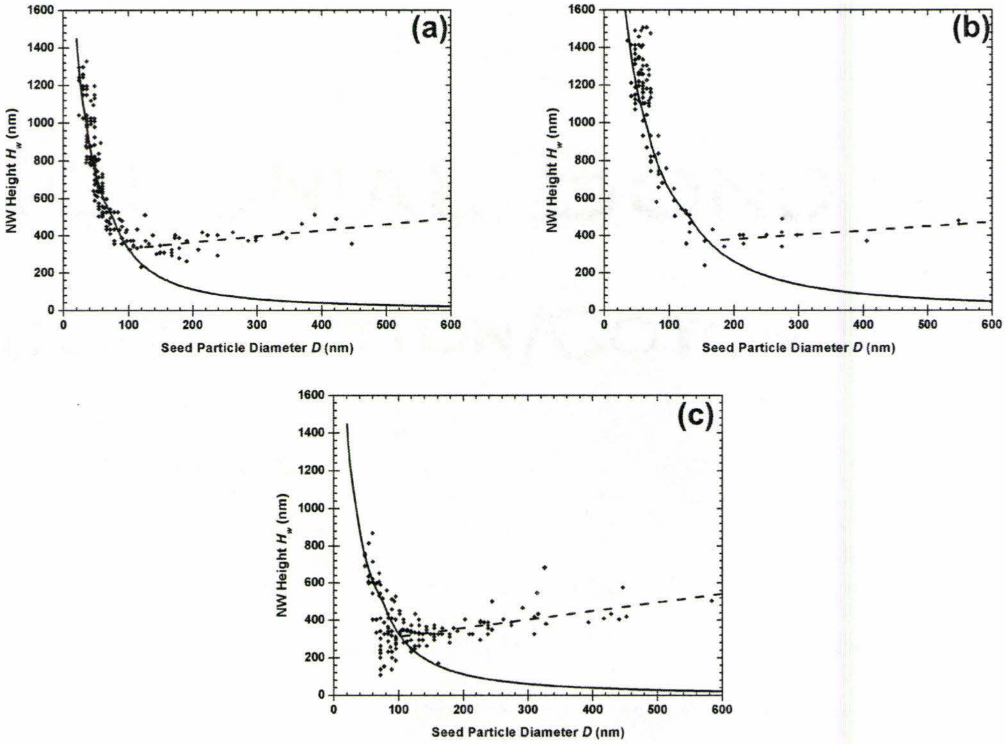

Figure 3.2: Height of GaAs NWs as a function of the seed particle diameter for a V/III flux ratio of 1.5 and substrate temperature of (a) 500°C, (b) 550°C, and (c) 600°C. The solid curves are fits to the data as explained in the text. The dashed lines are guides to the eye.

critical diameter, D_{oj}, at which the change in faceting occurred for each of the growth conditions. As the growth temperature increased, the faceted wires were increasingly intermixed with wires having sidewalls of both types ($\{\bar{1}\ 1\ 0\}$ and $\{\bar{2}\ 1\ 0\}$ planes), or wires in which no facets at all could be discerned (cylinder-like wires).

3.1.3 Discussion

The growth of the wires may be sustained by adatoms supplied via three pathways, as previously presented by Bhunia and co-workers in the case of MOVPE growth of InP NWs [110], and shown in Figure 3.3. Pathways (a) and (b) result from the direct impingement of the growth species on the seed particle. In (a), the species diffuse on the surface of the Au particle in a "random walk" manner until they either desorb or encounter the growth interface. At this point, the adatoms may incorporate into the wire crystal via diffusion along the particle-wire interface. Pathway (b) consists of the bulk diffusion through the Au particle. Finally, the third source of materials (pathway (c)) consists of the growth species impinging on the substrate surface, which may diffuse in a "random walk" manner to the base of the wires, then along the wire sidewalls up to the growth interface. Once again, the adatoms will either incorporate in the crystal by diffusing along the particle-wire interface, or continue their walk on the surface to eventually desorb or diffuse in the Au particle. In this latter scenario, it is assumed for simplicity that the beam of impinging atoms is perpendicular to the substrate surface, which is sufficient for the purpose of the present discussion. A more generic and realistic description, accounting for a beam impinging with a certain angle (due to the geometry of an actual MBE system), will be considered in Chapter 6 within the framework of an analytical model to describe the growth.

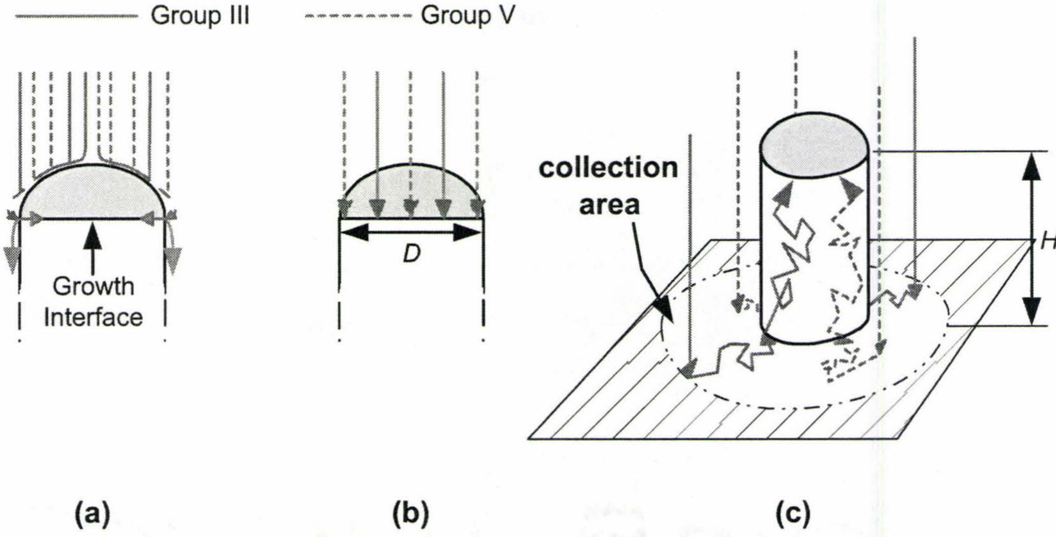

Figure 3.3: Mass transport mechanisms of growth species to the Au-wire interface: (a) direct impingement on the Au particle, followed by diffusion on its surface; (b) direct impingement on the Au particle followed by bulk diffusion through the Au; (c) diffusion on the 2D surface then along the wire sidewalls, in a "random walk" manner.

The dependence of the wire height with the diameter of the seed particle is now discussed according to the three mass transport mechanisms presented above. For Au particles with diameters D smaller than a certain critical value D_{oi} (see Table 3.1 for numerical values), the wire height H_w varies as $1/D$. This regime appears to have been first observed experimentally by Schubert and co-workers for the MBE growth of Si NWs [53], and was subsequently modeled by Dubrovskii and co-workers [56]. The third mass transport mechanism (Figure 3.3c; diffusion from the substrate surface) is predominant in this range of particle diameter. The idea of adatoms diffusing on the sidewalls of the wire up to the tip, and yielding a $1/D$ behavior of wire height, has been well established for over five decades now, and was first described by Sears [8]. Ruth and Hirth later elaborated a model that includes adatom exchange with the substrate, and obtained an analytical expression relating the growth duration t, the NW height H_w, and its diameter D (Equation 35 from Reference [12]):

$$
\begin{aligned}
t = {} & \frac{4\lambda_{sw}^2 D}{\sqrt{2} I (16\lambda_{sw}^2 - D^2)} \ln\left[\cosh\left(\frac{\sqrt{2}}{\lambda_{sw}} H_w\right) + \left(\frac{4\lambda_{sw} + \beta D}{4\beta\lambda_{sw} + D}\right) \sinh\left(\frac{\sqrt{2}}{\lambda_{sw}} H_w\right)\right] \\
& - \frac{D^2 H_w}{I(16\lambda sw^2 - D^2)},
\end{aligned}
\tag{3.1}
$$

where I is the net impingement current on the the NW tip (in nm/s), λ_{sw} is the adatom diffusion length on the sidewalls (in nm), and β is the parameter that accounts for the above mentioned adatom exchange (λ_s being the adatom diffusion length on the substrate surface):

$$
\beta = \left(\frac{\lambda_s}{\lambda_{sw}}\right) \left[\frac{K_1(\sqrt{2}D/2\lambda_s)}{K_0(\sqrt{2}D/2\lambda_s)}\right]. \tag{3.2}
$$

Our data is well described by this latter model, as represented by the solid curves in Figure 3.2. These fits used the diffusion length values from Table 3.1, which are consistent with typical adatom diffusion lengths measured elsewhere [111, 112]. In addition, to successfully fit the model to the data, it was necessary to assume that growth by bulk diffusion was negligible (as represented by the variable I in Equation 3.1: $I < 2 \times 10^{-7}$ μm/s for the fits in Figure 3.2). This latter condition reinforces the assertion that growth of the wire by bulk diffusion (pathway (b)) is negligible in the regime $D < D_{oi}$. Indeed, Wang and Fischman [113] showed that mass transport by bulk diffusion is negligible for sufficiently small particle diameters.

The $D < D_{oi}$ regime clearly bears the signature of diffusion from the 2D surface then up to the wire tip with incorporation occurring at the Au-wire interface. The absence of tapering, coupled with an optimum growth rate, at a temperature of 550°C and V/III flux ratio of 1.5 indicates that adatoms impinging on the 2D surface under these conditions may optimally diffuse up the wire to reach the growth interface. The tapering (or radial growth) observed when lowering the growth temperature (500°C) in the $D < D_{oi}$ range can be attributed to a lower diffusivity of the adatoms on the substrate and sidewalls consistent with the diffusion lengths reported in Table 3.1. Raising the substrate temperature to 600°C increases the probability of desorption (lower mean surface residency time before desorption), again resulting in shorter diffusion lengths and lower wire heights. Normally, as in the case of 2D film deposition, the NW growth is assumed to be limited by the arrival rate of group III adatoms with any excess group V species desorbing. But as will be further explored in Chapter 4, both axial and radial growth can be controlled via the adjustment of the nominal V/III flux, thus suggesting a group V stabilized mechanism.

Unlike the case of CBE where the diffusion of the group V species is considered negligible [114], it appears necessary for the GS-MBE growths to take into account the diffusion of both group III and V species. Examination of the data presented in Figure 3.2 provides strong indication in favor of this argument. For instance, for the three growths presented here that were conducted with a V/III flux ratio of 1.5 and a nominal 2D growth rate of 0.28 nm/s (i.e., ~1 μm/h) for a duration of 1800 seconds (0.5 hour), this would mean that, neglecting desorption, direct impingement would provide enough As for NWs up to 750 nm high at most. However, wires that exceeded, and were even almost twice as tall as this limit were measured, leading us to conclude that growth of the wires must arise from diffusion of both Ga and As_2. A complete model of the NW growth should therefore include a consideration of both group III and V diffusion.

As the diameter of the Au precursor exceeds D_{oi}, the contribution from the 2D surface diffusion decays (solid curves in Figure 3.2), and a transition in the growth process appears to take place. This particular transition had not been observed in any MBE studies [53,56] published thus far, and was for the first time reported by us in the Journal of Crystal Growth [54]. Due to the $1/D$ dependence of the wire height in pathway (c), it is reasonable to assume that direct impingement on the particle becomes the main source of materials to sustain the growth in the $D > D_{oi}$ regime. In this case, the growth of the wires by pathway (a) may be expressed as [53]:

$$\left(\frac{\pi D^2}{4}\right)\frac{dH_w}{dt} = \gamma\left(2\pi D\right), \tag{3.3}$$

where γ is a constant independent of the diameter or growth time. Alternatively, growth may occur by pathway (b) and be expressed as:

$$\left(\frac{\pi D^2}{4}\right)\frac{dH_w}{dt} = \gamma'\left(\frac{\pi D^2}{4}\right), \tag{3.4}$$

where γ' is similarly independent of diameter or growth time.

Accordingly, one would expect a wire height, or growth rate dH_w/dt, that varies inversely with D (Equation 3.3) or is independent of D (Equation 3.4). While not totally accurate, our measurements most closely resemble a growth law that obeys Equation 3.4. Indeed, growth by bulk diffusion is expected to dominate with increasing particle diameters [113]. However, as D increases, the wires appear to grow slightly taller in our case (dashed lines). This could be attributed to multiple factors. For one, an increase of H_w with D is typical of wires grown by chemical vapor deposition (CVD), and as such was first reported and modeled by Givargizov and Chernov [17]. The authors then based their derivation on the Gibbs-Thomson effect, caused by the finite curvature of the wire. A generalization of this model, which also includes considerations on nucleation-mediated growth, was more recently proposed by Dubrovskii and Sivirev [52]. It is then conceivable that the increase of H_w observed in the $D > D_{oi}$ regime be associated with the transition from a mononuclear growth mechanism to a polynuclear one under the Au particle as D increases, coupled to the Gibbs-Thomson effect. Note that since our first report on this second regime, Dubrovskii and co-workers elaborated a model predicting this behaviour [59], and even succesfully fitted our 500 and 550°C data [60].

The observed differences in sidewall faceting were initially thought to have their origin in the crystalline structure of the wires. For instance, Persson and co-workers in their CBE growth study [114] identified the $\{\bar{1}\ 1\ 0\}$ facets with the zincblende crystal structure. It was then believed, prior to any TEM analysis, that the observed $\{\bar{2}\ 1\ 0\}$ facets were actually the $\{\bar{1}\ 1\ 0\ 0\}$ surfaces of the wurtzite structure. The absence of facets, which prevailed in growth C could be the result of alternating layers of the two crystal structures (i.e., zincblende and wurtzite intermixed due to a rotating twin at a $(\bar{1}\ \bar{1}\ \bar{1})$ plane of the zincblende structure, as proposed by Hiruma and co-workers [115]). Subsequent time-dependence studies (as the ones discussed in Sections 3.2 and 6.3.2) however revealed that facets form when the NW exceeds a certain height, and that initially it has a circular cross-section (as was also discussed in Reference [90]).

Our analysis also indicated a possible dependence of the facet type with the diameter of the NW. Table 3.1 presents the diameter at which the sidewall facets changed from $\{\bar{1}\ 1\ 0\}$-type ($< D_{oj}$) to $\{\bar{2}\ 1\ 0\}$-type ($> D_{oj}$). Comparison of D_{oj} with D_{oi} in Table 3.1 indicates that the facet transformations appear unrelated to the change in growth pathway. D_{oj} is always less than D_{oi}, meaning that the facet transition takes place under conditions where growth by surface diffusion (pathway (c)) dominates. As will be clarified in Section 3.2, and further emphasized in Chapter 4, the initial assumption of sidewall facet types being associated with the crystal structure proved to be wrong. Instead, the sidewall facet types are associated with radial growth on the NW sidewalls. The absence of facets in growth C (Table 3.1) is related to an absence of radial growth due to the low height compared to the other two growths. To further elaborate the radial growth of NWs, the NW height and radius were studied for various growth durations, as elaborated in the next section.

3.2 Tapering, Sidewall Faceting and Crystal Structure

In this section we present the morphology evolution of GaAs NWs grown from Au seed particles by GS-MBE. The crystalline structure, the onset of radial growth, and tapering are discussed. In addition, we elaborate a qualitative growth model to describe our results. The essential of the text was published in the Journal of Crystal Growth [80].

3.2.1 Experimental Details

Si-doped (carrier concentration 1.6–2.3 × 10^{18} cm^{-3}) (1 1 1)B-oriented GaAs substrates (AXT Inc. [91]) were first submitted to a UV-ozone cleaning treatment in order to remove any hydrocarbon contamination. The resulting protective oxide layer was etched by dipping the substrates in a commercial 10% buffered HF solution for 30 seconds, and subsequently rinsing under flowing deionized water for 10 minutes. Following the surface preparation, the substrates were then immediately transported in ambient air to an e-beam evaporator system to deposit a 4 nm-thick film (as measured by a quartz crystal monitor) of Au at room temperature. For the synthesis of Au nanoparticles and growth of NWs, the substrates were transferred to the GS-MBE system (SVT Associates Inc. [101]). The substrates were initially degassed for 15 minutes at a temperature of 300°C. In the growth chamber, oxides were desorbed by heating the substrates to a temperature of 525°C while submitting them to a hydrogen plasma from an inductively coupled plasma source for 10 minutes under an As_2 flux. Growth of NWs was initiated by opening the Ga shutter (atom flux yielding a 2D growth rate of 0.28 nm/s), with the As_2 flux set to a nominal V/III flux ratio of ~1.5, and the substrate temperature kept at a constant value of 525°C. These conditions were maintained for durations of 3 (Growth #311), 10 (Growth #312), 30 (Growth #264), and 40 (Growth #313) minutes in four separate growths, after which the substrates were cooled under the As_2 flux, and brought back to ambient conditions.

Characterization of the resulting NWs was performed using a JEOL JSM-7000F field emission scanning electron microscope (FE-SEM) operated at 5 kV (for tilted views) and 15 kV (for top views) in the secondary electron mode to obtain information on surface density (number of NWs per unit area) and morphology (growth orientation on the substrate, height, faceting orientation). Crystal structure was investigated using a Philips CM12 conventional transmission electron microscope (CTEM) operated at 120 kV for bright field imaging and selected area electron diffraction (SAED), while a JEOL JEM-2010F high resolution TEM (HR-TEM) operated at 200 kV was used for lattice resolved imaging. For the TEM analysis, the NWs were broken off the surface of the substrates by putting a specimen in a vial, adding acetone, and sonicating for 1-2 minutes. A small volume ($\sim$20 μl) of the solution was then pipetted onto a standard TEM copper carbon holey grid, resulting in NWs being dispersed after solvent evaporation.

3.2.2 Results

The specimens were first characterized by SEM and CTEM to determine the morphology of the NWs. Typical tilted views of the surfaces after a 3-, 10-, and 30-minute growth are shown in Figures 3.4a – c, along with TEM images of representative NWs from each specimen as insets. In the case of the 40-minute growth (not shown), the NWs exhibited similar morphologies as the ones obtained after 30 minutes. Consistent with the results presented in Section 3.1, the NWs grew predominantly perpendicular to the substrate surface, along the [1 1 1]B direction. For the longer growths (30 and 40 minutes) a minority of NWs grew at tilted angles, but no preferential orientation could be established. It is also evident that the conditions selected for the longer growth durations favored a strong tapering, which was isolated near the NW tip. This is illustrated in the inset of Figure 3.4c, and is most noticeable for the NWs that were seeded from Au particles smaller than 50 nm in diameter.

The dependence of tapering on Au particle diameter is further emphasized by the inset of Figure 3.4b for the 10-minute growth sample, where two types of structures, rod and taper-shaped NWs, could clearly be identified. The tapering was quantified

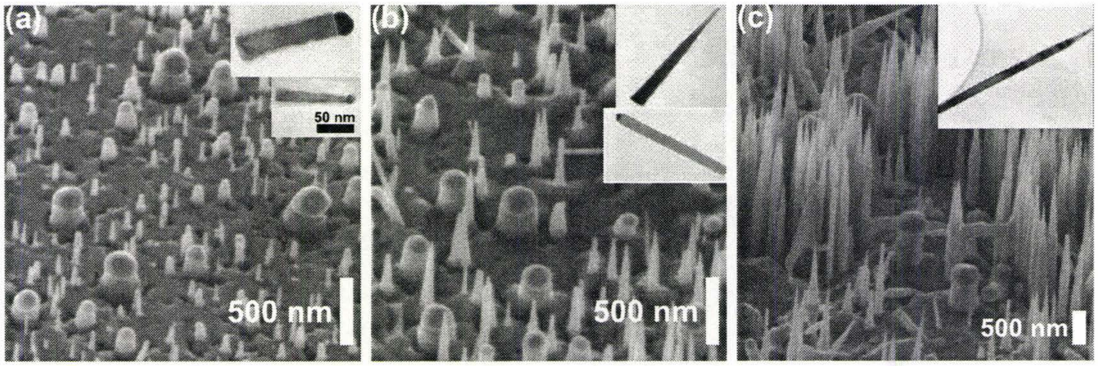

Figure 3.4: 45° tilted view of GaAs NWs grown on a GaAs (1 1 1)B substrate for (a) 3, (b) 10, and (c) 30 minutes at a temperature of 525°C and V/III ratio of ~1.5. The insets are TEM images illustrating the typical morphology of the NWs from each specimen.

using a series of SEM images such as the ones in Figure 3.4, by introducing a "tapering ratio", defined here as the ratio of the NW diameter at its base to that at its tip. Measurement of the wires was performed manually, directly on the tilted-view images, without any discrimination of morphology (i.e., tapered and non-tapered). These ratios are shown in Figure 3.5 as a function of the Au seed particle diameter D, where each data point represents a NW. After only 3 minutes of growth some tapering can already be observed. For the longer growths, note that the "tapered" characteristic refers essentially exclusively to "pencil-shaped" NWs (referring to the fact that the taper is isolated near the tip), as no other types of tapered structures were observed (e.g cone-shaped). As is emphasized in Figure 3.5, and will be further discussed in Chapter 5, there is a strong relation between tapering and the size of the particle. In general, smaller seed particles mean stronger tapering, while larger ones yield more rod-like structures. The observed range of tapering ratio for a given seed particle size is attributed to the non-uniform particle distribution associated with the synthesis method (annealing of Au thin film). While the relative position of the particle on the substrate has a direct influence on the axial growth rate of the NWs (the adatom collection area is not constant for all wires), and thus indirectly on the radial growth rate, the overall growth mechanism however remains the same.

Faceting of the NW sidewalls was characterized by top view SEM imaging (results not shown here). In the case of the shorter growths (3 and 10 minutes) the type of facets was not always clearly discernable, and in the majority of cases the NW-cross section appeared circular. When facets were present (most notable for the 10-minute growth), a predominance of $\{\bar{2}\ 1\ 1\}$-oriented ones could be established by reference to the substrate primary and secondary flats. On the other hand, for the 30- and 40-minute growths, sidewalls with clear hexagonal facets were observed, predominantly $\{\bar{1}\ 1\ 0\}$-oriented for $D < 200$ nm, while the larger diameter wires ($D > 200$ nm) often did not exhibit a clear orientation. Of particular interest is the case of strong tapering where we limit the scope of the current study to NWs with tapering ratio greater than 5, and that exhibit the $\{\bar{1}\ 1\ 0\}$-oriented facets. Figure 3.6 shows such a NW, with Au seed particle of $D \approx 8$ nm and grown for 40 minutes. Similar morphology was observed for the 30-minute growth. Two sets of facets can clearly be distinguished. While the wire base (outer diameter) has the predominant $\{\bar{1}\ 1\ 0\}$ facets mentioned above, a series of discrete layers can be distinguished in the tapered region as we move toward the NW top, where the seed particle is positioned. These layers frequently exhibited the $\{\bar{2}\ 1\ 1\}$-oriented facets, as the image in Figure 3.6 shows.

From the same top view images used for faceting identification, we concluded the SEM characterization by estimating the density of NWs on each sample. Once again, the measurements were manually performed directly on the images, and accounting for every seed particle that was visible, regardless of the underlying NW morphology. The results are summarized in Figure 3.7, which shows the density plotted as a function of the seed particle diameter for the 3-, 10-, and 40-minute growths. A shift

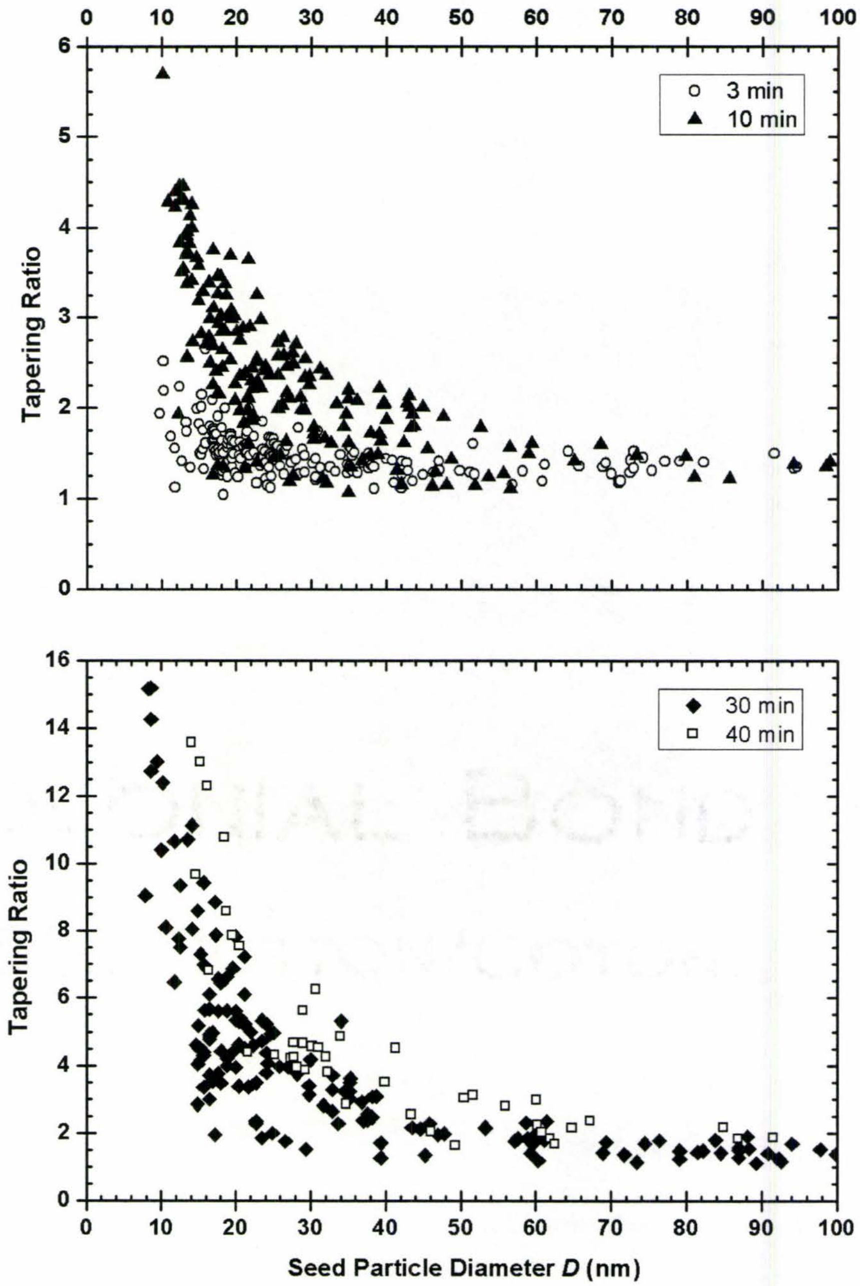

Figure 3.5: Tapering ratio (defined as the ratio of NW diameter at the base to that at the tip) as a function of the Au seed particle diameter D for various growth durations.

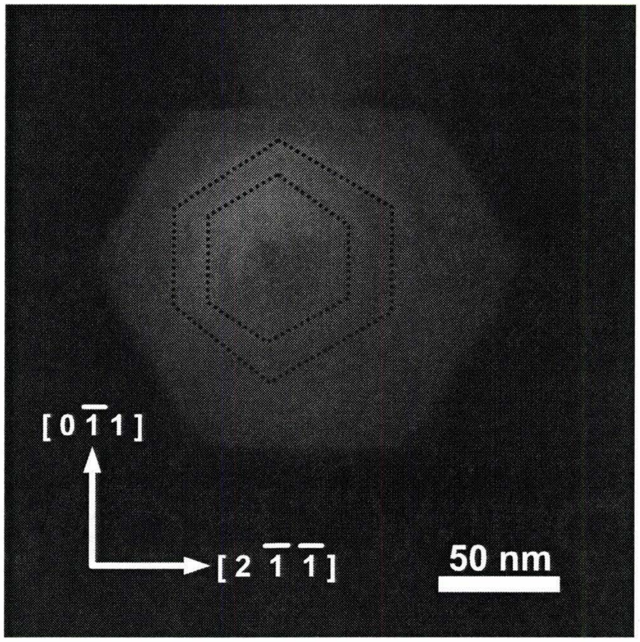

Figure 3.6: Top view SEM of a 40-minute grown GaAs NW on a GaAs (1 1 1)B substrate, revealing the transition in the sidewall faceting between the base and the tip. The axes indicate the wafer orientation defined by the substrate flats, and the dotted hexagons emphasize two of the inner facets.

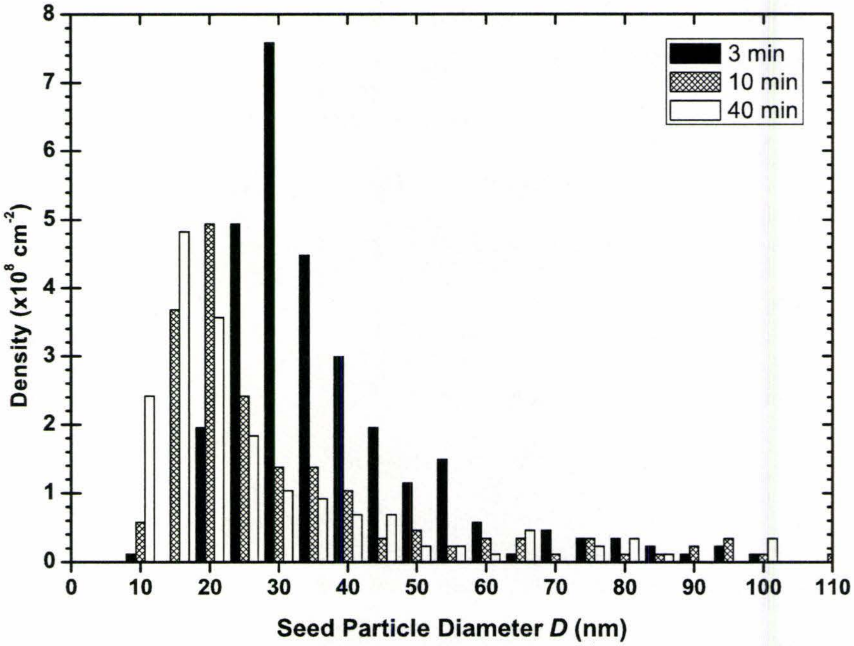

Figure 3.7: Size distribution of seed particles after 3, 10, and 40 minutes of growth.

in the distribution toward smaller particle diameter is observed as the growth evolves over time. This will be further discussed in the next section.

To investigate the nature of the tapered structure of the NWs, and simultaneously collect additional information toward an understanding of the NW growth mechanisms, further characterization by TEM was performed. A HR-TEM image from the 30-minute growth is shown in Figure 3.8a for the tapered region of a NW having a seed particle of $D \approx 15$ nm. SAED measurements performed in this region (not shown) clearly indicated that the crystal has the wurtzite structure with growth direction along $[0\ 0\ 0\ \bar{1}]$. The lines intersecting the diameter of the NW, indicated by the arrows in Figure 3.8a, are stacking faults frequently observed in NW growth. In a manner similar to what was observed in the case of GaP-GaAsP NWs (which will be discussed in Chapter 5), it appears that faults generally coincide with surface steps on the sidewall surface. Furthermore, the characteristic ABAB atomic stacking of the wurtzite crystal structure along the $[0\ 0\ 0\ \bar{1}]$ direction (the NW growth direction) can be distinguished in the regions separating each fault, as confirmed by performing Fast Fourier Transform (FFT) analysis of the image (not shown). From the atomic stacking observed in the image, the faults appeared to consist of only a few layers ($\sim$3) of atoms.

Next we compare the situation described above for the NW tip to that at the base of the NW. As previously observed in the inset of Figure 3.4c, the uniformity of the diameter in the base region of the NW is notable. Also notable is the higher density of stacking faults at the NW base as compared to the top, as illustrated by the HR-TEM image of a 30-minute grown NW taken near the base in Figure 3.8b. The linear density (number of faults per unit length) of stacking faults was on the order of 0.2 nm^{-1} in the base region, compared to $\sim$0.04 nm^{-1} in the vicinity of the tip. The principal diffraction spots in the SAED pattern measured near the base, shown in Figure 3.8c, confirmed that the dominant crystal structure of the NW base is wurtzite, identical to the NW tip. However, significant streaking of the diffraction spots along the growth direction is present due to the stacking faults. A series of satellite spots, spread between consecutive principal diffraction spots, appears superimposed on the basic wurtzite pattern, indicating a local periodicity in the stacking faults along the growth direction.

3.2.3 Discussion

As emphasized by the SEM and TEM characterization shown in Figure 3.4, and the measured tapering ratios plotted in Figure 3.5, the growth conditions favored

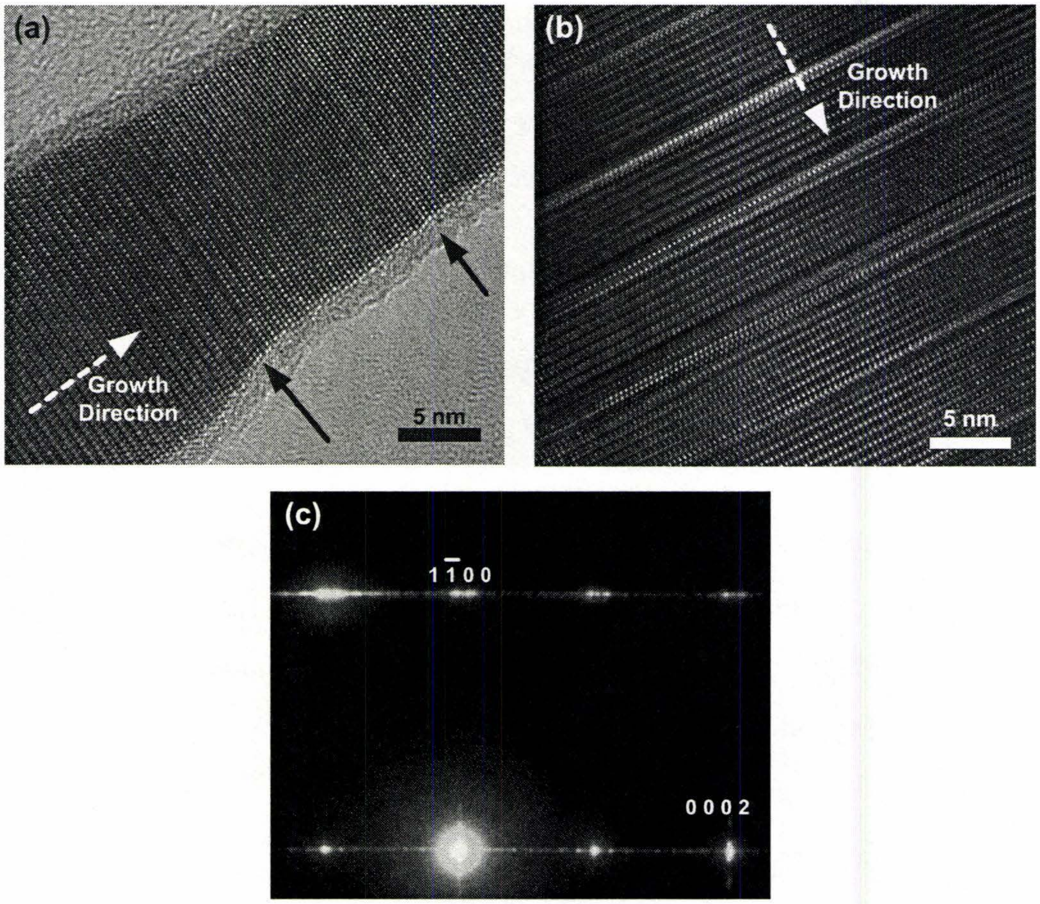

Figure 3.8: (a) Lattice-resolved HR-TEM image in the vicinity of two stacking faults in the tapered part (near the seed particle) of a 30-minute grown GaAs NW. The solid arrows indicate the location of surface steps, which appear to coincide with stacking faults. (b) HR-TEM image near the base of a 30-minute grown NW, illustrating the local pseudo-periodicity of stacking faults. (c) SAED pattern obtained near the base of a NW, revealing its fine structure. The latter is representative of the wurtzite crystal structure along the $\langle 1\ 1\ \bar{2}\ 0 \rangle$ zone axis.

a tapered NW morphology. For the two longest growths reported in this study, it is important to notice that the NW diameter is essentially constant up to a certain height from the NW base, and then reduces rapidly near the tip. We previously observed this characteristic morphology in GaP-GaAsP NWs (which will be discussed in Chapter 5), and from these observations we proposed that radial growth occurs, at some expense of axial growth, via the layer-by-layer and step-flow growth modes on the NW sidewalls similar to that for conventional 2D film growth [116]; i.e., nucleation on the sidewalls leads to island formation followed by the adsorption of adatoms at atomic steps along the island perimeters, resulting in a layer-by-layer radial growth of the NW. The observation of surface steps and ledges in the tapered region of the NW in Figure 3.8a suggests that, once significant radial growth has been initiated, a step-flow growth mode takes place in the tapered region. Adatoms diffusing along the NW sidewalls that reach the tapered region will preferentially incorporate at the step edges in a manner similar to vicinal film growth [116]. This process appears to occur at a fairly early stage of the growth under the conditions that were set, as observations made after only 3 minutes in Figures 3.4 and 3.5 suggest.

We focus now on the strongly tapered NWs obtained from the longer growths (30 and 40 minutes), where a transition in the sidewall faceting near the NW tip is clearly observed (Figure 3.6). Note that for the remainder of this discussion we shall adopt the 4-digit indexing notation for hexagonal crystals, since our TEM and SAED analysis showed that the NWs have the wurtzite crystal structure. The $[0\ \bar{1}\ 1]$ and $[2\ \bar{1}\ \bar{1}]$ axes given in Figure 3.6, corresponding to the orientation of the wires relative to the zincblende substrate, thus correspond to $[1\ \bar{2}\ 1\ 0]$ and $[1\ 0\ \bar{1}\ 0]$, respectively, in the hexagonal lattice. Essentially all the NWs in the size range of interest (i.e., $D \sim< 40$ nm) have $\{\bar{2}\ 1\ 1\ 0\}$-oriented facets at their base. However, as the NW tip is approached, a series of layers with different facet orientations appear. These are associated with the tapered part of the NW, and indicate that the latter evolves in a "digital" manner. Furthermore, the radial boundary of each layer corresponded to a step on the sidewall, which was confirmed by the TEM analysis, and shown for a typical NW in Figure 3.8a. The sidewall facets of the layers closest to the Au particle generally exhibited $\{\bar{1}\ 1\ 0\ 0\}$-oriented sidewalls. These evolved toward the $\{\bar{2}\ 1\ 1\ 0\}$ sidewalls of the NW base due to radial overgrowth. We previously speculated (as was discussed in Section 3.1) that sidewall faceting could be linked to the crystal structure. However, the SAED analysis that was performed suggests otherwise. The identical crystal structure, namely the wurtzite phase of GaAs, was obtained for both the base and tip region of the NW regardless of the different sidewall facet orientations in these two regions, in agreement with other reported MBE-grown GaAs NWs [117, 118]. Instead, the transformation of the $\{\bar{1}\ 1\ 0\ 0\}$ planes into $\{\bar{2}\ 1\ 1\ 0\}$ planes as the growth proceeds is believed to be the result of their instability, similar to the transformation from $\{\bar{2}\ 1\ 1\}$ surfaces into $\{\bar{1}\ 1\ 0\}$ surfaces observed for planar MBE growths [119,120]. Fabrication of heterostructures with core-shell geometry could then require a better understanding of the global growth mechanisms, as a detailed study performed by Sköld and co-workers showed for the AlInP-GaAs materials system, and where phase segregation occurred in certain areas of the NW cross-section [121]. These authors also observed a similar facet transformation.

NW tapering occurring in MBE growth was previously discussed by Harmand and co-workers [122], and its origin was attributed by these authors solely to the size reduction of the seed particle arising from the lowered Ga supersaturation at the end of the growth. Another tapering mechanism may occur via migration of Au on the NW sidewalls and the substrate, giving rise to particle coarsening as was previously described in the case of Si NWs grown by low-pressure chemical vapor deposition [123]. On the basis of the present work, we believe that the diffusion-limited layer-by-layer radial growth should also be considered, and moreover dominates under the growth conditions used in this study. If lowered Ga supersaturation or Au coarsening were the only factor contributing to tapering, then the tapering ratios reported in Figure 3.5 would suggest that the seed particle was significantly larger before the onset of tapering. For example, Figure 3.5 indicates that a typical 40-minute grown NW with $D \approx 15$ nm (after growth) would have had a seed particle that was initially 10 – 12 times larger, suggesting either a considerable amount of Ga in the particle at the onset of the growth, or a significant depletion of the Au as the growth proceeds. Contrary to this, Figure 3.7 revealed that the peak seed particle size distribution shifted from $D \approx 30$ nm after 3 minutes of growth to $D \approx 15$ nm after 40 minutes, which could account for a typical tapering ratio of only 2, not 10 – 12 as observed in Figure 3.5. This suggests that Ga depletion or particle coarsening may indeed take place, but not to the extent required to fully explain the measured tapering ratio. Consequently, radial growth appears to be a major contribution in the NW morphology evolution.

The pseudo-periodicity of stacking faults was revealed in the NWs by HR-TEM (Figures 3.8b-c), where we can clearly distinguish the ABAB atomic stacking of the wurtzite phase, briefly interrupted by a defect before it returns to the initial ABAB sequence. The HR-TEM images allowed us to identify the ABCABC sequence corresponding to the zincblende crystal structure. The fine structure (superlattice spots) in the SAED results of Figure 3.8c indicates a pseudo-periodicity in the stacking faults of the NW base, similar to that observed by Xiong and co-workers for III-V NWs grown by pulsed laser vaporization [124]. Note that the pseudo-periodicity in the stacking faults evolves (spatial period becomes longer), and seems for the most part to disappear as the growth progresses, as the two images in Figure 3.8a-b taken in two different areas of a NW show. The presence of steps on the sidewall surface as we approach the tip was discussed previously in light of radial growth, but in addition we notice that the step coincides with a stacking fault. We thus speculate that the stacking faults constitute a barrier to adatom diffusion on the sidewalls, and act as a preferential site for nucleation during radial growth.

The above characterization of stacking faults in the NWs, coupled to the evolution of their morphology over time, can lead to a significantly enhanced understanding of the NW growth history. Based on these results, we thus propose a sequential description of the events constituting the growth of a typical NW. Our approach is similar to what was presented in recent work on periodically twinned NWs [124, 125]. The key element in the metal-assisted growth of nanostructures is the seed particle itself, whose role is to act as a local collector of growth species that guides the anisotropic growth [58]. Any variation in its size and/or shape should therefore have an impact on the crystal growing underneath. It is well established that the seed particle is fed with growth species via two sources: direct impingement on its surface from the surrounding vapor, and migration of adatoms that reach the particle after diffusing on the substrate surface and along the surface sidewalls (see Section 3.1). As suggested by the higher density of faults near the base, the particle supersaturation is most likely subjected to fairly rapid fluctuations in the early stage of the growth, when this double income of material is at its peak (i.e., the NW is short enough that the adatoms within the collection area reach the particle). A possible origin for the faults could reside in the difference between the nucleation rate at the particle-NW interface and the diffusion of growth species through the droplet. Following the same argument as given in Reference [125], we assume here that crystallization at the particle-NW interface is faster than the intra-particle diffusion of the group III and V atoms. The following steady-state sequence is thus proposed:

(i) The NW initially grows with the wurtzite crystal structure, and has a circular cross-section. Based on some analysis done by other groups, it appears that the wire material and growth play a major role [22, 58] in the crystal structure adopted by the NW. More recently, a thermodynamic argument based on the location of the nucleus under the particle was also presented by Glas and Harmand to explain the origin of the non-stable wurtzite phase in III-V NWs [126].

(ii) As material builds up due to diffusion of growth species through the seed particle, a change in shape and surface area of the particle is induced. Such a change was notably observed in-situ during the growth of carbon nanofibre [127].

(iii) The total energy of the system consequently increases until a certain point, where the stored energy is released by inducing a change in the crystal structure of the growing wire to zincblende (the stacking fault).

(iv) This change is however only momentary, as after a few monolayers of zincblende crystal structure constituting the fault, the seed particle returns to its previous conformation and the wire returns to a wurtzite structure. Once the NW attain a certain height, the circular cross-section becomes hexagonal as the $\{\bar{1}\ 1\ 0\ 0\}$ sidewall facets form. A full understanding of the facet formation has not yet been established, beyond the fact that it is assumed to be related to the energetics of the system.

The above sequence is repeated as long as the supersaturation of the seed particle is not affected by the limited diffusion of surface adatoms, thus inducing a local pseudo-periodicity in the formation of faults. However, as the growth proceeds and the NW gets longer, fewer adatoms from the substrate surface reach the particle to the profit of radial growth, and the supersaturation of the particle changes. This is most likely accompanied by a slight diameter reduction of the seed particle as shown in Figure 3.7. A new steady-state regime is reached, and a similar sequence of events as the one described above takes place. However, since the material build-up in the seed particle depends almost solely on direct impingement, the process is slower and thus faults form less frequently. As layers form on the sidewalls, the facets transition from $\{\bar{1}\ 1\ 0\ 0\}$ to $\{\bar{2}\ 1\ 1\ 0\}$. It is worth mentioning that the dangling bond density of a $\{\bar{1}\ 1\ 0\ 0\}$ surface is on the order of 11 nm^{-2} (average between A and B surfaces, both present on a faceted NW), while it is close to 9 nm^{-2} for $\{\bar{2}\ 1\ 1\ 0\}$ (same for A and B surfaces). This could then be at the origin of the observed transition.

3.3 Chapter Summary

The Au-assisted growth of GaAs NWs on GaAs (1 1 1)B surfaces has been investigated as a function of the temperature, and the size of the Au seed particle. Two distinct growth regimes with different growth rate dependencies were observed when the diameter of the particle varied from ~20 nm to 800 nm. The critical size D_{oi} at which this transition occurred was found to be ~105 to 130 nm depending on the growth conditions. The height H_w of the wires originating from particles that are smaller than this critical diameter is driven by the diffusion of the growth species from the surrounding 2D surface up to the tip of the wire, as exhibited by the typical $H_w \propto 1/D$ dependence of diffusion-induced growth. The wire growth rates exceeded the limit expected by the V/III flux ratio, indicating the contribution of both group III and V species in the diffusion process. For larger particle diameters ($D > D_{oi}$), growth by surface diffusion becomes negligible and direct impingement of the growth species on the Au particle, followed by bulk diffusion through the particle, appears to dominate. A transition from mononuclear- to polynuclear-mediated growth under the Au particle could be at the origin of the observed height increase with increasing particle size.

The time evolution of the NW morphology was also studied. Radial growth was identified as a major mechanism contributing to the tapering observed near the tip of the NWs, thus complementing the Ga depletion in the seed particle that was previously assumed to solely explain this morphology [122]. SEM showed that the tapered tip exhibits different facets than the base of the wire, resulting from the transformation of the $\{\bar{1}\ 1\ 0\ 0\}$ surface into the $\{\bar{2}\ 1\ 1\ 0\}$ surface during planar growth of the NW sidewalls. These results further support a growth model that we previously proposed (Reference [82], which will also be covered in Chapter 5), and bring to light important considerations for the practical realization of NW-based devices. For instance, the fabrication of heterostructures with core-shell geometry requires a thorough understanding of the global growth mechanisms taking place, including the radial growth described in this study.

To complement the morphological information gained on GaAs NWs, the nature and frequency of defects in the NWs were investigated. Pseudo-periodicity of stacking faults was observed, especially in the vicinity of the NW base. Our observations on the NW morphology after different growth durations, coupled to the change in the fault linear density along the wire, provided information that allowed speculation of a possible sequence of events taking place as the growth of a typical NW proceeds.

Chapter 4

Control of Morphology and Crystal Structure

4.1 Introduction

Much effort has been invested in recent years toward a better understanding of the various mechanisms operating during the growth of NWs, which is essential if one aspires to control their structures. These studies have notably highlighted the influence of growth parameters on the NW morphology [54, 77, 128]. On the theoretical side, analytical descriptions of the process, showing good correlation with experiments, have been derived [60, 129]. These clearly revealed that the self-assembly of the crystal is primarily governed by the diffusion of growth species from the sidewalls and the substrate surface toward the NW tip.

While the effects of growth temperature have been widely investigated, much fewer studies have been done on the role of group V species in the NW growth process. Building on recent observations on InAs NW growths by MOVPE [42], we investigated the effects on GaAs NWs of varying the temperature, V/III flux ratio, and Ga impingement rate during GS-MBE growth. This comprehensive investigation on the effects of growth parameters focuses on the morphology and crystal structure of the resulting NWs, providing new insights on the various growth mechanisms. The essential (GaAs results, Section 4.2) of this chapter was previously published in

Nanotechnology [81], while Section 4.3 reports on preliminary results (unpublished) on the InAs material system.

4.2 GaAs

4.2.1 Experimental Details

The surfaces of n-type (111)B-oriented GaAs substrates were initially prepared following the process described in Section 3.2.1. A 1-nm layer of Au was deposited at room temperature in an electron-beam evaporator equipped with a quartz crystal to monitor the thickness. Prior to the actual GS-MBE growth, each substrate was submitted, under ultra-high vacuum conditions, to a 15-minute degas at a temperature of 300°C, followed by annealing at 550°C for 10 minutes to activate the formation of the seed particles on the surface. Oxide desorption was performed using an inductively coupled hydrogen plasma source, while an As_2 flux ensured that the surface stoichiometry was preserved. After setting the temperature and As_2 flux to the desired values, the NW synthesis was initiated by opening the Ga effusion cell shutter.

Multiple NW samples were fabricated, each under a specific set of three parameters: growth temperature ranging between 400 and 600°C, Ga flux yielding equivalent 2D growth rates between 0.07 and 0.28 nm/s (as determined from previous thin film calibrations on GaAs (1 0 0) substrates), and impinging V/III flux ratios between 1.1 and 4.6. In all cases the growth duration was determined such that the nominal amount of material deposited was equivalent to a 500 nm-thick epilayer. The growth conditions of the samples described in this chapter are summarized in Table 4.1.

Table 4.1: Growth conditions for the samples discussed in this chapter.

Sample	Temperature, T °C	V/III Flux Ratio, ϕ	2D Growth Rate nm/s	Growth #
A	400	1.1	0.28	504
B	400	2.3	0.28	505
C	500	1.7	0.28	506
D	500	2.3	0.28	516
E	600	1.1	0.28	507
F	600	1.7	0.28	577
G	600	2.3	0.28	508
H	600	2.3	0.14	543
I	600	2.3	0.07	643
J	600	4.6	0.14	517

The morphology of the NWs on the as-grown samples was characterized using a JEOL JSM-7000F FE-SEM, operated at an accelerating voltage between 3 and 15 kV. NW length, seed particle size, crystal structure and quantification of defects were primarily investigated with a Philips CM12 CTEM operated at 120 kV in bright field conditions. A more detailed description of the crystal structure required the use of a JEOL JEM-2010F HR-TEM, which was equipped with an EDX spectrometer for the compositional measurements of the Au seed particle. For the TEM analysis the samples were prepared by a sonication method in the same manner as described in Section 3.2.1.

4.2.2 Results

(Throughout this section the reader may refer to Table 4.2 on page 87 for a summary of the results.)

For the first set of experiments, the nominal 2D growth rate was kept constant at 0.28 nm/s and the V/III flux ratio ϕ between 1.1 and 2.3. Figure 4.1 shows SEM cross-sectional views of samples grown at T = 400°C and 500°C for different ϕ values

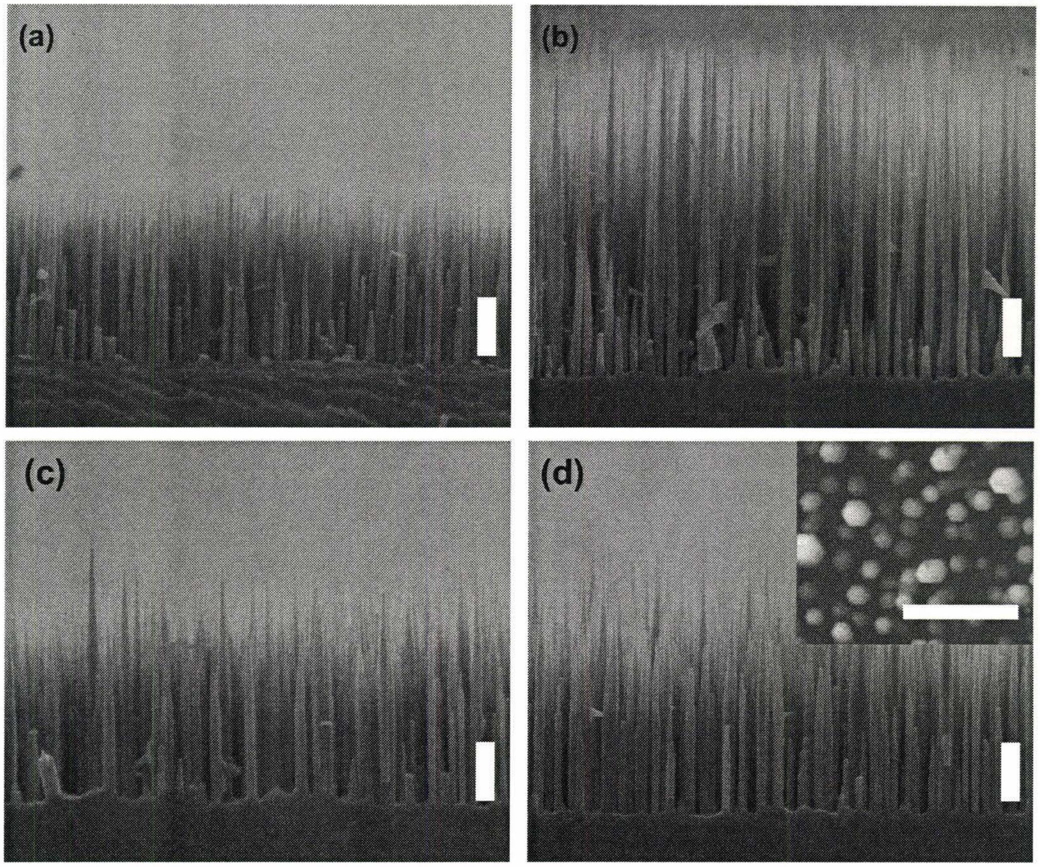

Figure 4.1: Cross-sectional SEM views of specimens after growth at a nominal 2D rate of 0.28 nm/s and: (a) $T = 400°\text{C}$, $\phi = 1.1$ (sample A); (b) $T = 400°\text{C}$, $\phi = 2.3$ (sample B); (c) $T = 500°\text{C}$, $\phi = 1.7$ (sample C); (d) $T = 500°\text{C}$, $\phi = 2.3$ (sample D). The inset in (d) is a typical top view from sample D. Length bars indicate 500 nm.

(corresponding to samples A – D described in Table 4.1). Essentially all the NWs under these conditions grew perpendicular to the substrate surface. First, we focus on the results obtained at 400°C. The NW density on the substrate surface derived from plan view SEM images, such as the inset in Figure 4.1d, was estimated to be on the order of $(8.0\text{–}10) \times 10^9$ cm^{-2} for samples A and B ($T = 400°\text{C}$).

Due to the small size of the Au particle at the NW tip, TEM, rather than SEM, was used to assess the relationship between NW height H_w and diameter D of the

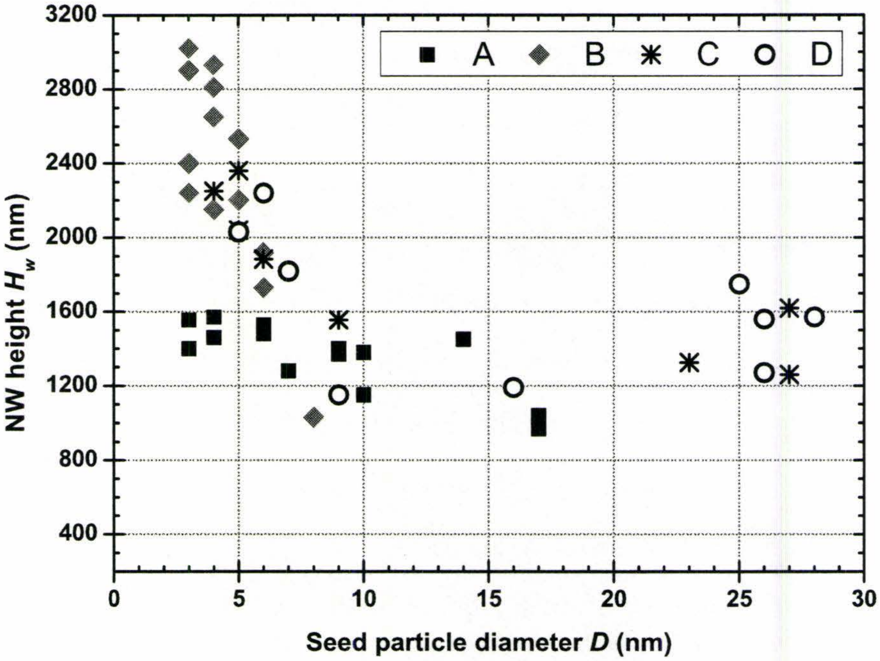

Figure 4.2: NW height as a function of the seed particle diameter, measured at growth temperatures of 400 and 500°C, and V/III flux ratio between 1.1 and 2.3 (nominal 2D growth rate of 0.28 nm/s). The labels indicate the samples as described in Table 4.1. Each data point represents a measurement made by TEM on a single NW.

seed particle, as shown in Figure 4.2 for the two temperatures of interest. Consistent with the results discussed in Section 3.1, H_w decreased with increasing D, which is a signature of growth by diffusion of adatoms [60,129]. At T = 400 °C, the growth rate increased with the flux ratio, as is clearly revealed by comparing Figures 4.1a and b, and the corresponding data points in Figure 4.2. For instance, in the case of NWs originating from seed particles with D in the range of 4 to 6 nm, the estimated mean growth rate increased from ~0.8 nm/s for sample A, up to ~1.2 nm/s for sample B.

In both cases the general NW morphology showed a decreasing diameter near the NW tip (i.e., the NW was tapered). We previously referred to these morphologies as "pencil-shaped" (Section 3.2). As was then pointed out, the tapering occurs because some of the species impinging on the substrate or directly on the NW sidewalls (since the effusion cells of the MBE system make an angle of ~35° with the substrate surface) do not reach the tip due to limited adatom diffusion. The NWs seeded from the smallest particles typically exhibited not only a strong and long taper toward the tip similar to the previous pencil morphology, but also what we refer to as a "reversed taper", i.e., a regular decrease in diameter toward the base (see Figure 4.3). We believe this is a result of the very high surface density of the NWs where shadowing from neighboring NWs could limit the direct impingement near each NW base [77]. Growth would thus be fed almost exclusively from the direct impingement flux near the Au particle when a critical NW length is reached. The adatom diffusion toward the base would then be limited, with adatoms finding nucleation sites on the sidewalls before reaching the base.

Consistent with published results on MBE-grown GaAs NWs [117,126,130], and also discussed in the previous chapter, SAED analysis on individual NWs confirmed that the wurtzite phase was the dominant crystal structure in all the NWs that were characterized (independent of T, ϕ, or growth rate). Contrast stripes intersecting the NW as evident in the TEM images (for example, Figure 4.3) can be attributed to the presence of stacking faults where the ABABAB... atomic stacking sequence of the wurtzite crystal structure was periodically interrupted by a few monolayers of the zincblende ABCABC... arrangement). At the current temperature of interest (400°C), stacking faults occurred over the entire length of the NWs, although less frequently (on the order of 0.05 nm^{-1}) for $\phi = 1.1$ than $\phi = 2.3$ (> 0.2 nm^{-1}).

Raising the growth temperature to 500°C slightly decreased the NW density to $\sim 6.7 \times 10^9$ cm^{-2} (samples C and D). Density variations are partly associated with the temperature-dependent coalescence of Au, and will be further elaborated in the

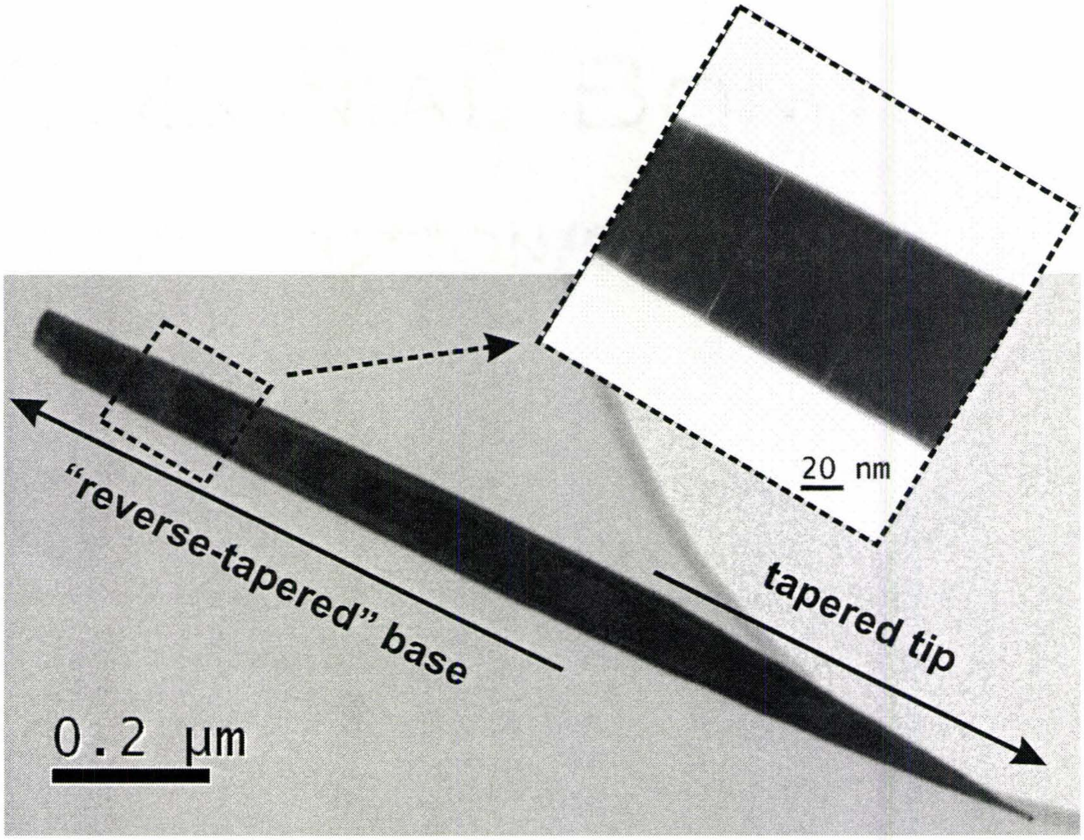

Figure 4.3: Typical morphology exhibited by NWs grown at a temperature of 400°C, and a nominal 2D growth rate of 0.28 nm/s. Two opposing tapering effects can be distinguished: toward the tip, and toward the base. The inset shows a higher magnification of a NW segment containing stacking faults, characterized by contrast stripes.

next section. The NW morphology was similar to the one observed at 400°C; that is, both the tip and base exhibited the tapering presented above. As in the previous case, these two tapering modes were typically more dominant in NWs seeded from the smallest particles ($D < 20$ nm). Height measurements in Figure 4.2 revealed that the growth rates for both samples C and D were essentially the same over a range of D between 4 and 30 nm. For a direct comparison with samples A and B previously discussed, NWs with $D = 4$–6 nm grew at a mean rate of ~1.2 nm/s for samples C and D, similar to sample B. In addition, for Au seed particles with diameters in the 4 – 6 nm range, the resulting NW diameters (the largest diameter measured along the length) were on average 12 nm greater for sample D compared to sample C. Comparing the NW lengths and diameters at 500°C, it therefore appears that higher V/III flux ratios result in greater radial growth of the NWs at the expense of axial growth and growth on the substrate surface due to the reduced mobility of the adatoms on the sidewalls. Note that this is opposite of what is observed at 400°C, where increasing the V/III flux ratio resulted in greater NW axial growth rates. These trends will be discussed further below. Stacking faults at 500°C occurred over the entire length of the NWs, with an estimated frequency as low as 0.03 nm^{-1}, and exceeding 0.3 nm^{-1} in the most extreme cases (~0.1 nm^{-1} on average), independent of the flux ratio.

For the two temperatures presented so far, NW growth occurred over the entire range of flux ratio, resulting more or less in a similar morphology (where sidewall growth is important with significant tapering), and a crystal structure with comparable defect densities. Upon raising the growth temperature to 600°C, with the nominal 2D growth rate set to the same value as for the previous scenarios (0.28 nm/s), the results became more sensitive to the V/III flux ratio, as illustrated in Figures 4.4a-c. Firstly, the NW density increased with flux ratio ϕ. At $\phi = 1.1$ (sample E), the NWs were not uniformly distributed, leaving large bare areas on the substrate, which on average resulted in a NW density of $\sim 0.2 \times 10^9$ cm^{-2}. The NW density increased to $\sim 0.6 \times 10^9$ cm^{-2} as the flux ratio was raised to 1.7 (sample F), but again the distribution did not appear very uniform, with a noticeable fraction of NWs growing non-orthogonally (tilted) with respect to the substrate surface, and some NWs even showing a kinked morphology. Raising the flux ratio to 2.3 (sample G) resulted in a more uniform NW distribution of $\sim 3.8 \times 10^9$ cm^{-2} (a six-fold increase compared to sample F), essentially all growing perpendicular to the surface.

Cross-sectional SEM imaging clearly indicated an evolution in the NW morphology with flux ratio. At the lower end of the spectrum ($\phi = 1.1$, sample E), the small number of NWs predominantly exhibited a short conical shape. Increasing the group V flux to give $\phi = 1.7$ (sample F) generally improved the morphology for the NWs that grew perpendicular to the substrate surface. Tapering, when occurring, was localized near the tip (typically not further than 100 nm from the Au particle, but extended in the most extreme cases to ~300 nm), resulting in the pencil-shaped morphology. Rod-shaped NWs (with a uniform diameter throughout the entire length) were also observed with roughly equal abundance as the tapered NWs. It is interesting to note that in the rod-shaped NWs, stacking faults were mostly found in the bottom third part of the NWs, with a fault density ranging from 0.06 to 0.2 nm^{-1} (0.1 nm^{-1} on average), making the NWs defect-free over several hundreds of nanometers. Tapered NWs, on the other hand, had faults occurring over the entire length, with an estimated average density of ~0.14 nm^{-1}.

Upon raising the group V flux so ϕ reaches its maximum value of 2.3 at the same 0.28 nm/s growth rate (sample G), a more regular reaction at the seed particles appeared to be established, where essentially all the NWs grew perpendicular to the substrate surface. As was the case for sample F, both pencil- and rod-shaped NWs could be identified. The latter morphology yielded an improved crystal structure

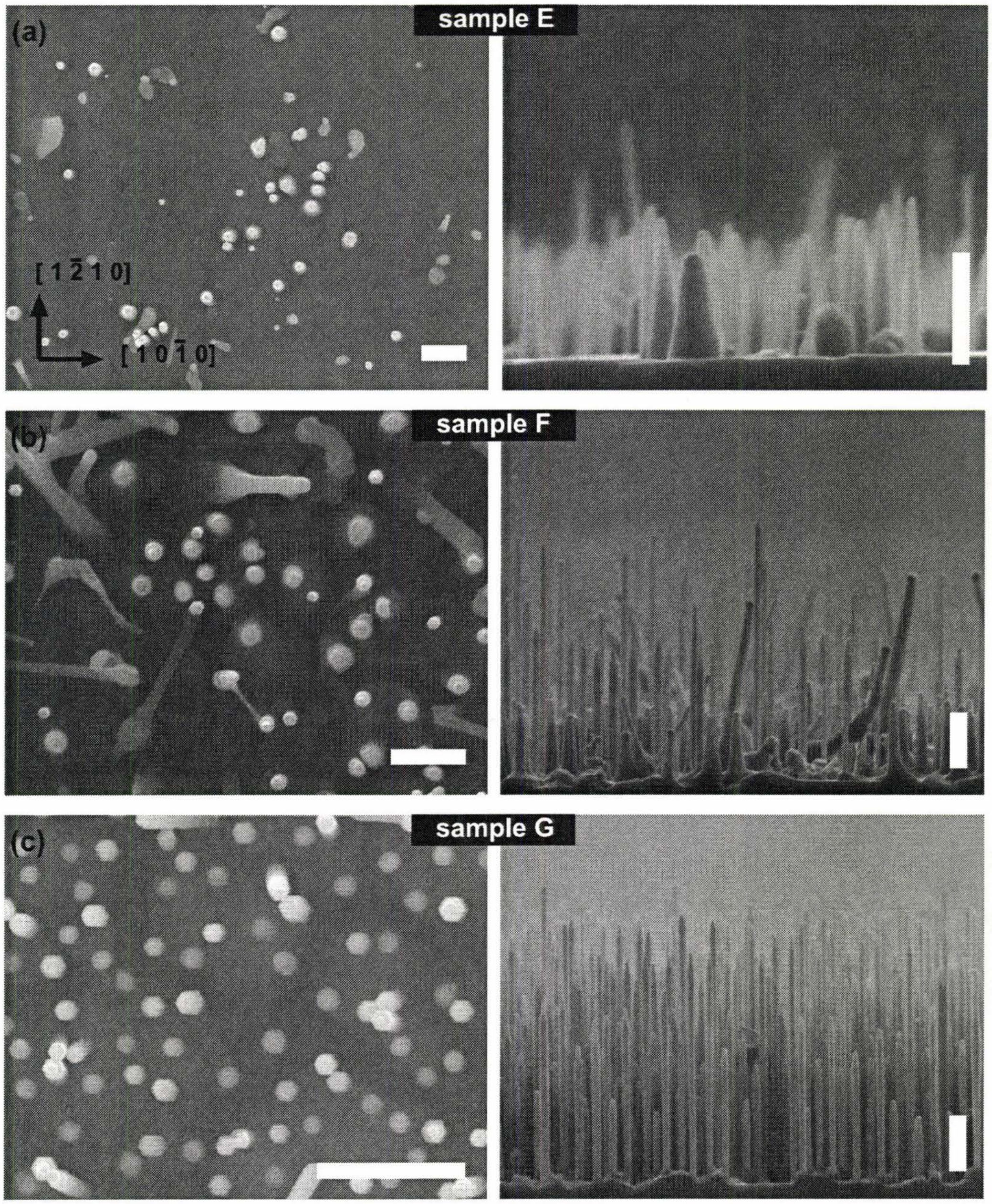

Figure 4.4: Evolution of the NW density and morphology for a growth temperature of $T = 600°\text{C}$, as a function of the V/III flux ratio and the nominal growth rate (as indicated in Table 4.1 for each sample). The axes in (a) represent the orientation of the substrate surface and apply to all cases. All length bars indicate 500 nm. (continued on next page)

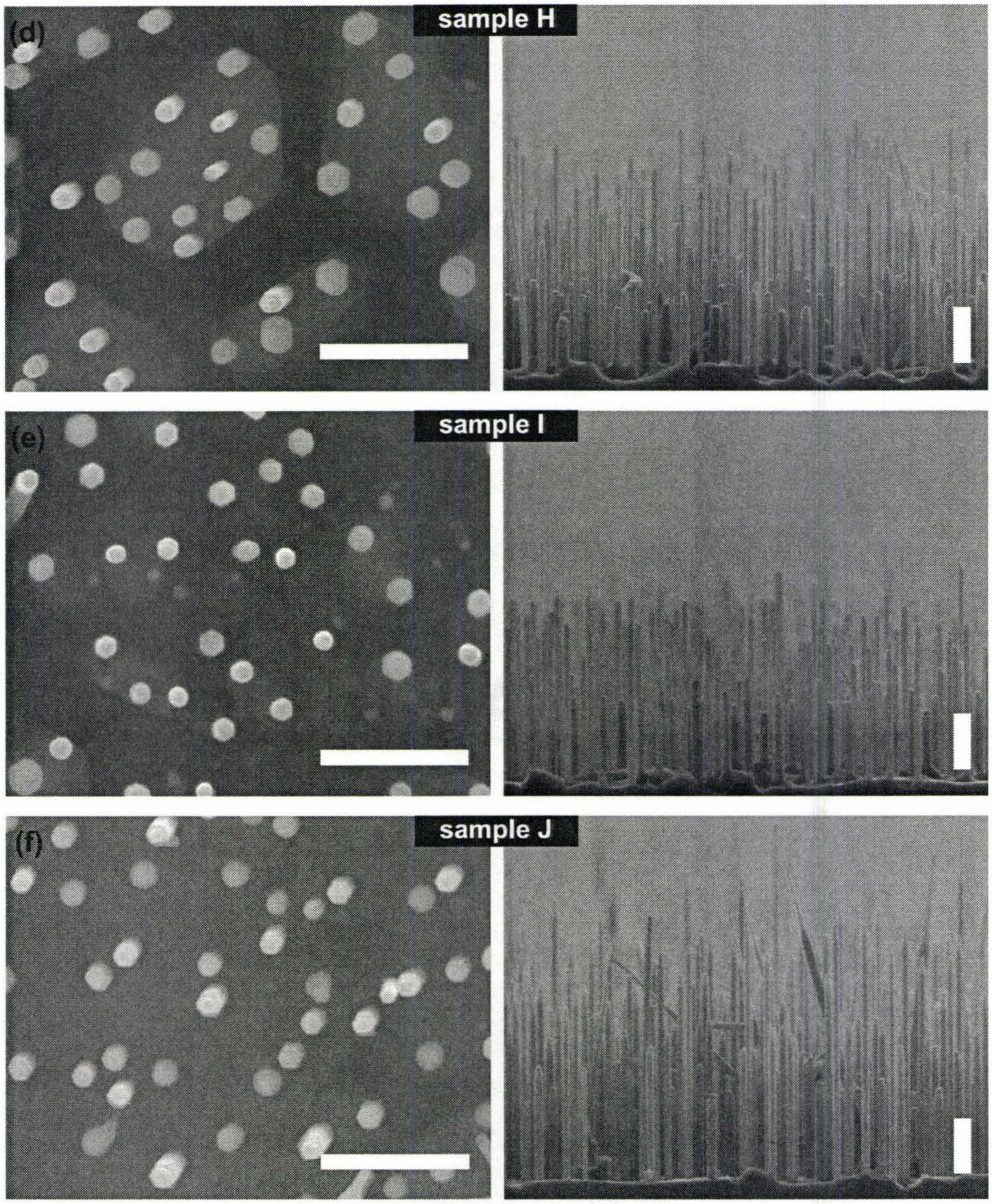

Figure 4.4: (cont.) Evolution of the NW density and morphology for a growth temperature of $T = 600°\mathrm{C}$, as a function of the V/III flux ratio and the nominal growth rate (as indicated in Table 4.1 for each sample). All length bars indicate 500 nm.

(mean fault density < 0.02 nm^{-1}), and even in the case of tapered NWs the faults occurred at a rate of $\sim$0.03 nm^{-1}, more than a 4-fold improvement compared to similar structures from sample F.

The length measurements for samples E, F, and G obtained directly from TEM analysis are summarized in Figure 4.4a. Note that, due to the nature of the NW morphologies discussed above, the expected dependence of H_w with D (i.e., H_w decreasing with increasing D) was only clearly established when ϕ was increased to 2.3 (sample G), which also makes the NWs grow faster.

Plan view SEM images as in Figures 4.1d (inset) and 4.4 revealed predominantly the $\{\bar{2}\ 1\ 1\ 0\}$ family of sidewall facet planes for all NW samples considered thus far. Our previous studies indicated that this is a marker of significant sidewall growth, consistent with the tapered morphology (Section 3.2).

Next, keeping the substrate temperature at 600°C, the temperature of the Ga effusion cell was set to yield a 2D nominal growth rate of 0.14 nm/s (half the value of all samples discussed thus far), while the As_2 flux was adjusted accordingly to maintain $\phi = 2.3$ (sample H). In this case, the same total amount of material was deposited as for the previous growths (i.e., equivalent to a 500 nm epilayer). Typical top and cross-sectional views are shown in Figure 4.4d. The NW density was $\sim 1.5 \times 10^9$ cm^{-2}, more than a factor 2 lower than sample G (grown under the same T and ϕ conditions). Interestingly, the length of the NWs does not seem to be significantly affected by the difference in Ga flux (see Figure 4.4). However, looking more closely at NWs with a given diameter, a shape change from pencil (sample G) to rod (sample H) morphologies can be observed. This phenomenon is illustrated in Figure 4.6a for samples G and H for the case of $D = 32 \pm 2$ nm. For this value of D, the NW diameter was estimated by TEM to be $\sim$68 nm on average for sample G, and $\sim$54 nm for sample H, indicating more sidewall growth for the former sam-

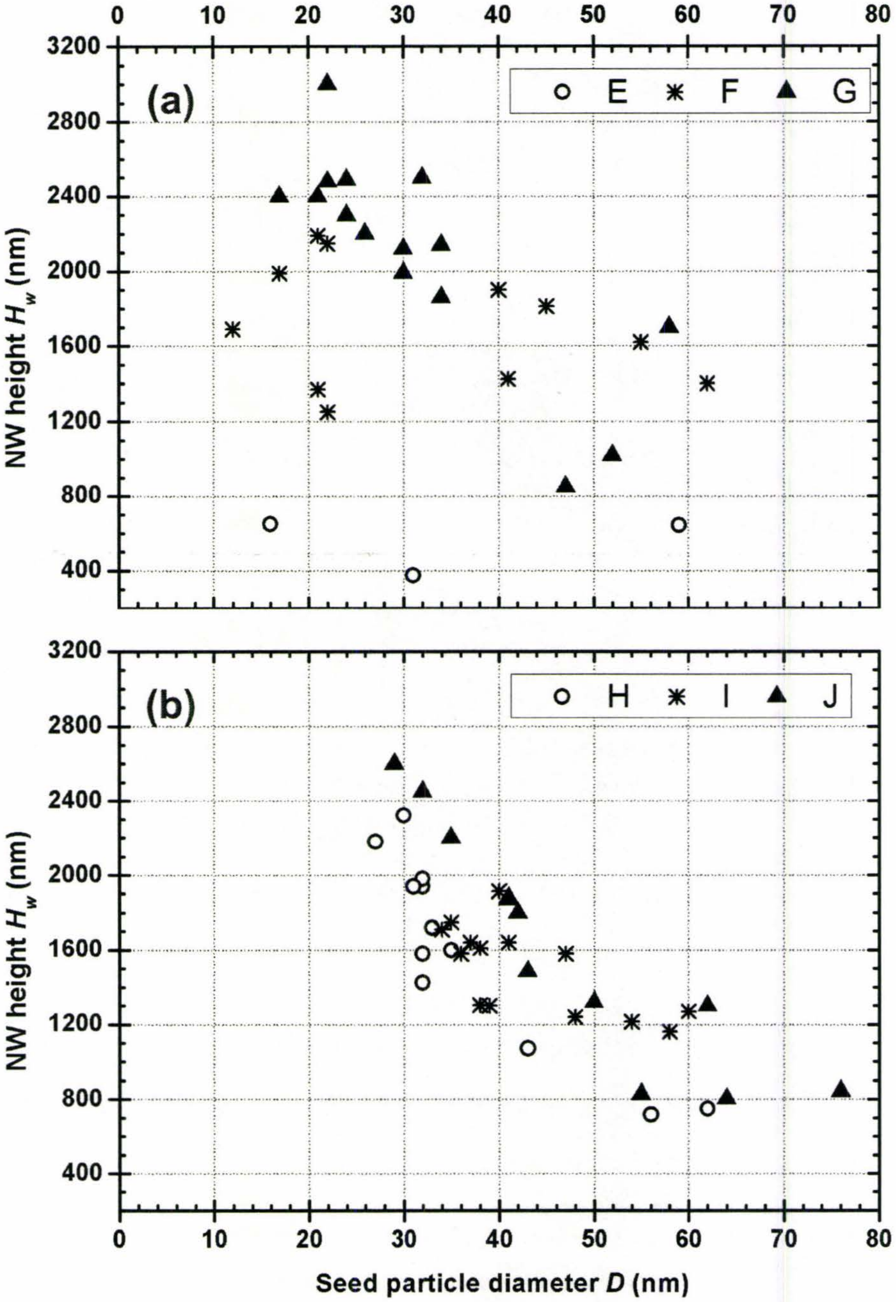

Figure 4.5: NW height as a function of the seed particle diameter, measured at a growth temperature of 600°C, and various combinations of V/III flux ratio and nominal 2D growth rate. The labels indicate the samples as described in Table 4.1. Each data point represents a measurement made by TEM on a single NW.

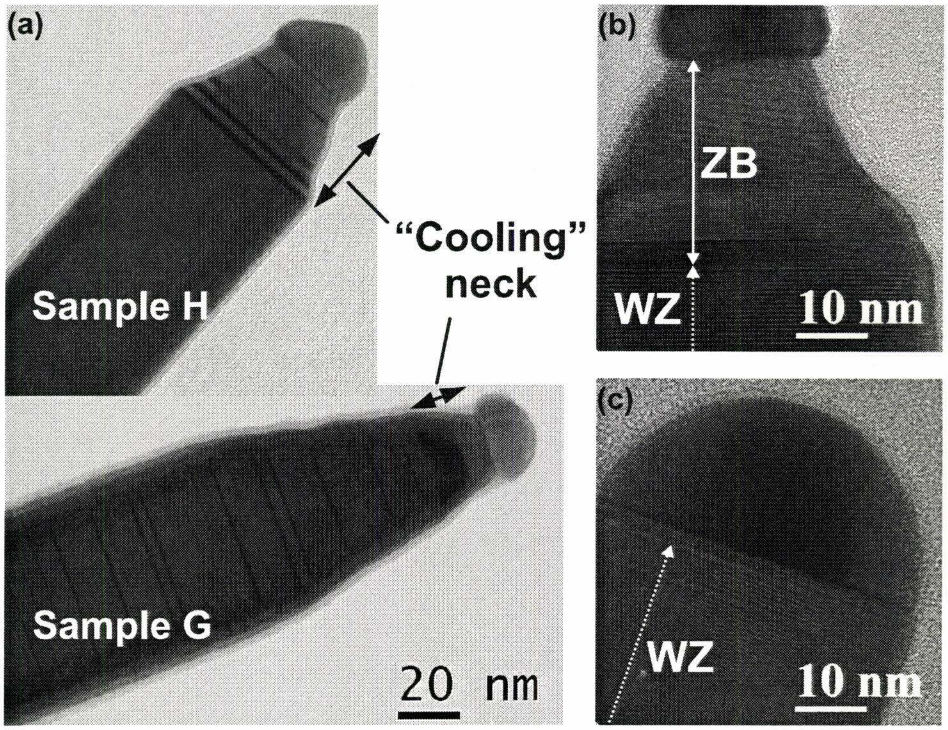

Figure 4.6: (a) Effect of Ga flux on NW morphology at $T = 600°\text{C}$ and $\phi = 2.3$. For NWs with $D \approx 32$ nm, a nominal 2D growth rate of 0.28 nm/s (sample G) yields a pencil shape morphology, while a rod is obtained at 0.14 nm/s (sample H). (b,c) HR-TEM images taken in the vicinity of the particle when the specimen is: (b) slowly cooled off under an As_2 overpressure (sample H); (c) quenched, and the As_2 flux is terminated simultaneously with the Ga flux (same growth conditions as sample G).

ple. Moreover, while the dominant sidewall facet type was $\{\bar{2}\ 1\ 1\ 0\}$ for sample G, the facets were $\{\bar{1}\ 1\ 0\ 0\}$ for sample H. As was indicated in Section 3.2, the latter indicates limited sidewall growth, consistent with the rod morphology of sample H.

Closer inspection by TEM of samples G and H revealed a subtlety in morphology near the NW tip. While sample H was mostly rod-shaped with virtually no tapering, the tip of the NW directly beneath the Au particle revealed a sharp "neck" typically observed in GaAs NWs [34]. This can be attributed to the cooling period after the growth is interrupted by terminating the Ga flux while still maintaining the As_2

overpressure (Figure 4.6b). The Ga is purged out of the seed particle by crystallizing with the arsenic from the applied As_2 overpressure. EDX performed on the particle confirmed that no measurable amount of Ga or As could be detected in the Au particle after the growth. Furthermore, FFT analysis on HR-TEM images of the neck region indicated a zincblende crystal structure as compared to the wurtzite body of the NW, consistent with previous observations of the "cooling neck" [34]. For sample G, the cooling neck was also visible along with the more gradual tapering associated with the sidewall growth present at the higher growth rate. In contrast, quenching the specimen after growth (growth #633, with the same conditions as sample G but for a shorter duration), while terminating both the As_2 and Ga fluxes simultaneously, essentially resulted in the disappearance of the cooling neck (thus confirming its origin), and a more hemispherical shape of the particle (Figure 4.6c). Furthermore, EDX measurements revealed that the Au particle contained on the order of ~40 – 45 at. % of Ga in this case. Characterization of the NW morphology from this sample (not shown here) however revealed roughening of the sidewall surfaces due to desorption of As during cooling.

Remarkably, a very low density of defects was also achieved in sample H compared to all the growths presented thus far. For the body of these rod-shaped NWs the stacking fault density was estimated at ~ 0.008 nm^{-1} on average (range was 0.0001 – 0.03 nm^{-1}). With further lowering of the nominal growth rate to 0.07 nm/s (sample I), the rod-shaped morphology was maintained, consistent once again with the $\{\bar{1}\ 1\ 0\ 0\}$ dominant sidewall facets (Figure 4.4e). The NW density on the surface in this scenario was $\sim 1.7 \times 10^9$ cm^{-2}, similar to sample H. While the average fault density was estimated to be on the same order of magnitude as the latter sample, defect-free NWs could be observed, unlike NWs grown under the other conditions.

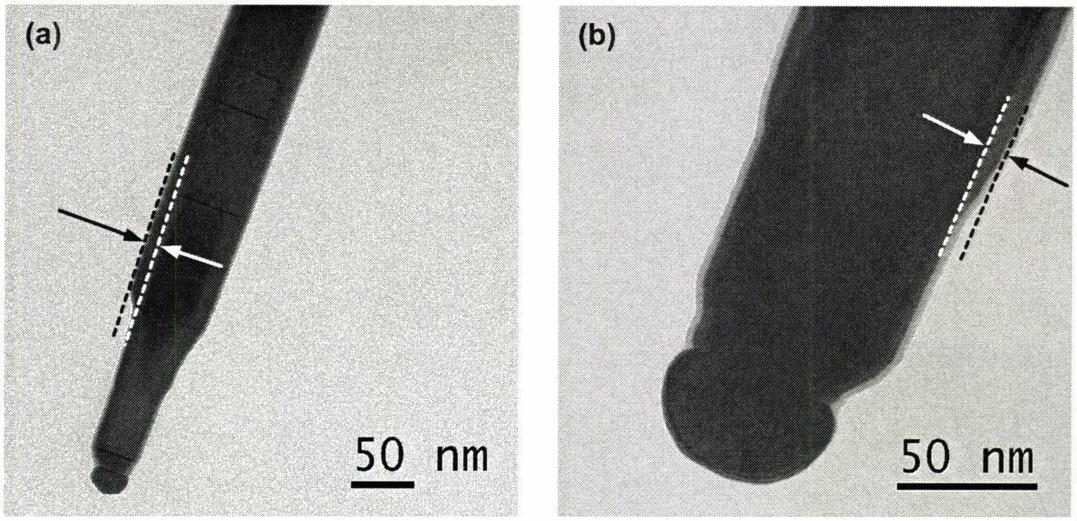

Figure 4.7: Typical NWs from sample J for (a) $D \approx 29$ nm and (b) $D \approx 64$ nm. Dashed lines indicate radial growth of the NW.

Using the combination of high temperature and moderate growth rate (0.14 nm/s), the flux ratio was doubled to a value of 4.6 (sample J). Under these conditions, the NW surface density was measured at $\sim 2.2 \times 10^9$ cm^{-2} (Figure 4.4f). The higher density of As_2 on the surface will limit the migration of Ga adatoms. The experimental observations clearly revealed that the NWs grew axially in a diffusion-induced manner as the H_w vs. D relationship plotted in Figure 4.4b suggests. The resulting morphology (Figure 4.7) exhibited a uniform diameter that was slightly greater than the Au seed particle, indicating uniform radial growth. Note that the same "cooling neck" as described above was also observed. Compared to samples H and I, the dominant facet type was $\{\bar{2}\ 1\ 1\ 0\}$ indicative of the uniform sidewall growth, and the average defect density was on the order of $\sim$0.01 nm^{-1}.

As a mean to recapitulate the evolution of NW desnity, stacking fault density, morphology, and facet type as a function of the growth conditions, the results presented above are summarized in Table 4.2.

Table 4.2: Summary of SEM and TEM observations

Sample	NW density $\times 10^9$ cm^{-2}	Fault density nm^{-1}	Morphology	Dominant facets
A	10	0.05	long tapered tip + reverse taper	$\{\bar{2}\ 1\ 1\ 0\}$
B	8.0	> 0.2	long tapered tip + reverse taper	$\{\bar{2}\ 1\ 1\ 0\}$
C	6.8	0.1	long tapered tip + reverse taper	$\{\bar{2}\ 1\ 1\ 0\}$
D	6.6	0.1	long tapered tip + reverse taper	$\{\bar{2}\ 1\ 1\ 0\}$
E	0.2	0.02 – 0.1	short, conical, low surface coverage	$\{\bar{2}\ 1\ 1\ 0\}$
F	0.6	0.14	tilted, kinked, "pencil", or rod, low surface coverage	$\{\bar{2}\ 1\ 1\ 0\}$
G	3.8	0.06 – 0.2	"pencil", or rod	$\{\bar{2}\ 1\ 1\ 0\}$
H	1.5	0.008	rod	$\{\bar{1}\ 1\ 0\ 0\}$
I	1.7	0.01	rod	$\{\bar{1}\ 1\ 0\ 0\}$
J	2.2	0.01	rod, with uniform radial growth	$\{\bar{2}\ 1\ 1\ 0\}$

4.2.3 Discussion

The large variation in the NW surface density that was observed among the different samples is first discussed. It is clear that, despite the same pre-growth annealing conditions, the setting of the growth conditions modified the seed particle size distribution. Previous studies indicated that, with increasing temperature, the mobility of Au on the GaAs (1 1 1)B surface increases, resulting in coalescence and thus larger particles on average as well as a smaller density [79]. This is consistent with our observations that the NW density was essentially constant for a given growth temperature in the case of $T = 400$°C (samples A and B) and $T = 500$°C (samples C and D), and with the lowering of density with increasing temperature. In the case of 600°C (samples E – G), the NW growth appeared to be inhibited except at the highest V/III flux ratio. This is almost certainly due to the desorption of group V species at the elevated temperature, which could be corrected by supplying more group V flux. This point is discussed further below. The lower growth rate samples (H – J) showed a lower surface density compared to sample G. This difference cannot be attributed to temperature, as these samples were all grown at 600°C. In addition, the temperature ramp rate and delay time before opening the Ga shutter were nominally identical in all of these samples; therefore, the different surface densities are not likely attributed to different pre-growth annealing conditions of the Au. Although not entirely understood at present, the initial phase of NW growth could be one contributing factor in the growth rate dependence of the NW surface densities. NW growth is initiated upon supersaturation of the Au particle with Ga adatoms. When the Ga shutter is opened, the Au particle accumulates Ga adatoms and eventually becomes supersaturated. Upon supersaturation, nucleation occurs at the Au-semiconductor interface, initiating the growth of the NW. The reduced flux of Ga adatoms at a lower growth rate implies a longer time to reach the supersaturation concentration and a longer delay before the onset of NW growth. A similar phenomenon was previously observed in the case of Si NWs [131]. During this delay time, further coalescence of the Au seeds may occur resulting in the observed lowering of NW density.

Focusing now on the morphology and crystal structure of the NWs obtained under the various growth conditions, we first turn our attention to the results obtained at the lowest temperatures. Starting with $T = 400°\text{C}$, Figure 4.2 indicated that despite the reduction in the Ga adatom diffusion length expected from the increase in the arsenic pressure [132], the NWs grew axially faster for sample B compared to A by a factor of 1.5. Due to the accumulation of Ga in the Au particle in the VLS mechanism, it is probable that the effective V/III flux ratio at the particle-NW interface is lower than unity, thus limiting the axial growth rate of NWs by the supply of As_2. Increasing the V/III impingement flux ratio (sample B) would therefore increase the NW axial growth rate as observed. Similar dependence of growth rate with group V pressure was also observed for Ga-assisted MBE growth of GaAs NWs [133], and a similar model has been proposed for GaN NWs [134]. The group V-limited aspect of the growth has also been observed for GaSb NWs synthesized by MOVPE [135].

Interestingly, raising the growth temperature to 500°C did not result in longer NWs. Moreover, the average growth rate appeared to be independent of the flux ratio (see series C and D in Figure 4.2) for the two values investigated ($\phi = 1.7$, 2.3). This is most likely due to an increase in radial growth at the highest ϕ (at the expense of axial and film growth), as direct measurements of NW diameters (for identical Au particle sizes) on the TEM images confirmed.

For $T = 600°\text{C}$ and nominal growth rate of 0.28 nm/s (samples E – G, Figures 4.4a-c), the surface density increased with V/III flux ratio. Note that NW growth was never completely inhibited, but the low density of NWs resulting from high temperature and low V/III ratio (sample E) are certainly indications that a large fraction of the seed particles did not result in NW growth and probably became buried under the 2D film growing simultaneously between the NWs. Although the incident V/III flux ratios exceeded unity in all cases, the actual ratio at the NW tip likely differs from the impinging flux due, as pointed out above, to the accumulation of Ga in the particle, and the differences in desorption rates of Ga compared to As_2 at 600°C (see for instance Figure 2.6 in reference [136]). Thus for $\phi = 1.1$ and 1.7, the effective flux ratio at the particle-substrate interface was severely limited by As_2 supply.

Under the conditions of 600°C and flux ratio of 2.3, a better control of morphology and crystal structure can be achieved when the effective 2D growth rate (i.e., the group III flux) is lowered to 0.14 nm/s (half the previous value). The shape change from pencil to rod (see Figure 4.6) between samples G and H, coupled to the transition in dominant sidewall facets from $\{\bar{2}\ 1\ 1\ 0\}$ to $\{\bar{1}\ 1\ 0\ 0\}$, are strong indications of more radial growth occurring in the case of higher group III flux (Section 3.2). On the previously established basis that the VLS growth is limited by group V species, the higher Ga flux (sample G) has little or no effect on axial growth above a certain level, as the V/III flux ratio in the particle is lower than unity, and instead growth on the sidewalls sets in [134]. Furthermore, the improvement by more than an order of magnitude in stacking fault density when the nominal growth rate is lowered (even to the point that defect-free wires could be obtained in sample I) suggests that either low group III supersaturation (and possibly high group V supersaturation) at the particle is required for the crystallization in the wurtzite structure [126].

In the cases where uniform radial growth is desirable, such as for the fabrication of core-shell structures, our study suggests that the most efficient strategy (in terms of final morphology and crystal structure) lies in using the conditions of sample J. Under these conditions, a uniform shell that extends close to the tip (as shown in Figure 4.7) can be deposited. Optimization of the V/III flux ratio to a value between 2.3 and 4.6 could enable fine tuning of the NW geometry between axial and sidewall growth.

4.3 Comparison with InAs

To finalize this chapter, some (unpublished) results on the InAs system are presented. Since the cost of InAs (1 1 1)B substrates is significantly higher than their

GaAs equivalents (by more than 5 times), a more cost-effective alternative was to use the efficient stress relaxation property of the NWs with respect to the underlying substrate (due their small lateral dimension). The InAs NWs were therefore grown on GaAs (1 1 1)B substrates. While time restriction prevented a more systematic study, it will already be noticed that, in light of this preliminary analysis, the generic concepts that were derived from the GaAs studies can be applied to this binary compound. Recommendations for future investigations can also be made.

4.3.1 Experimental Details

The surface of n-type GaAs (1 1 1)B substrates were first prepared in the same manner as described in Section 3.2.1. A 1-nm layer of Au was deposited at room temperature in an electron-beam evaporator equipped with a quartz crystal to monitor the thickness. After transferring the substrates (in ambient air) to the GS-MBE system, they were submitted to the following pre-growth cleaning process: degas at 300°C for 15 minutes in the preparation chamber, followed by plasma-enhanced oxide desorption/annealing in the growth chamber at 550°C, under an As_2 overpressure, for 10 minutes. After setting the temperature and As_2 flux to the desired values, the NW synthesis was initiated by opening the In effusion cell shutter.

Three samples were grown, all at a nominal 2D growth rate of 0.28 nm/s, with the temperature ranging between 400 and 460°C, and the As_2 flux set to yield a nominal V/III flux ratio of either $\sim$1.5 or $\sim$2.0. Post-growth characterization was carried out using SEM (JEOL JSM-7000F), CTEM (Philips CM12), and HR-TEM (JEOL JEM-2010F).

4.3.2 Results and Discussion

The first growth was performed at a temperature of 460°C and a nominal V/III flux ratio of ~1.5 (Growth #381), for a duration of 600 s. This temperature was first selected to be on the "hot-side" for the successful epitaxial growth of InAs epilayers by GS-MBE (based on previous experiences), because the initial plan was then to eventually fabricate InAs/GaAs heterostructures (to be discussed in Section 5.2). It was therefore desired to use a temperature as hot as possible to accommodate both materials. As is illustrated in Figure 4.8a, this combination of conditions did however not result in any NW on the surface. While the exact reasons for this result were not fully understood at the time this specimen was grown (it was obtained prior to the GaAs study presented in Section 4.2), the previous findings helped to shed some light on the possible origins. The hot temperature, yielding diffusion lengths for In adatoms that are greater than Ga [137, 138], combined with the low nominal V/III flux ratio, most likely resulted in an effective V/III flux ratio at the NW growth interface (particle – substrate) that is less than unity, and prevented the axial growth to take place under the particles. The latter thus most likely became buried under the 2D growth.

In order to increase this effective V/III flux ratio, the incoming flux of group III adatoms reaching the particle must be reduced, and/or the group V flux increased. The first strategy attempted consisted in keeping the same nominal V/III flux ratio as in the previous case (i.e., ~1.5), but decrease the substrate temperature to 430°C to reduce the diffusion length (Growth #387). As shown in Figures 4.8b and c for a 10-minute growth, these conditions yielded some NWs growing perpendicular to the surface. Notice however the small density (on the order of 0.3×10^9 cm^{-2}) compared to the GaAs NWs grown under similar conditions (see Table 4.2), something that had already been observed during the growth of InP NWs on InP (1 1 1)B

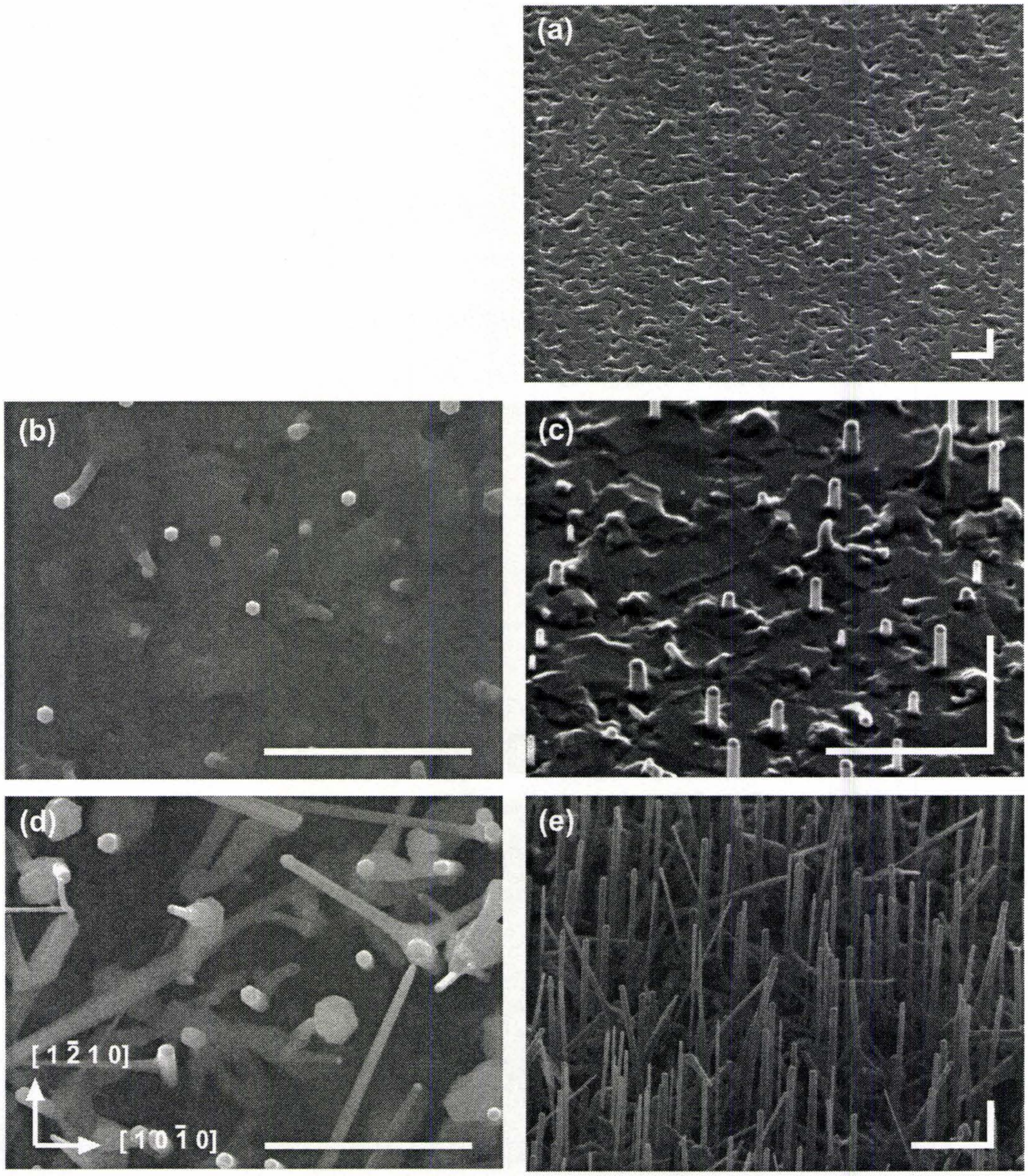

Figure 4.8: SEM images of InAs NWs grown on GaAs (1 1 1)B substrates under various temperature and V/III flux ratio conditions, and at a nominal 2D growth rate of 0.28 nm/s. (a) Tilted-view from a specimen grown at 460°C, and a V/III flux ratio of ~1.5. Top- (b) and tilted- (c) views of a specimen grown at 430°C, and V/III flux ratio of ~1.5. Top- (d) and tilted- (e) views of a specimen grown at 400°C, and V/III flux ration of ~2.0. All length bars indicate 1μm. The axes indicating the crystalline orientation in (d) are the same for (b).

substrates [139]. Decreasing the growth temperature to 400°C, and increasing the As_2 flux so as to yield a nominal V/III flux ratio of ~2.0 (Growth #551), resulted in the surface shown in Figures 4.8d and e (after 30 minutes of growth). The net increase in NW surface density under this set of conditions provides a good indication that the group V-limited aspect of the growth can explain the trend observed. While in this scenario a significant number of NWs grew perpendicular to the substrate surface, a non-negligible fraction were tilted, with various angles. This result is somewhat similar to the GaAs Sample F (see Figure 4.4b). The origin of these structures is not fully understood at the moment; additional characterization (e.g. cross-sectional HR-TEM analysis) would therefore be necessary in order to determine their crystalline orientation, and possibly isolate the location where tilting initiates (often at the NW base, but not in all instances). The structural information thus gained could certainly clarify the nature of such a behaviour. In analogy with the GaAs study, one can speculate that increasing the V/III flux ratio, while maintaining the temperature and growth rate, could result in vertical NWs, as observed in the transition from GaAs Sample F to G (Figures 4.4b and c, respectively).

TEM analysis confirmed that the InAs NWs grew with the wurtzite crystal structure under the latter conditions. Rod-shaped wires clearly dominated (consistent with the $\{\bar{1}\ 1\ 0\ 0\}$ facets observed in Figure 4.8d), with tapering occurring for some of the tilted wires. While further analysis would be necessary to quantify any trend, already the few NWs observed showed a very low number of stacking faults (linear density on the order of $\sim 0.001\ \text{nm}^{-1}$), concentrated in the lower segment of the NWs, making the structures defect free over lengths exceeding 2 μm. The "cooling neck" previously described (see Section 4.2) was still present, but point EDX measurements done on one particle indicated an incomplete purge of the In (about 70 at.% In after the growth). This suggests that even a greater amount may be present during the growth. Already this result diverges from previous observations done on MOVPE-grown InAs NWs, where typically 25 – 30 at.% In [41] and ~21 at.% In [140] were measured.

More work is undoubtedly necessary to fully understand this material system and optimize the growth conditions. However, it is already clear that the principles that followed from the GaAs study still apply, and therefore further generalize the proposed description.

4.4 Chapter Summary

In summary, an exhaustive study on the influence of growth conditions on GaAs NWs was conducted. It was shown that a good control of the NW morphology and its crystal structure can be achieved via the right combination of temperature, V/III flux ratio, and Ga flux. While growth can occur over a very wide temperature window, it appears that a high temperature (~600°C) may be of the greatest practical interest for device fabrication. Moreover, a relatively large amount of group V species (flux ratio ~2.3) and low group III flux (0.07 – 0.14 nm/s) is necessary for uniform diameter NWs with minimized tapering. These conditions also result in a significant decrease in, and even for some cases in complete elimination of, stacking fault occurrence. They are thus suited for the fabrication of rod-shaped NWs intended, for example, for axial homojunctions (pn-junctions) or heterostructures. On the other hand, further increase in the V/III flux ratio to 4.6 limits the adatom mobility on the surface, and consequently triggers uniform sidewall growth. This strategy could thus enable a good control in the fabrication of core-shell structures.

In addition to the practical implications of these results, this study provided additional evidence on the mechanisms operating during the growth. For one, increasing coalescence of Au with increasing temperature was observed. Additionally, the measured differences in NW densities on the specimen surfaces (at a fixed substrate temperature of 600°C) when the group III flux was altered suggested a possible incubation period between the time the growth is initiated by opening the shutter, and the time NW nucleation occurs. At the lower nominal growth rates of 0.07 and 0.14 nm/s, the seed particle supersaturation necessary for NW growth initiation would thus take a longer time to be reached (due to the lower flux of group III atoms), time during which the particles could still move on the surface and coalesce.

Consistent with MOVPE observations [42], the V/III flux ratio appeared to modify the temperature window for NW growth. At low temperature, NW growth appeared to be limited due to diffusion of group V species. At high temperatures, NW growth appeared to be limited due to desorption of As_2. In both cases, higher nominal V/III flux ratios could address this deficit. Our results suggest that axial growth of NWs was limited by As supply, and that the V/III flux ratio at the Au-NW interface is less than the nominal value.

Minimization of defects was achieved via the control of both group III and group V species. Although a detailed model was beyond the scope of the present chapter, it appears that in light of these experimental observations, mass transport of group V species and the influence of the Ga flux rates need to be included in future NW growth models under certain MBE conditions.

The principles that were drawn from this exhaustive study on the GaAs system appeared to be validated by some preliminary results obtained on InAs NWs that were grown on GaAs (1 1 1)B substrates. Notably, the group V-limited aspect of the axial growth was clearly established, and is even more obvious due to the longer diffusion length of In adatoms compared to Ga. The conditions to suppress tilted NWs, as well as to trigger radial growth in a controlled manner, remain to be investigated.

Chapter 5

Heterostructure Nanowires

While the bulk of our studies focused on single binary compound NWs (more especially GaAs, as was presented in Chapters 3 and 4), some efforts have been invested in more complex material systems involving the fabrication of heterostructures. In the first section of this chapter we therefore discuss some of the work that was done in collaboration with Chen Chen, then a postdoctoral researcher within the LaPierre group, on GaP/GaAsP heterostructure NWs. The observations that were made on this material system were pivotal in the subsequent elaboration of a quantitative model (which will be reviewed in Chapter 6). Some unpublished results on InAs/GaAs structures are also presented, focusing on possible strategies for improving the fabrication in future attempts.

5.1 GaP/GaAsP Core-Shell and Axial Heterostructures

Device applications require rational control of the NW morphology, which may be achieved by alternating between conditions that promote non-metal-assisted radial growth on the NW sidewalls as compared to VLS-type axial growth [141,142]. In this way, a variety of NW shapes may be produced (intentionally or otherwise) including straight rods, tapered rods, and conical structures. In addition to controlling the morphology of NWs, one-dimensional quantum electronic devices require the implementation of heterostructures whereby the distribution of chemical elements change abruptly along the axis or radius of the NW. Device applications requiring p-n junctions, heterostructures, and compositionally modulated superlattices are achieved by gas phase switching of the precursor source material during VLS growth.

Within the framework of this present study, our goal was to further elucidate the VLS growth mechanisms operative during GS-MBE. We focused our efforts on GaP-GaAsP segmented NWs, which are a model system for studying group V heterointerfaces (i.e., a system exhibiting a change in group V composition along the NW axis). The essentials of this section were published in an issue of the Journal of Materials Research dedicated to NWs and nanotubes [82].

5.1.1 Experimental Details

Substrates of GaAs (1 1 1)B were prepared following the same process as outlined in Section 3.2.1. In the GS-MBE system, group III species were supplied as monomers from a heated solid elemental source, and the group V species were supplied as dimers (As_2 and P_2) from a dual-filament hydride (AsH_3 and PH_3) gas cracker operating at 950°C. Before the actual growth, the Au-covered substrates were heated to a temperature of 550°C for 10 minutes under an As_2 flux to form Au nanoparticles on the surface. Simultaneous desorption of native oxide was enhanced by the use of an inductively coupled H_2 plasma source.

The growth consisted of GaP-GaAsP-GaP heterostructures (Growth #103). After oxide removal and Au nanoparticle formation, growth of NWs occurred by initiating PH_3 flow, terminating AsH_3 flow, waiting 30 seconds, then opening the Ga shutter for growth of the first GaP segment. Switching of the molecular beams at the GaAsP-on-GaP interface occurred by first shuttering the Ga beam to terminate growth of the GaP layer, initiating AsH_3 flow, setting PH_3 flow, waiting 30 seconds, and then opening the Ga shutter to initiate growth of the GaAsP layer. The As/P gas flow ratio corresponded to a two-dimensional film composition of $GaAs_{0.6}P_{0.4}$ as determined by earlier thin film calibration growths. After growth of the GaAsP segment, growth of a second GaP segment was initiated. Molecular beam switching at the GaP-on-GaAsP interface occurred by first shuttering the Ga beam to terminate growth of the GaAsP layer, setting PH_3 flow, terminating AsH_3 flow, waiting 30 seconds, then reopening the Ga shutter for growth of the final GaP segment. Growth times were 3 minutes for each GaP segment, and 24 minutes for the GaAsP segment, giving a total growth time of 30 minutes. Throughout growth, the Ga flux rate remained constant (corresponding to a 2D growth rate of 0.28 nm/s). The group V fluxes were set for a V/III flux ratio of 2.0.

After growth, the morphology of the resulting NWs was first observed with a LEO/Zeiss 1540XB SEM (in the secondary electron mode) at the university of Western Ontario (operated by Dr. Todd Simpson), before the establishment of the McMaster system. *In situ* cross sectioning of the deposited material was achieved by milling with a Ga focused ion beam (FIB). EDX then provided compositional analysis of the deposition. An incident electron beam energy of 5 keV and probe size less than 3 nm was used during EDX. Under these conditions, the electron beam is expected to be confined to the NW, thus yielding negligible background X-ray fluorescence [143].

After SEM, NWs were prepared for further analysis by TEM. NWs were removed from the GaAs substrate by sonicating in ethanol solution for 1-2 minutes. A small volume ($\sim$50 μl) of the ethanol solution was placed onto a holey carbon TEM support grid. After ethanol evaporation, NWs were found to be dispersed onto the grid as observed with a JEOL 2010F HR-TEM. EDX in the TEM provided further compositional analysis around the NW heterostructure with a probe size less than 1 nm.

5.1.2 Results

A typical top SEM view of the post-growth surface is shown in Figure 5.1. Bright dots in Figure 5.1 indicated Au at the top of NWs, which grew preferentially in the [1 1 1]B direction, normal to the substrate surface. The presence of Au at the top of the NWs was confirmed by EDX, which verified that the wires grew by a metal-assisted process. As shown in previous work (Section 3.1), and confirmed in the SEM image of Figure 5.1, the annealing process used in this study resulted in Au particles with diameters ranging between about 20 nm and 500 nm. Wire lengths, measured directly from the SEM images, were between 0.5 and 2 μm above the two-dimensional surface. It is also evident in Figure 5.1 that although the majority of NWs grew in the [1 1 1]B direction, some grew at tilted angles from the substrate. A preferred growth direction for these tilted NWs was not evident. Finally, a close examination of top SEM images revealed that the growth gave rise to NW sidewalls with six-sided faceted structures as observed previously for GaAs NWs (Chapters 3 and 4). Inspection of other SEM images (not shown) indicated that the facets were predominantly $\{\bar{1}\ 1\ 0\}$ for particle diameters below about 200 nm (see, for example, the NW labeled A in Figure 5.1), and predominantly $\{\bar{2}\ 1\ 1\}$ above this critical diameter (labeled B in Figure 5.1).

SEM images such as that in Figure 5.1, and the TEM analysis discussed below, allowed the morphology of the NWs to be classified. Some of the NWs (such as that labeled C in Figure 5.1) were strongly tapered near the tip forming a pencil-shaped morphology, while others (such as D) appeared as rods with nearly uniform diameters along their entire length. In addition to the pencil- and rod-shaped NWs, unusual kink geometries were occasionally observed such as that shown by the tilted SEM view in Figure 5.2a. EDX compositional mapping of arsenic was performed in order to locate the GaAsP-GaP heterointerfaces relative to the kink. The resulting EDX

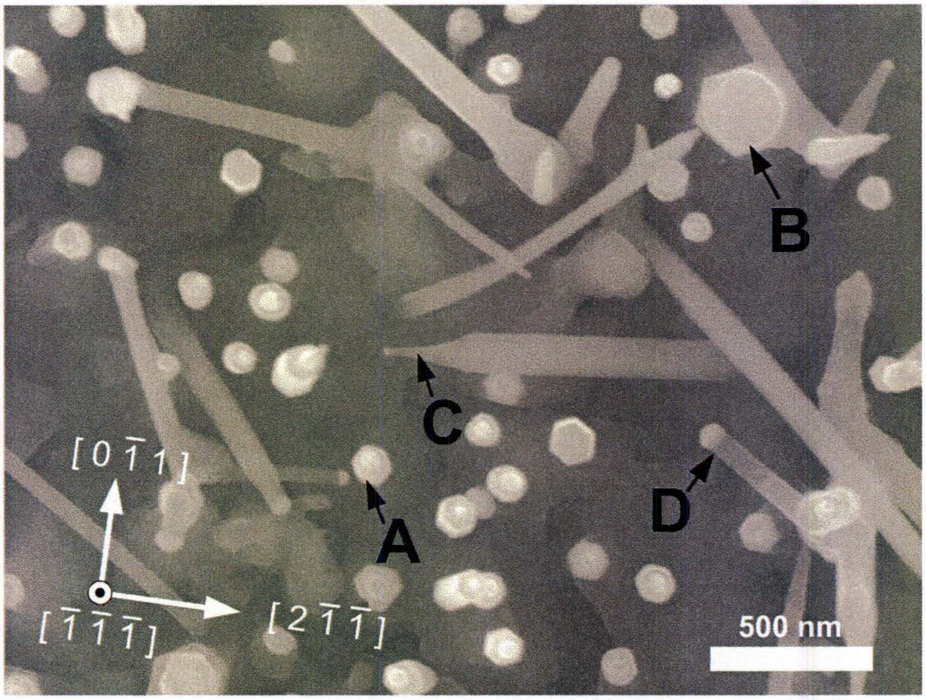

Figure 5.1: SEM top view of GaP/GaAsP NWs. NWs labeled A through D are discussed in the text.

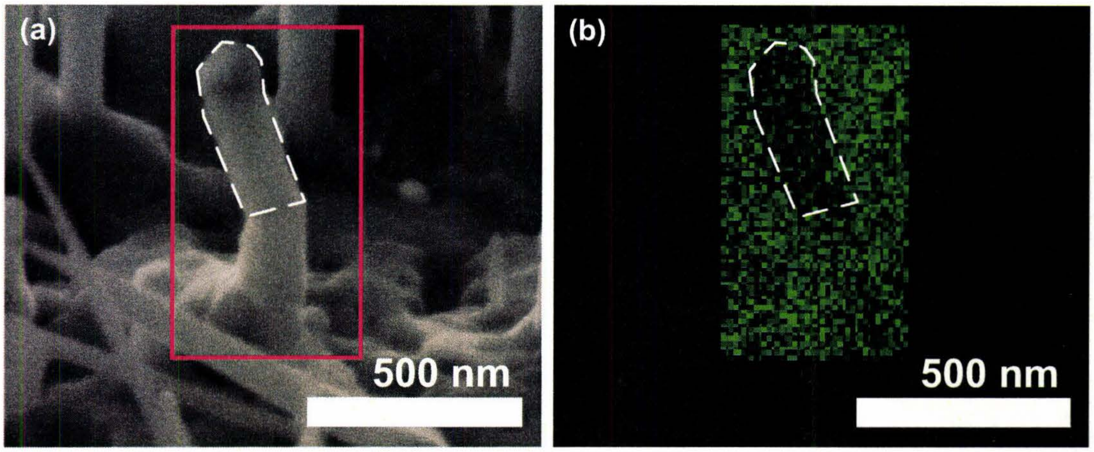

Figure 5.2: (a) Tilted SEM image of a kinked NW. (b) EDX compositional map of arsenic for the boxed area in (a). The portion of the NW above the kink (the GaP segment) has been outlined for clarity.

map of As, shown in Figure 5.2b for the boxed area in Figure 5.2a, revealed a dark region (outlined for clarity) corresponding to the GaP segment at the top of the NW. The kink is evidently co-located with the GaP-on-GaAsP heterointerface near the top of the NWs. The first heterointerface (GaAsP-on-GaP) expected near the bottom of the NWs was not evident in Figure 5.2b, due to burial in the two-dimensional film that grew non-catalytically between the NWs. Therefore, only the GaP-on-GaAsP interface, which lies near the top of the NWs and above the two-dimensional film growth, will be discussed further in this chapter.

After the SEM analysis presented above, the NWs were studied by TEM, which allowed detailed observations of the pencil- and rod-shaped NW heterostructures. First, we will consider the pencil NWs. A typical bright-field TEM image of such a structure is shown in Figure 5.3. A series of wide terraces separated by surface steps (indicated by arrows) were evident in the tapered region at the tip of the NW. The vertical lines intersecting the NWs (at the far left and right arrow) are stacking

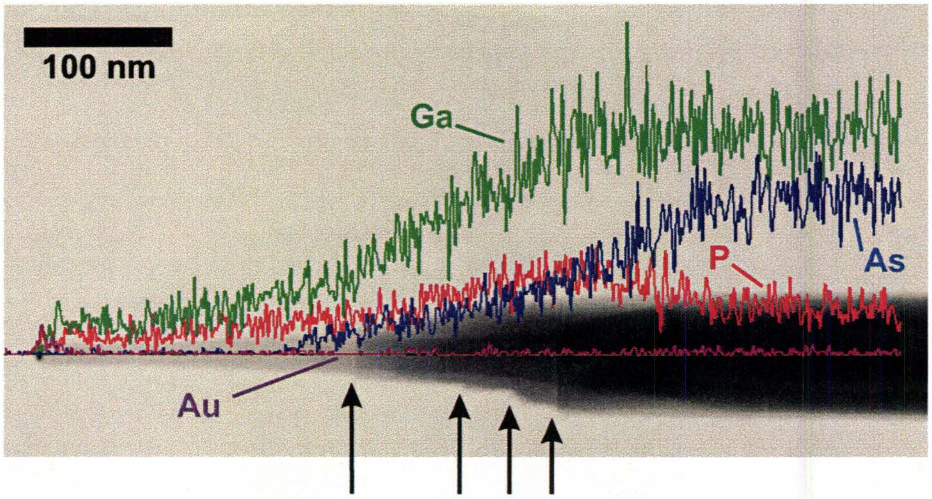

Figure 5.3: Bright-field TEM image of a pencil NW. EDX linescans of Ga (green), As (blue), P (red), and Au (purple) along the center of the NW are superimposed on the image. Arrows indicate the location of surface steps.

faults, commonly found in [1 1 1]B oriented NWs [115,144]. The stacking faults in the tapered region of our NWs appeared to coincide with the step edges, as previously established with GaAs (Section 3.2).

Next, EDX measurements were used to characterize the GaAsP-GaP heterointerface in the pencil NWs. An EDX linescan along the center of the NW is superimposed on the TEM image of Figure 5.3. Assuming the usual stoichiometric growth for Group III-V compounds, the Ga atomic percent is expected to be constant (50%) throughout the NW. A constant Ga signal (green curve) was therefore observed in the EDX linescan until the tapered region at the end of the NW was entered. At this point, the Ga signal started to decay due to the gradual reduction in material volume associated with the tapered geometry. The decrease in As (blue curve) and increase in P (red curve) along the growth direction (right to left in Figure 5.3) indicated the transition from the GaAsP to the GaP segment. A tapered contrast gradient was also evident inside the NW in Figure 5.3, indicating a core-shell structure associated with the GaAsP-GaP heterointerface. The gradual changes in As and P signals were consistent with the presence of this tapered core-shell structure.

The tapered shape of the core-shell structure in the NW of Figure 5.3 closely matched the shape of the external taper at the tip of the NW, suggesting that the tip geometry evolved only slowly during growth, at least during the top portion of the NW visible in Figure 5.3. Further evidence to support this claim was provided by the TEM and EDX analysis of other NWs with unusual morphologies. Figure 5.4, for example, shows a TEM image and corresponding EDX composition map of As for another pencil NW. The tapered morphology at the end (right side) of the NW appeared to be asymmetric; that is, skewed toward one side of the NW. The identical asymmetry was evident from the contrast (emphasized by the white short-dashed line) in the core-shell structure of the GaAsP-GaP heterointerface (Figure 5.4b and magnified view in Figure 5.4c) and the accompanying EDX composition map (Figure 5.4a). The origin of this asymmetric morphology is not clear at present, although it may arise from anisotropic mass transport, as might occur for a tilted NW. The important point is that radial growth appeared to evolve slowly in comparison to axial growth, such that the core-shell structure of the heterointerface was similar to the morphology of the NW tip.

We now turn our attention to the rod-shaped NWs, where similar TEM and EDX analysis was performed as presented in Figure 5.5. Au particles with diameter larger than 30 nm typically resulted in this type of structure, while smaller Au catalysts produced the tapered pencil NWs. In contrast with the latter (previously discussed), the EDX line scans for the rod-shaped NWs presented a Ga signal that was constant along the entire NW length until the Au catalyst was entered. The transition in As (yellow curve) and P (green curve) occurred over a length less than 7 nm, signifying an abrupt and planar GaAsP-GaP heterointerface. A close examination of Figure 5.5

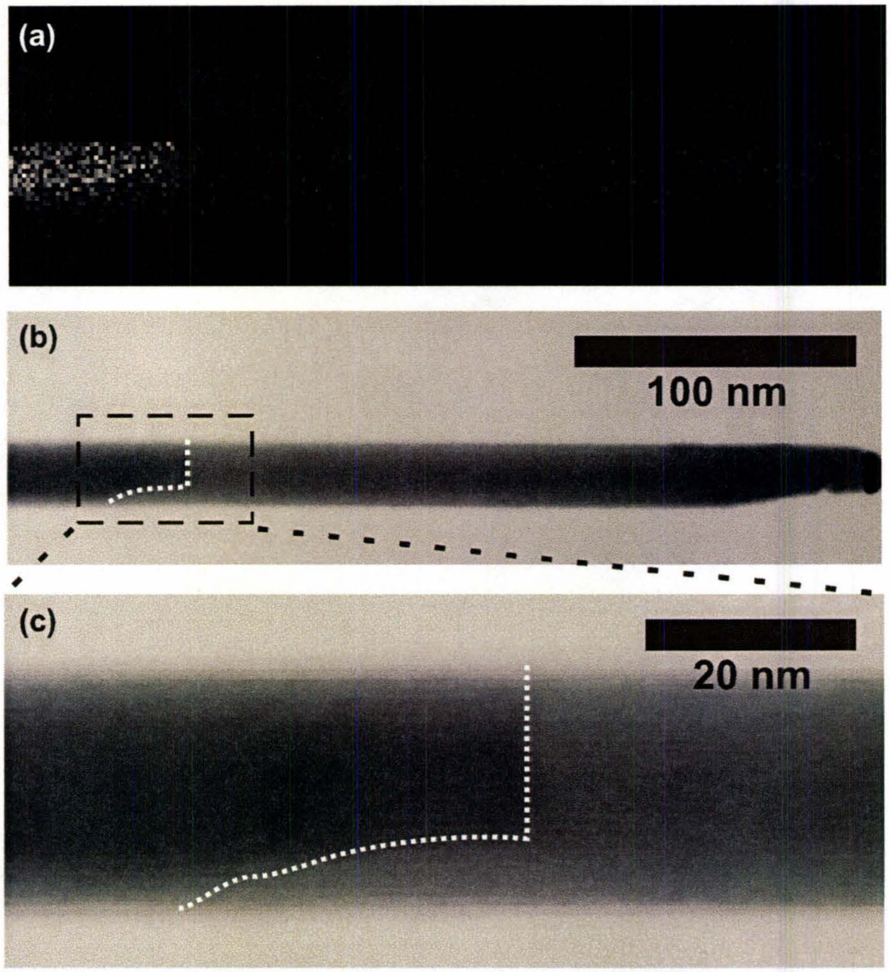

Figure 5.4: (a) EDX composition map of As and (b, c) bright-field TEM images for a pencil NW.

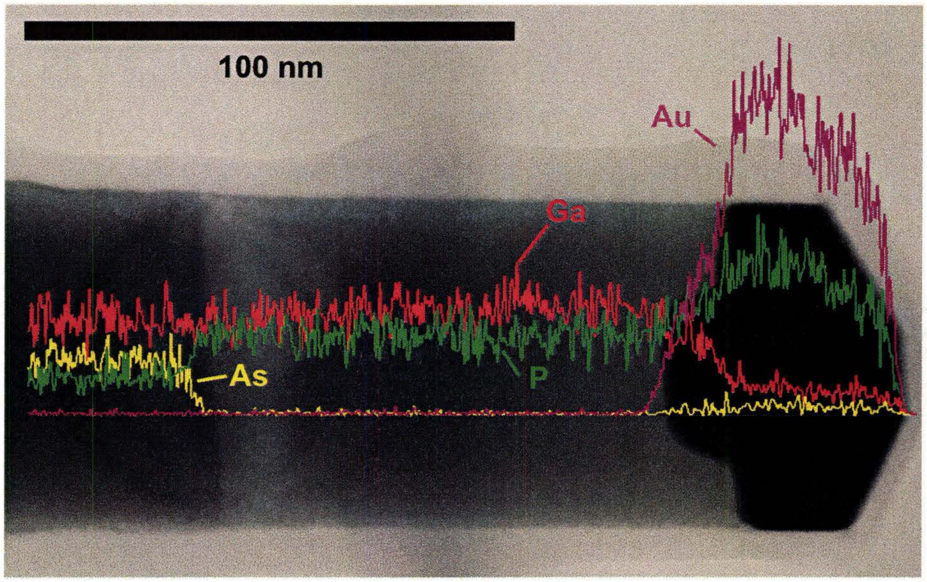

Figure 5.5: Bright-field TEM image of a rod-shaped NW. EDX linescans of Ga (red), As (yellow), P (green), and Au (purple) along the center of the NW are superimposed on the image.

revealed a circular strain field near the heterointerface, which may be attributed to the lattice mismatch strain between GaP and GaAsP, as observed previously for InAs-GaAs heterostructures [145].

Also of interest is the "mushroom" shaped facets of the Au catalyst in Figure 5.5, which to our knowledge have not been previously observed. SEM analysis indicated that the cap of the mushroom near the top of the NW exhibited a truncated octahedral shape, commonly found in Au particles [146]. More frequently, the Au particle exhibited the shape evident in Figure 5.6, also a truncated octahedron but without the base of the "mushroom". The geometry of the Au particle did not appear to influence the interface abruptness, as evident in Figure 5.5. If the Au catalyst had maintained the "mushroom" shape during growth, we might have expected a similarly shaped heterointerface. The fact that the latter was planar suggested that the Au

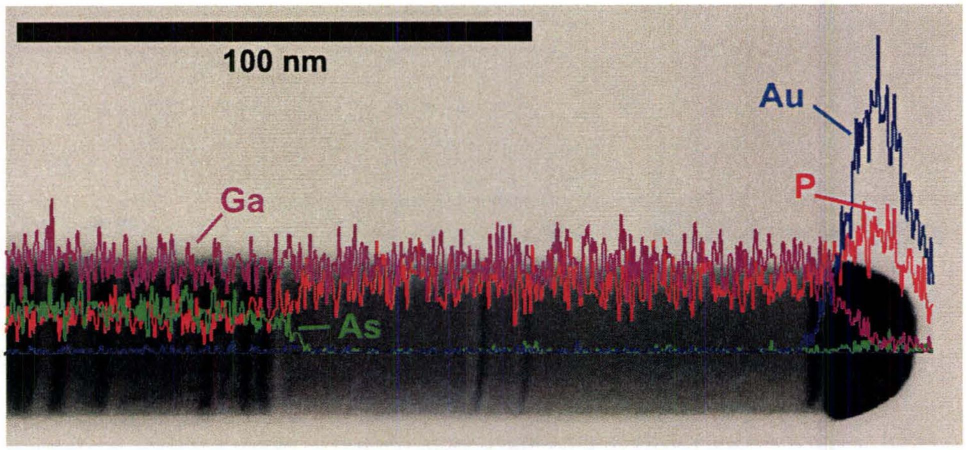

Figure 5.6: Bright-field TEM image of a rod-shaped NW showing stacking faults in GaAsP section (left portion of wire). EDX linescans for Ga (purple), As (green), P (red), and Au (blue) are superimposed on the image.

was instead liquid during growth, and the facetted structure of the Au particle was formed at lower temperatures upon cool down of a liquid Au drop. Further evidence to support this view was provided by compositional analysis of the Au catalyst, as will be discussed below.

To further examine the abruptness of the heterointerfaces in rod-shaped wires, a lattice-resolved HR-TEM image was acquired around the GaP-on-GaAsP heterointerface as shown in Figure 5.7. Further HR-TEM images across the entire width of the NW (not shown here) indicated abruptness of the interface to within several monolayers, consistent with the EDX linescans in Figure 5.5.

Our TEM observations also allowed us to observe the relative number of stacking faults in the GaAsP and GaP segments. TEM images, such as Figure 5.6, typically indicated a large number of stacking faults (dark vertical lines) in the bottom portion of the NW, while the top portion near the Au catalyst showed relatively few. The superimposed EDX linescan in Figure 5.6 indicated the location of the GaP-on-GaAsP

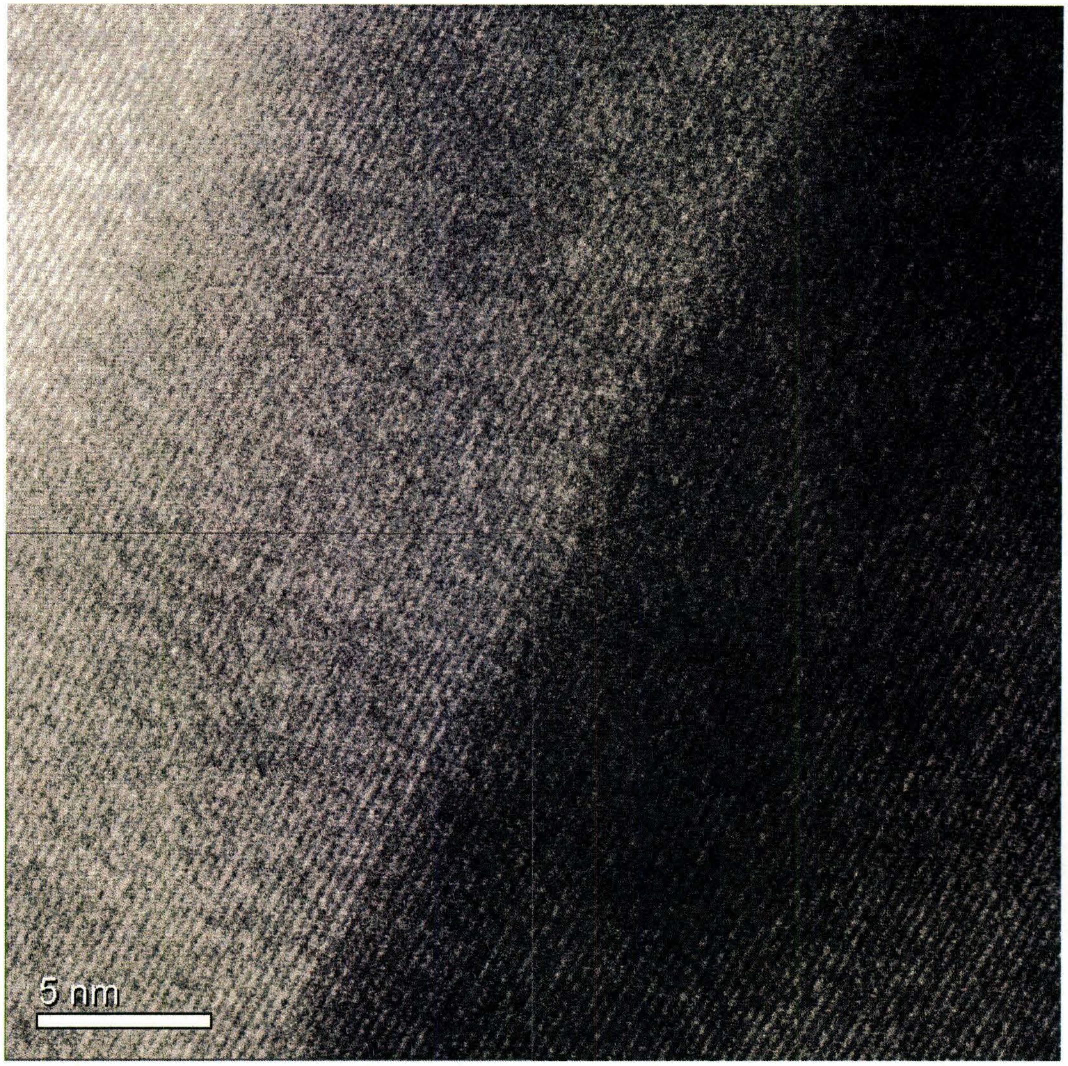

Figure 5.7: HR-TEM image of the GaP-on-GaAsP interface for the NW in Figure 5.5. The GaP section is on the left, and the GaAsP section is on the right.

heterointerface evident from the changes in As (green curve) and P signal (red curve). Hence, it can be seen that the change in stacking fault density coincided with the heterointerface, with GaAsP containing more stacking faults than GaP. On the other hand, TEM images (not shown here) of NWs with diameter less than 30 nm typically exhibited fewer stacking faults compared to larger diameter NWs.

Finally, it is interesting to note the increase in P signal in the vicinity of the Au catalyst at the end of the NWs as evident in the EDX linescans of Figures 5.5 and 5.6. This is noteworthy because all previous studies of NWs have shown that the solubility of Group V elements in Au is negligible in agreement with the Au-As and Au-P phase diagrams [147]. The P Kα1 and Au Mα1 X-rays used in these EDX linescans overlap closely in energy (2.014 and 2.123 keV, respectively). Since Au background subtraction was not performed in the raw X-ray spectra, the observed P yields near Au were anomalously high. Nevertheless, P (and some As) were clearly observed in the vicinity of Au. To precisely locate the group V elements, a NW was cross-sectioned by an *in situ* FIB in the SEM. A tilted view SEM image of a cross-sectioned wire is shown in Figure 5.8. The negligible solubility of group V elements in Au was confirmed by EDX point measurements in the cross-sectioned Au particle, where no group V elements were detected. However, the SEM image also revealed an "overcoat" on the Au catalyst. EDX point measurements of the overcoat revealed the presence of Ga and P but no Au. It is therefore apparent that P_2 (and some residual As_2), that are present during cool down after growth, reacted with the Au-Ga alloy to form a Ga-P compound overcoat. It is believed this could, at least partially, explain the origin of the P signal near Au in TEM.

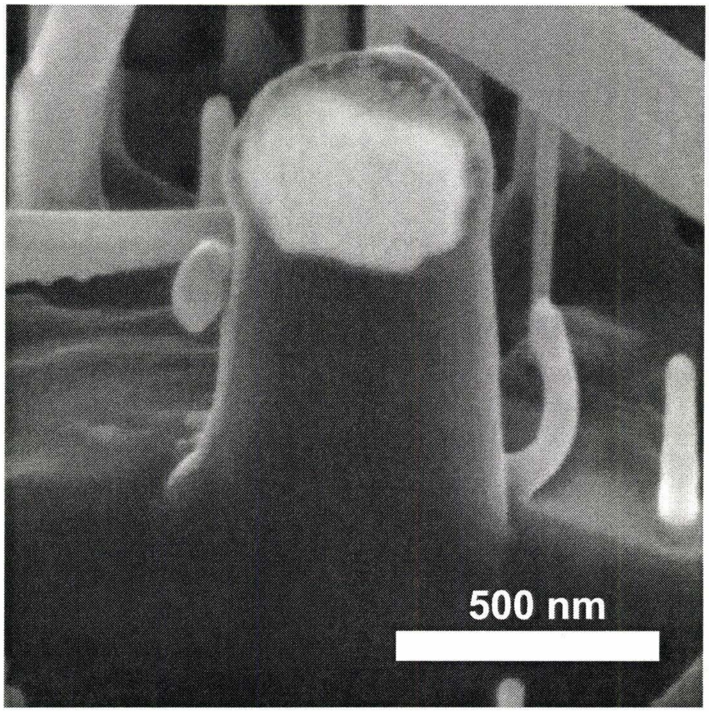

Figure 5.8: Tilted view SEM image of a cross-sectioned NW, showing an overcoat covering the Au surface.

5.1.3 Discussion

In some of our previous work (e.g. Chapter 3), GaAs NWs grew exclusively along the [1 1 1]B direction, orthogonal to the substrate surface, which is the energetically favorable orientation for GaAs NWs due to the (1 1 1)B surface having the lowest free energy. However, in the present study, it appeared that the substitution of As with P for the GaP–GaAsP segmented NWs resulted in some instability in the [1 1 1]B growth direction, as illustrated by the variable growth directions in Figure 5.1. These differences cannot be attributed to the Au catalyst preparation method, as discussed elsewhere [148], since the Au catalysts in this study were prepared in a manner identical to that used in our prior work to grow exclusively [1 1 1]B oriented GaAs NWs (Section 3.1). Instead, the instability in NW growth direction could partially be due to an insufficient supply of group V species, as was observed for the case of GaAs (sample F, Section 4.2) and InAs (Section 4.3) NWs. Additionally, the influence of elastic strain energy introduced by the lattice mismatch among GaP, GaAsP and GaAs could also play a role. For example, GaAs NWs have been observed to grow along the [1 1 0] direction due to the strain energy induced by proximity effects of neighboring NWs [149]. For similar reasons, compressively strained InAs NWs on GaAs substrates have been observed to grow along the [1 0 0] direction [150]. In the present study, it appears that the elastic strain energy induced by the GaP–GaAs substrate interface, or by the GaP–GaAsP heterointerfaces, had a similar influence on the NW growth direction. This is most evident in Figure 5.2 where EDX composition mapping revealed that kinks in NWs coincided with the GaAsP-GaP heterointerface.

We now turn our attention to the two different types of morphology observed in our NWs: pencil- and rod-shaped. Previously, we explained these different morphologies observed in GaAs NWs in terms of the growth mechanisms. It is well known that the dominant mechanism for NW growth consists of diffusion of adatoms from the base and the side of the NW, along its sidewalls, and then into the Au particle at the top of the NW (see Section 3.1). On this basis, we explained the different NW morphologies in terms of the adatom diffusion lengths in comparison to the length of NWs, which resulted in competition between metal-assisted axial growth at the tip of the NW, versus non-metal-assisted radial growth on the NW sidewalls. As was further emphasized in Chapter 4, a tapered pencil morphology occurred at low growth temperatures or high V/III flux ratios where the lower diffusivity of the group III adatoms on the substrate and sidewalls resulted in radial growth of the NWs. Conversely, at higher temperatures and intermediate V/III flux ratios, adatoms optimally diffused to the top of NWs, resulting predominantly in axial growth and rod-shaped NWs. This latter work highlighted the importance of the V/III flux ratio in determining the growth rate and morphology of NWs.

Unlike the GaAs NW growths just described, the GaAsP-GaP NWs in the present study exhibited both pencil and rod-shaped morphology under fixed conditions (temperature and V/III flux ratio) in a single growth. This instability is believed to arise from the competing effects of As and P at the top of NWs. The diffusive transport of adatoms to the Au – NW interface is known to be dependent upon the diameter and separation of NWs [113, 151]. Therefore, the different adatom diffusion lengths for As_2 and P_2 [152], coupled with the broad size distribution and spacing of Au particles, is expected to introduce a variability in V/III flux ratio, As/P ratio, and growth rate at the top of NWs. It is not surprising that the morphology of NWs would be influenced under such conditions. To further elucidate the VLS growth mechanisms, future studies require a systematic variation in Au particle size and separation as performed previously for growth of InAs NWs by CBE [151].

It was apparent from Figures 5.5 and 5.6 that rod-shaped NWs consistently yielded abrupt GaAsP-GaP interfaces. On the other hand, pencil-shaped NWs yielded tapered core-shell heterostructures that matched the morphology at the tip of the NW. From this observation, it was concluded that the NW morphology evolved slowly in the last stages of growth. Furthermore, it was noted that for the pencil NWs, only the top part of the NW that is close to the Au particle was tapered. The lower part below the tapering appeared to be very uniform in diameter. Figure 5.3 also revealed a series of steps (indicated by arrows) and terraces along the tapered region. Finally, it was observed that tapered pencil NWs typically resulted from the smallest Au particles (diameter < 30 nm), while larger Au particles resulted in rod-shaped NWs.

Using the latter observations, a feasible model for growth of the NWs is now elaborated. It is well known that the axial growth rate of a NW is inversely proportional to the Au particle diameter (Section 3.1). We suggest that NWs seeded by relatively large Au particles (> 30 nm in the present case) grow slowly in comparison to the smaller ones (see Figure 3.2) and maintain a length throughout growth that is shorter than the adatom diffusion length. Under these conditions, adatoms may optimally diffuse to the top of the NW and catalytic axial growth is dominant in comparison to radial growth, resulting in rod-shaped NWs (see Figure 5.9a). On the other hand, pencil-shaped NWs, produced from our smallest Au particles (< 30 nm in the present case), grow relatively fast such that their length exceeds the adatom diffusion length in the early stages of growth (Figure 5.9b and c). Subsequently, the probability to nucleate islands at the sidewalls is increased at the expense of metal-assisted axial growth, resulting in significant radial growth (Figure 5.9c). Equivalently, if the adatom diffusivity is kinetically limited (e.g., by lowering temperature or increasing V/III flux ratio), then the probability to nucleate islands on the sidewalls is also increased.

The fact that only the top portion of the pencil NWs were tapered, while the bottom part had uniform diameter, suggests that the radial sidewall growth occurs in a layer-by-layer fashion similar to that for conventional 2D film growth [153]; i.e., island nucleation continues until the sticking of adatoms to the atomic steps of the islands dominates over the creation of new islands (Figure 5.9d). The stable islands then grow by absorbing adatoms at atomic steps along their perimeter, resulting in the completion of a monolayer and return of the sidewall to an atomically flat surface as observed in this work (Figure 5.9e).

The observation of surface steps and ledges in the tapered region of the NW suggest that, once significant radial growth has been initiated, a transition takes place from an island-dominated growth mode in the sidewall region to a step-flow-dominated growth mode in the tapered region. The role of surface steps has been well

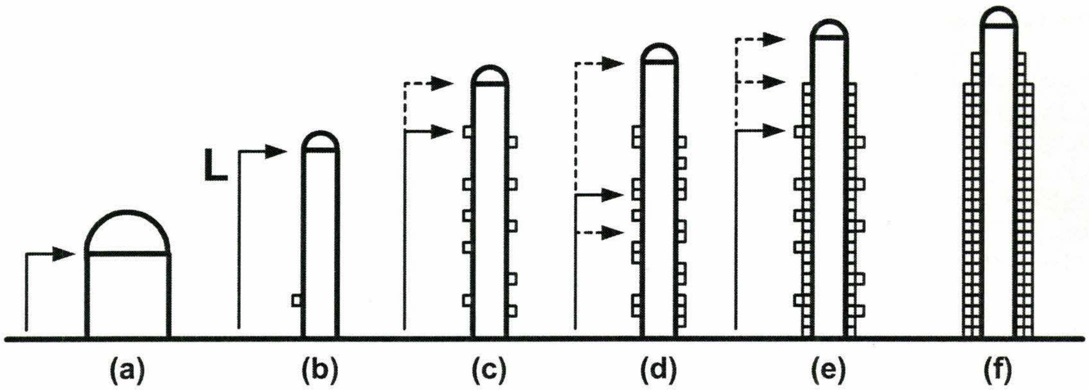

Figure 5.9: Two-dimensional representation of NW growth model. (a) NW produced by large diameter catalyst. (b) NW produced by small diameter catalyst for same growth time as depicted in (a). The NW height is approaching the adatom diffusion length, L. (c) With continued growth, the NW length exceeds L and nucleation on sidewalls (solid arrow) is more probable than catalytic growth (dashed arrow). (d) As nuclei density increases, incorporation at island edges (solid arrow) becomes more probable than the formation of new nuclei (bottom dashed arrow) or catalytic growth (top dashed arrow). (e) Upon completion of a monolayer, the nucleation process depicted in (c) begins anew (solid arrow), while step-flow growth (bottom dashed arrow) and catalytic growth (top dashed arrow) proceed slowly. A tapered geometry is formed with subsequent sidewall deposition, step-flow growth, and slow catalytic growth.

known for decades in the context of film growth on vicinal surfaces [116]. In a like manner to vicinal film growth, adatoms diffusing along the $\{\bar{1}\ 1\ 0\}$ or $\{\bar{2}\ 1\ 1\}$ planes of the NW sidewalls that reach the tapered region will preferentially incorporate at the step edges (Figure 5.9e). Consequently, non-VLS growth occurs as each step edge advances, so that the tapered morphology changes only slowly with time as observed in this study. The possible existence of an Ehrlich-Schwoebel barrier at the step ledges is likely an important consideration in understanding the evolution of the tapered geometry. Adatoms reflected from existing steps due to the barrier would lead to the preservation of existing steps, and to the possible creation of new steps [154]. This will be further considered in the elaboration of a quantitative growth model presented in Chapter 6.

Finally, we turn our attention to the stacking faults observed in Figure 5.6. TEM observations of our NWs revealed that the GaAsP segment contained a large density of stacking faults, while the GaP segment showed very few or no stacking faults. The origin of the stacking faults has been previously attributed to an alternation between zincblende and wurtzite crystal structures due to a rotational twin [144, 148]. It is interesting to note that in the case of GaAs/GaP growth by MOVPE, a trend opposite to ours has been observed [155]; that is, GaP exhibited a large stacking fault density while GaAs showed none. Hiruma and co-workers [115] showed in their early work on GaAs NWs grown by MOVPE that either the zincblende or wurtzite crystal structure could be favored, depending on growth conditions. Previous studies of II-VI nanocrystals grown by colloidal methods [156] showed that the polytypism of zincblende and wurtzite was related to the level of supersaturation, with low levels of supersaturation favoring zincblende and high levels favoring wurtzite. It has been suggested that crystal structure changes during VLS may ensue from structural transformations in the Au particle due to quasi-periodic changes in supersaturation [157].

Although the mechanism of forming zincblende or wurtzite structures has not yet been completely clarified, the changes in stacking fault density observed in our NWs may be driven by a change in group V supersaturation of the Au particle that results from the gas switching at the GaAsP/GaP heterointerface. Furthermore, unlike the case of MOVPE, the comparatively low V/III flux ratio operative during GS-MBE means that the supersaturation of our smallest diameter NWs (< 30 nm) may be influenced by the Gibbs-Thompson effect [57].

5.2 InAs/GaAs Heterostructures

The study of group III heterointerfaces (i.e., a system exhibiting a change in group III composition along the NW axis) was initiated using the InAs/GaAs system. Note that it was done simultaneously to the first two InAs samples that were attempted, and that were described in Section 4.3. Chronologically preceding the systematic study on growth conditions performed on GaAs NWs (Section 4.2) that clarified some growth mechanisms, the results presented here are therefore not optimum. They are included within the framework of this thesis for information purposes only, as they still provide the basis for interesting analysis. The knowledge acquired since then, coupled to what has been published on this specific material system by other groups, allows us to speculate on possible avenues to explore in future work.

5.2.1 Experimental Details

Following the same surface preparation, Au deposition, degas, and annealing procedure as outlined in Section 4.3.1 for the InAs NWs, GaAs NWs were first grown on the GaAs (1 1 1)B substrate at 460°C for 20 minutes (nominal 2D growth rate of 0.28 nm/s, V/III flux ratio ~1.5). Keeping the temperature and AsH_3 flow constant, the shutter was then applied in front of the Ga effusion cell, and the In shutter removed to initiate the InAs growth for 10 minutes. The In atom flux was set to be the same as Ga, which translates to a nominal 2D growth rate of $\sim$0.33 nm/s for this material. Post-growth characterization of this sample (Growth #385) was carried out using SEM (JEOL JSM-7000F), as well as TEM (JEOL JEM-2010F) in bright field, scanning, and HAADF modes.

5.2.2 Results and Discussion

Figure 5.10 shows the typical morphology of the specimen after the growth. A large variety of structures are visible, with the majority of them perpendicular to the substrate surface. Irregular morphologies are however noticed, including some kinking (e.g. feature A in Figure 5.10), a non-negligible occurrence of "bridging", i.e., crystal joining two (or, in some instances, more than two) perpendicular standing NWs (e.g. feature B in Figure 5.10), and thin "antenna-like" structures on top of wider bases (e.g. feature C in Figure 5.10). Unlike the other growths discussed in this thesis, the presence of a hemispherical particle at the tip of the wires (e.g., as can be seen in Figures 3.1, 4.8, and 4.4) is not obvious in all the structures, particularly the ones with the largest diameters. This will be further discussed below, in light of the TEM results.

Some of the morphologies listed above were further investigated by TEM, in order to get information on the crystal structure and chemical composition. The HAADF image in Figure 5.11a illustrates the case of two NWs, one of them with an antenna (which is terminated by a Au particle), "fused" together with a short bridge. A closer examination of some of the areas, coupled to elemental mapping of short segments (labeled directly on Figure 5.11a), allowed us to clarify some aspects of the growth.

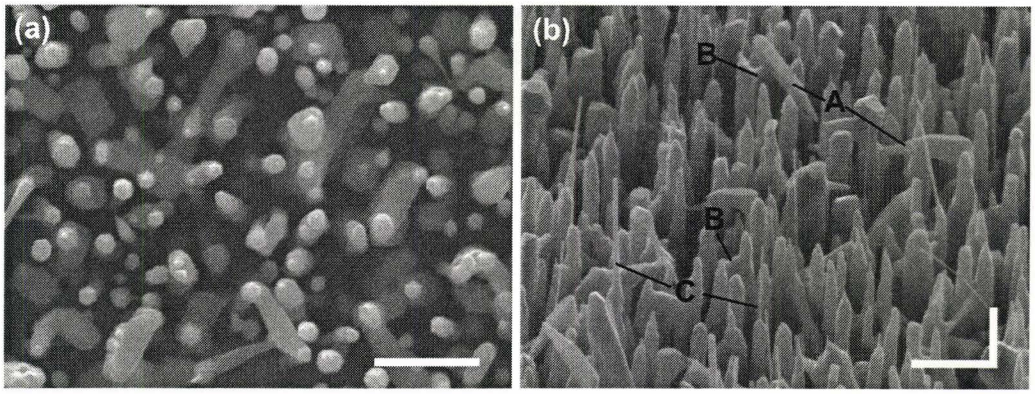

Figure 5.10: (a) Top, and (b) 45° tilted SEM views of the InAs/GaAs NWs. The different labels in (b) refer to the morphologies discussed in the text. Length bars represent 500 nm.

In Figure 5.11b the lower part of the wires (section I) is shown, with the EDX linescan confirming that it consists solely of GaAs. Performing a similar measurement slightly higher in the structure, where the image is brighter and some striped contrast begin to be visible (Figure 5.11c), the two wires are now clearly revealed from the shape of the Ga line (red), and the presence of In mostly in-between the wires suggests the "bridge" consists of InAs. This is even more clear higher up in the structures, where the GaAs NWs become narrower due to tapering (as should be expected under the current growth conditions, see Section 4.2). This scenario (section III) is shown in Figure 5.11d, where a wider InAs bridge can be distinguished between the two wires, which now each consists of a GaAs core and an InAs shell. Notice the bridge does not display any of the striped contrast, which will be discussed later in this section, that is visible on the wires. The nature of the antenna was also investigated (section IV), and as the EDX linescan in Figure 5.11e shows it consists of a pure InAs crystal. It is interesting to note that it was typically defect free, with the wurtzite crystal structure, as was observed on multiple NWs of that type (not shown here). In contrast, the second NW terminates abruptly, without any antenna, and no trace

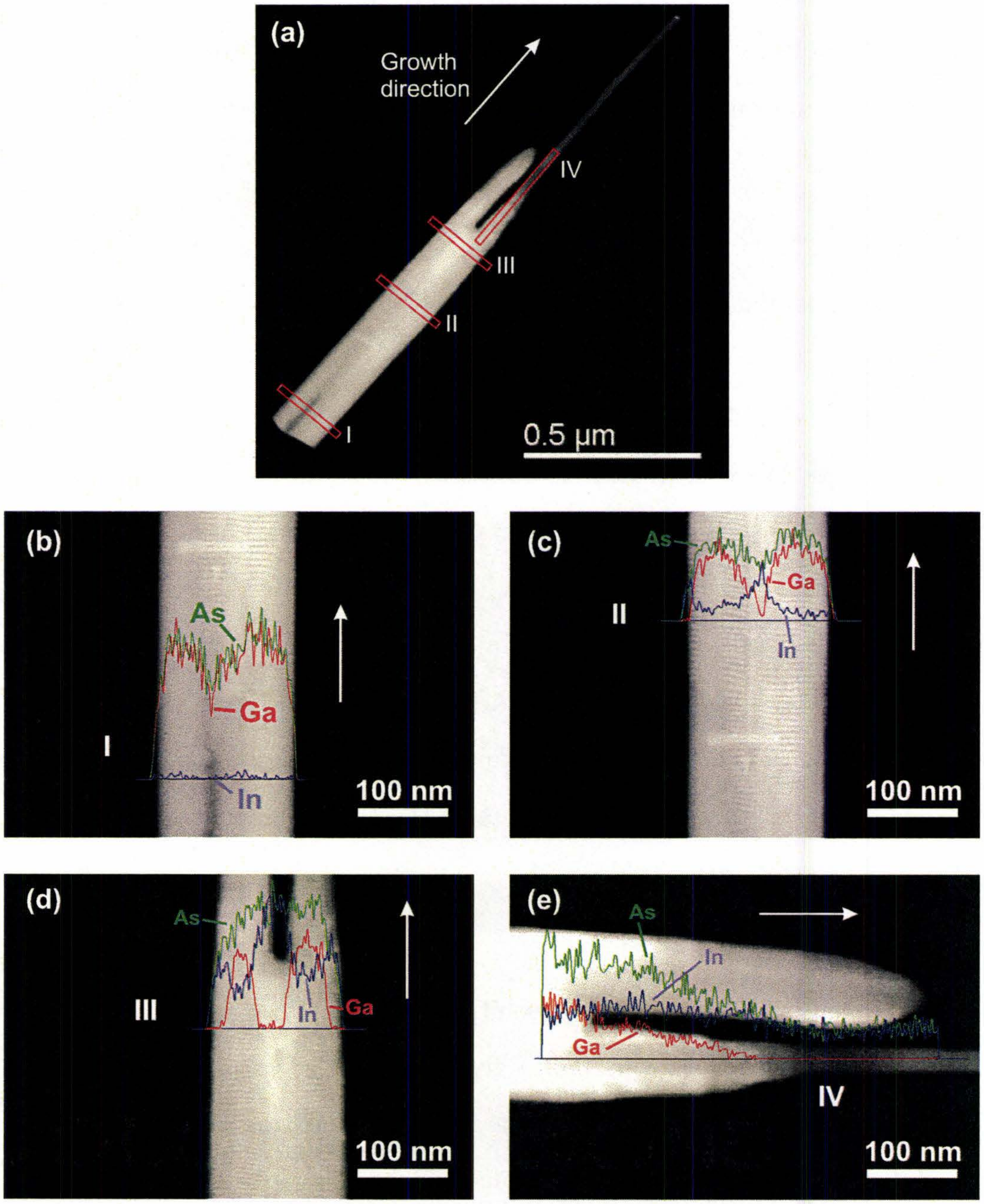

Figure 5.11: (a) HAADF TEM image of two InAs/GaAs NWs illustrating bridging and the growth of an antenna. (b) – (e) EDX linescans for sections I – IV identified in (a). Red: Ga; Purple:In; Green: As.

of Au could be detected in the tip vicinity. This could be the result of a thin antenna that was there initially, and broke off from its base during sonication, or, alternatively, the particle could have been buried due to unfavorable axial growth of the InAs NW segment under the current conditions (as was described in Section 4.3).

The tip area from a single NW of this latter type ("particle-free") is shown under bright field condition (and $\langle \bar{2}\ 1\ 1\ 0 \rangle$ zone axis) in Figure 5.12b. While no clear sign of a break is visible, the presence of a particle could not be established either, even using HAADF or EDX spectrometry. The GaAs core of the structure can however be clearly identified from the Moiré interference pattern in the centre of the structure, which results from the difference in lattice parameter between the core (GaAs, $a = 0.565$ nm at 300 K) and the shell (InAs, $a = 0.606$ nm at 300 K). Some strain contrast in the InAs shell surrounding the core can also be seen. Such features were reported in the literature for the same material system by Paladugu and co-workers [158]. Similarly, the striped contrast observed in the HAADF images of Figure 5.11 is most likely of the same nature (i.e., strain). A more detailed characterization, involving strain mapping from HR-TEM images via the use of the Strain Determination [159] and/or GPA [160] software tools, could therefore be in order to supplement this preliminary analysis.

As can be seen from the high resolution image in Figure 5.12c, the dominant crystal structure is wurtzite ($(0\ 0\ 0\ \bar{1})$ growth direction), with zincblende stacking faults. Interestingly, the very tip of the wire (emphasized on the image with the arrow) clearly reveals the ABCABC atom arrangement of the zincblende structure. Since the few antennas that were observed were wurtzite, it is thus reasonable to think that this zincblende segment formed at the very end of the growth, analogous to the cooling neck previously discussed (see Section 4.2), and that no antenna NW growth occurred at all. In this case though, this final zincblende segment could not be

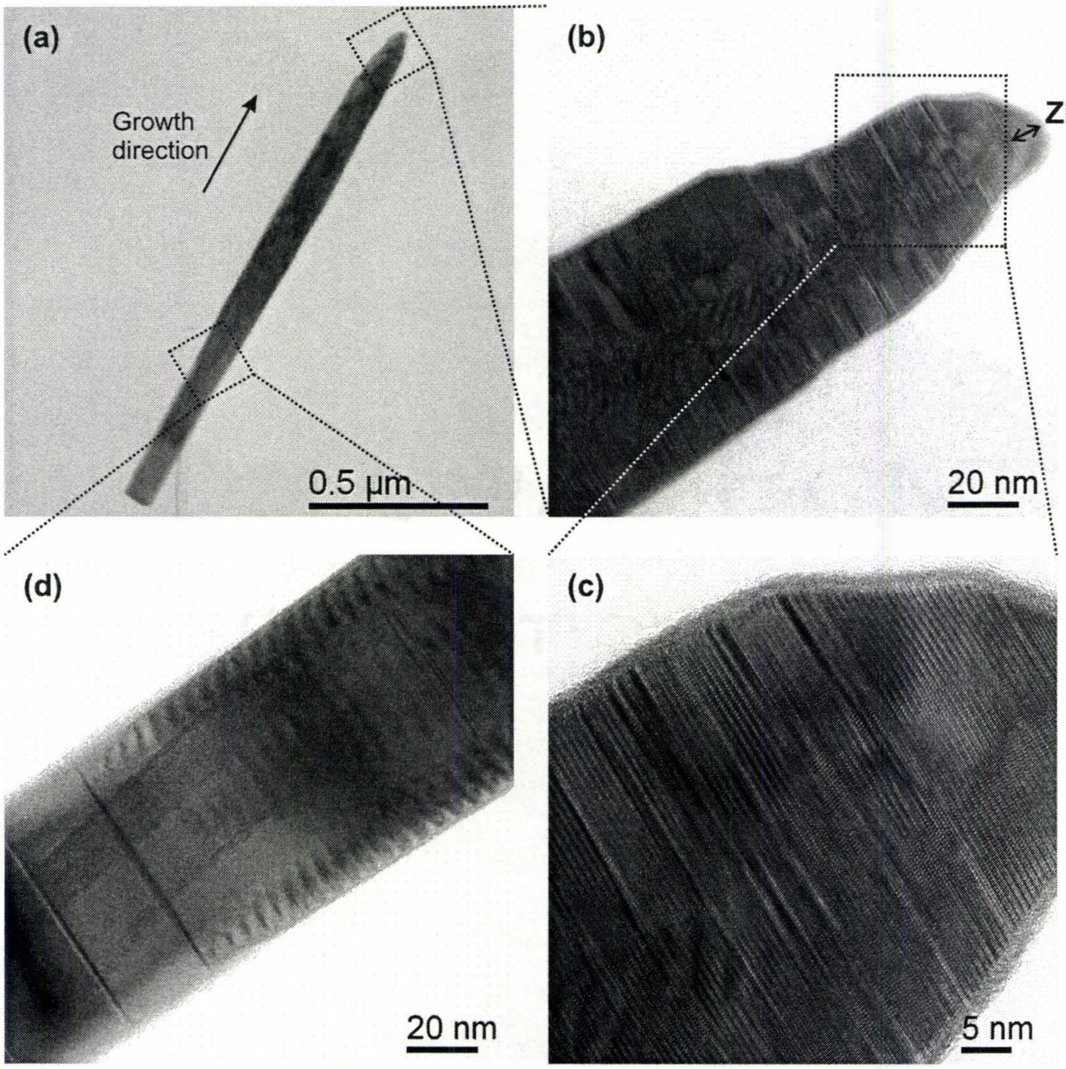

Figure 5.12: (a) Bright field TEM image of a "particle-free" InAs/GaAs NW. (b) A closer look at the tip, where the GaAs core can be identified from the Moiré fringes in the centre of the structure. (c) HR-TEM images in the tip vicinity, highlighting the zincblende nature of the upper part. (d) Bright field and TEM image taken where the InAs shell stops.

the result of the particle purging, and further study may be necessary to clarify the nature of this occurrence. Reduced supersaturation conditions are however probably at its origin. Particle burial when InAs growth was initiated (and GaAs terminated) appears more plausible (albeit un-verified at this point) in this scenario, due to growth conditions yielding a low effective V/III flux ratio at the particle – NW interface, thus inhibiting the Au-assisted axial growth (see Section 4.3 on InAs growth).

Looking now at what happens lower in the structure, the focus is placed on the area where the InAs coating stops. Figure 5.12d is a bright field TEM image illustrating the transition from the coated upper part (striped contrast) to the bare GaAs base. EDX mapping (not shown here) confirmed the chemical composition of each portion of the segment. Acknowledging from a previous study (Section 4.2) that GaAs NWs grown under the current conditions would exhibit strong tapering with $\langle\bar{2}\ 1\ 1\ 0\rangle$ facets in the lower part (i.e., one side of the hexagonal NW is perpendicular to the zone axis), then the "teeth pattern" exhibited by the InAs shell in this area is most likely linked to the wetting of this material on the NW core facets. The schematic in Figure 5.13 describes this proposed situation from three points of view. It thus appears that In adatoms coming from the upper part of the NW do not reach the base, resulting only in partial covering of the GaAs core.

In light of the preliminary analysis presented above, and using some of the knowledge acquired on the individual GaAs (Chapter 3 and Section 4.2) and InAs (Section 4.3) material systems, the following generic sequence of events is proposed to describe the dominant InAs/GaAs structures obtained under the current conditions:

(i) Following the initial GaAs growth, the surface of the specimen is similar to the one shown in Figure 4.1c. After 20 minutes growth, the high density of NWs most definitely yield shadowing effects between NWs.

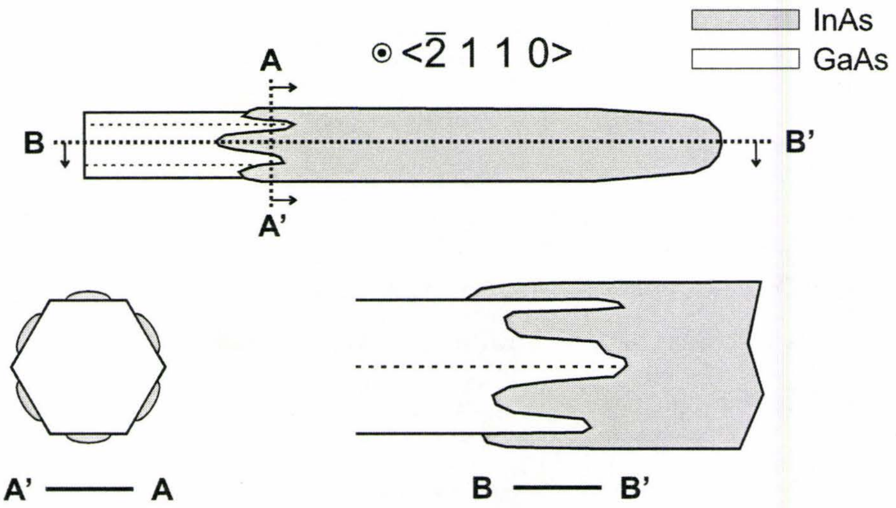

Figure 5.13: Schematic illustrating the transition between the coated and not-coated area of a InAs/GaAs NW from three different views: top view, cross-sectional cut, and side view. The "teeth pattern" observed experimentally would therefore be a result of partial wetting of the InAs coating on the hexagonal facets of the GaAs core.

(ii) InAs growth is then initiated, but the current combination of temperature (460°C), nominal V/III flux ratio (~1.5), and nominal 2D growth rate (~0.33 nm/s) most likely results in an effective V/III flux ratio at the particle – NW interface lower than unity, thus inhibiting axial growth via the VLS mechanism (see Section 4.3 for the growth of InAs NWs under similar conditions).

(iii) Instead, InAs growth takes place on the sidewalls of the NWs, thus coating the latter, and probably burying the seed particle. The stacking faults that are present in the GaAs core are propagated throughout the InAs shell, suggesting that the atoms of the shell mimic the arrangement of the sidewall surface (the substrate), i.e., the shell grows in an epitaxial manner.

(iv) Because of shadowing, the lower part of the GaAs NWs is not exposed to the In flux. In addition, the strong GaAs NW tapering expected from the growth conditions, resulting in steps on the NW surface, most likely limit the diffusion toward the base of the In adatoms that landed on the upper part of the NW. Therefore, only partial coating is achieved, thus leaving the base as bare GaAs.

In some instances, metal-assisted growth of the InAs segment can occur in parallel to the coating process described above, resulting in a defect-free antenna. In those situations, it is believed that the local morphology limited the diffusion of group III adatoms, yielding an effective V/III flux ratio at the particle – NW interface. While further characterization would be necessary to definitely conclude on the nature of the kinked structures, some indications on the possible mechanisms operating could be found from the evolution of InAs branches during the MOVPE growth of InAs on GaAs NWs described by Paladugu and co-workers [158]. Following the model proposed by these authors, an antenna growing downward as a result of an unbalance of the seed particle with the underlying GaAs NW [161] would be affected by the radial growth of InAs on the GaAs core (the downward movement would be terminated), and axial growth in a (1 1 1)B direction (or $(0\ 0\ 0\ \bar{1})$ in the present wurtzite scenario) would be initiated.

Clearly, the initial goal of fabricating axial InAs/GaAs heterostructures was not achieved, while the core-shell structure geometry would require refinement in the process to at least achieve uniform coating of the core. For future attempts at the growth of this material system, it would therefore be first recommended to follow a procedure in which each segment is grown under its optimum condition. Therefore, in line with the results presented in Section 4.2, the initial GaAs NWs should be grown at a fairly high temperature (~600°C), moderate V/III flux ratio (~2.3), and nominal 2D growth rate of 0.14 nm/s. Such conditions will significantly reduce the NW density, and therefore, in addition to an improved morphology and crystal integrity, limit the shadowing effects. With the shutter applied in front of both the Ga and In effusion cells, the temperature should be lowered to ~400°C under the As_2 overpressure. Then the In shutter could be removed, with a flux similar to the Ga. As pointed out in Section 4.3, more work would be required to optimize the nominal flux ratio, but we know from these preliminary results that a value greater than 2.0 should be established if an axial heterostructure is desired. In the case where a core-shell structure is targeted, it is suggested to adopt a strategy with a low nominal V/III flux ratio (e.g. 1.5 or lower), which will inhibit the axial VLS growth, and simply coat the GaAs cores. A better understanding and control of the particle instability that could trigger downward growth [161] may be necessary for the elaboration of a successful procedure.

5.3 Chapter Summary

The results obtained when studying the GaP/GaAsP NWs are of fundamental importance for understanding the growth conditions that are necessary to achieve abrupt, defect-free heterostructures in semiconductor NWs grown by gas source molecular beam epitaxy. We have proposed that sidewall growth of NWs occurs in a layer-by-layer fashion, as the result of an adatom diffusion length that is limited in comparison to the NW length. Once radial growth is initiated, a tapered geometry is formed that is maintained by a step-flow growth mode. As a result, core-shell heterostructures are formed that mirror the NW pencil geometry. Under conditions that promote longer diffusion lengths in comparison to the NW length (higher temperatures, lower V/III flux ratios, large Au catalysts), adatoms may optimally diffuse to the top of the NW forming a rod-shaped NW morphology. Under these conditions, planar and abrupt interfaces are formed. EDX composition measurements of the Au particle, and the faceted structure of the Au, suggested that the Au-Ga alloy was liquid at the growth temperature. This confirmed that the NWs grew by a vapor-liquid-solid process. Supersaturation conditions of the Au drop appeared to influence the crystal structure of the NWs, with GaP having fewer stacking fault defects compared to GaAsP. Consistent with the results presented in Chapter 4, our work indicated that single-crystal NWs, free of stacking faults, might be obtained in GS-MBE under appropriate supersaturation conditions.

Preliminary results on the InAs/GaAs material system were discussed to conclude this chapter. The desired axial heterostructure that was initially targeted resulted instead in GaAs NWs with a partial InAs cladding. Metal-assisted axial growth of the InAs segment was most likely inhibited by the growth conditions that induced a low effective V/III flux ratio at the particle – NW interface. Various resulting morphologies were shown and discussed, and a possible growth sequence was proposed. A strategy toward the successful fabrication of such heterostructures in the future was presented, involving a two-temperature and two-V/III flux ratio procedure.

Chapter 6

Analytical Growth Model

6.1 Introduction

Much effort has been devoted to the modeling of the axial growth of NWs. Pioneering work by Givargizov [17, 18], which described the growth of micron-size Si whiskers by CVD, revealed that thicker whiskers grew faster compared to thin whiskers. This behavior resulted from the low supersaturation conditions, whereby the Gibbs-Thomson effect associated with the finite curvature of the whisker surface, dominated in this regime [57]. Under the higher supersaturation taking place during growth by MOVPE [57,141], CBE [151], and MBE [53,54], the Gibbs-Thomson effect becomes negligible, and typically thin NWs grow faster than thicker ones. Consequently, the $H_w \propto 1/D$ behavior experimentally observed (with H_w and D being the NW height and diameter, respectively, as defined in previous chapters) indicates the diffusion-induced nature of the growth [12,53,56,57]. Recent work by Dubrovskii and co-workers suggested that a $1/D^2$ dependence would apply under certain growth conditions [129]. On the other hand, very little has been reported thus far to describe the radial growth of NWs. A model for the latter, based on the vapor-solid (VS) process (while the NW continues to grow axially via the VLS mechanism), was first proposed by Chen and co-workers [162]. The equation obtained for the radial growth rate suggests the existence of a critical NW radius above which the structure will thicken. More recently, the problem of sidewall nucleation was addressed by Dubrovskii and co-workers [163], where the authors developed a relationship for the NW diameter as a function of the distance from the substrate surface and the total NW height, which applies for conically-shaped NWs that can be obtained under lower growth temperatures. The development does not, however, address abrupt radius changes, such as the "pencil-shaped" structures often observed experimentally [54, 77, 80], and described in Chapters 3, 4, and 5 of this thesis.

In this chapter we present a simple model describing in an analytical manner the metal-assisted growth of NWs. The model constitutes an extension of the qualitative description that was put forward in Section 5.1.3, based on a step-flow mediated growth mechanism. For this purpose, we elaborate on a model that was initiated by Tchernycheva and co-workers [77]. Like these authors, an isolated NW is considered, thus neglecting the effects of neighbouring NWs, such as competition for adatoms and shadowing. Note that most of the text presented here has been taken from a journal article that was submitted for publication to the Journal of Applied Physics [83]. Additional steps in the derivation of the equations were included, and the figures were adapted to the format of the thesis.

6.2 Model

We aim to describe the evolution of the NW morphology over time, as observed in previous (Section 3.2) and recent (to be discussed in Section 6.3) experimental results on various III-V materials systems. Notably, the abrupt radius change yielding a pencil-shaped morphology is translated in terms of the initiation of radial growth, with a progression in a layer-by-layer fashion. We already suggested in Section 5.1.3 this mechanism to operate based on the observation of steps on the NW sidewall surfaces. Complementing this latter qualitative description, a set of equations is elaborated based on material conservation. The axial progression of the radial shell, consistent with our previous proposal, is included in the present model via a step-mediated growth. Similar to the treatment proposed by Tchernycheva et al. [77], the growth duration is divided into two main regimes. The NW initially grows in a purely axial manner (Regime A). Once a certain critical height is reached, nucleation is initiated on the sidewalls while the NW continues growing axially (Regime B).

Within the framework of this development, the NW will be approximated as a rod, and the shape of the Au seed particle will be treated as a perfect hemisphere. The geometry of an actual growth system such as MBE is also considered, with the incident atom flux making an angle α with the substrate surface normal.

6.2.1 Pure Axial Growth (Regime A)

Figure 6.1 illustrates the various parameters of the model in Regime A, where the NW growth occurs only along its axis without any radial growth, provided it is shorter than a critical height H_c achieved at a growth duration t_c (Figure 6.1c). A flux, J (# atoms/nm^2/s), of group III atoms (equivalent to a nominal 2D growth rate of V nm/s) is impinging directly on the Au seed particle, on the sidewalls of the NW, and on the substrate surface. It thus contributes to either the axial growth of the NW, or the growth of the 2D film on the areas of the substrate not activated by a metal particle. In this regime, the NW maintains a constant radius R_o throughout its entire length, which is identical to the particle radius. A circular area of radius $R_o + r_o$ surrounding the NW represents the collection area of adatoms, as shown in Figure 6.1b. Atoms impinging in this area can reach the Au-NW interface by diffusion and contribute to axial growth. The goal is thus to elaborate an expression for the height of the NW as measured from the surface of the 2D layer, i.e., $H_w(t)$.

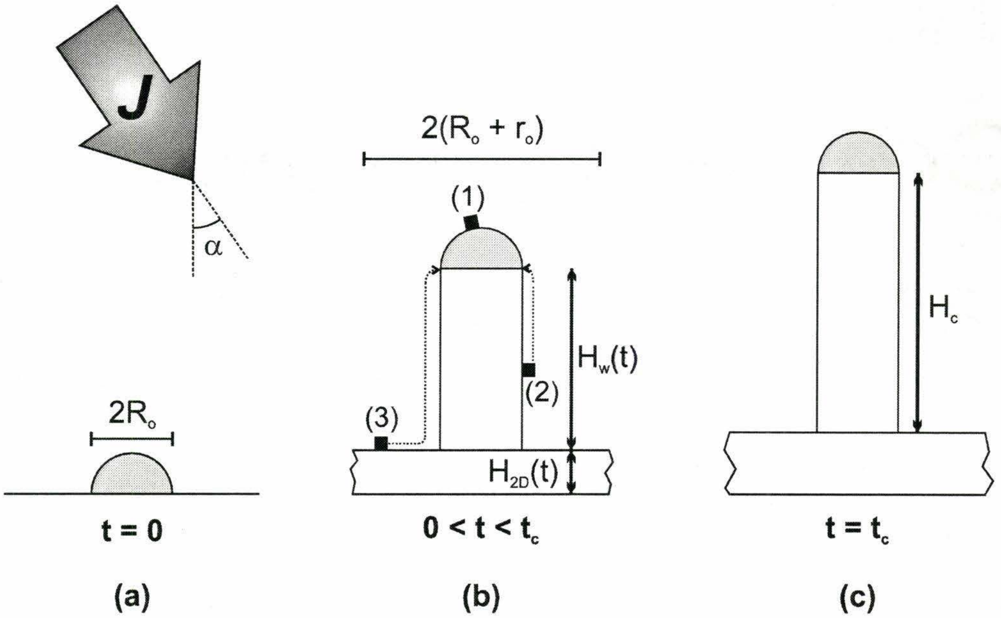

Figure 6.1: Schematic illustrating the various parameters used in developing the model in Regime A, i.e., pure axial growth. The dark squares represent adatoms that impinge directly on the various surfaces: (1) on the seed particle; (2) on the sidewall surface; (3) on the substrate surface. The dotted line arrows represent the path of the adatoms for incorporation at the axial growth interface.

Under the above considerations, the variation of the NW total volume per unit time is simply given by:

$$\frac{d(\mathrm{Vol})}{dt} = \pi R_o^2 \left(\frac{dH_T}{dt} \right) = \pi R_o^2 \left(\frac{d\left[H_w(t) + H_{2D}(t)\right]}{dt} \right), \tag{6.1}$$

where H_T is the total NW height, H_w is the NW height above the 2D film, and H_{2D} is the 2D film thickness. This growth is sustained by three main sources of incoming material as described below.

6.2.1.1 Direct Impingement on the Surface of the Seed Particle

We consider a steady-state scenario where the supersaturation of the particle is reached and maintained, so the precipitation rate is constant. A fraction χ_A of the atoms adsorbed on the Au particle (adatom (1) in Figure 6.1b) will contribute to the axial growth of the NW. No difference is made at this point whether the adatoms will diffuse *on* or *through* the particle to reach the growth interface, since the end result is identical regardless of the path followed (i.e., there is a direct contribution to the axial growth of the NW). An incident group III flux, J, on the Au particle of radius R_o at an angle α thus corresponds to $\pi R_o^2 J \cos\alpha$ atoms per second impinging on the particle. To obtain the volume variation, the latter expression is simply divided by the group III atom density in the crystal ρ. Since $J/\rho = V$ (i.e., the nominal 2D growth rate), the contribution to the NW volume variation is given by:

$$\frac{d(\mathrm{Vol})_1}{dt} = \chi_A \pi R_o^2 V \cos\alpha. \tag{6.2}$$

6.2.1.2 Direct Impingement on the Sidewalls

Of all the atoms impinging directly on the NW sidewall surfaces, it is assumed that only a fraction ξ_A will adsorb, migrate in the direction of the seed particle, and finally be incorporated in the growing NW crystal (adatom (2) in Figure 6.1b). As no radial growth occurs in this regime, all adatoms either contribute to axial growth, diffuse toward the base to contribute to the growth of the 2D layer, or simply desorb. Although the substrate is rotated during growth to ensure a more uniform flux distribution on the surface, the flux "sees" a rectangle of height $H_w(t)\sin\alpha$ and width $2R_o$. The number of atoms per unit time contributing to the axial growth is simply $2\xi_A J R_o H_w(t)\sin\alpha$, which translates to a volume variation rate of:

$$\frac{d(\mathrm{Vol})_2}{dt} = 2\xi_A V R_o H_w(t)\sin\alpha. \tag{6.3}$$

6.2.1.3 Impingement on the Substrate Surface

It is assumed that only a fraction φ_A of the atoms adsorbed within a circular ring of thickness r_o surrounding the NW will migrate toward the wire, diffuse along the NW sidewalls to reach the particle, and contribute to the axial growth (adatom (3) in Figure 6.1b). The remaining fraction of adatoms, $1-\varphi_A$, contributes to 2D film growth or desorb. The projection of the collection area along the flux direction is given by $\pi\left[(R_o+r_o)^2 - R_o^2\right]\cos\alpha$, thus giving a change in NW volume per unit time of:

$$\frac{d(\mathrm{Vol})_3}{dt} = \varphi_A \pi V\left[(R_o+r_o)^2 - R_o^2\right]\cos\alpha. \tag{6.4}$$

Combining the above three contributions (Equations 6.2, 6.3, and 6.4) with Equation 6.1 to obtain the balance equation results in the following differential equation:

$$\frac{dH_w(t)}{dt} - \frac{2\xi_A V \sin\alpha}{\pi R_o} H_w(t) = \left[\frac{\varphi_A \left[(R_o + r_o)^2 - R_o^2\right]}{R_o^2} + \chi_A\right] V \cos\alpha - \frac{dH_{2D}(t)}{dt}. \tag{6.5}$$

Within the framework of this analysis, where any irregularity of the surface morphology of the 2D film is neglected, it is reasonable to assume that the growth rate of the non-activated surface is constant, and is a fraction of the nominal growth rate, i.e., $dH_{2D}(t)/dt = \eta V$. Equation 6.5 then becomes a simple linear differential equation with the boundary condition $H_w(0) = 0$. It is solved by adding the homogeneous and particular solutions.

(i) Homogeneous Solution

The characteristic equation $(\lambda - (2\xi_A V \sin\alpha / \pi R_o) = 0)$ yields the following homogenous solution:

$$H_{wh}(t) = K_1 \exp\left[\frac{2\xi_A V \sin\alpha}{\pi R_o} t\right], \tag{6.6}$$

where K_1 is a constant.

(ii) Particular Solution

Given the nature of the term on the right-hand side of Equation (6.5), we set the particular solution as $H_{wp}(t) = K_2 = const.$, so its derivative $dH_{wp}(t)/dt = 0$. Replacing these in Equation (6.5):

$$\frac{-2\xi_A V \sin\alpha}{\pi R_o} K_2 = V \left\{\left[\frac{\varphi_A \left[(R_o + r_o)^2 - R_o^2\right]}{R_o^2} + \chi_A\right] \cos\alpha - \eta\right\}$$

thus yields

$$H_{wp}(t) = \frac{-\pi R_o}{2\xi_A \sin\alpha}\left\{\left[\frac{\varphi_A\left[(R_o + r_o)^2 - R_o^2\right]}{R_o^2} + \chi_A\right]\cos\alpha - \eta\right\}. \tag{6.7}$$

Adding (6.6) to (6.7), and applying the boundary condition to determine the constant K_1, an analytical expression is obtained for $H_w(t)$ in Regime A:

$$\begin{aligned} H_w(t) = \frac{\pi R_o}{2\xi_A \sin\alpha}&\left\{\left[\frac{\varphi_A\left[(R_o + r_o)^2 - R_o^2\right]}{R_o^2} + \chi_A\right]\cos\alpha - \eta\right\} \\ &\times\left\{\exp\left(\frac{2\xi_A V \sin\alpha}{\pi R_o}t\right) - 1\right\}. \end{aligned} \tag{6.8}$$

6.2.2 Radial and Axial Growths (Regime B)

When the NW reaches a height H_c (Figure 6.1c), which is obtained by setting $t = t_c$ in Equation 6.8, species impinging on the 2D film and subsequently migrating toward the NW can no longer reach the Au–NW interface ($\varphi_A = 0$) to contribute to axial growth. Instead, the adatoms nucleate on the NW sidewalls and contribute to radial growth. Only adatoms within a diffusion length of the Au–NW interface can contribute to axial growth; i.e., adatoms directly impinging on the Au seed particle or on the sidewalls near the top of the NW. We previously speculated the radial growth to operate in a step-flow mode around the core of the NW (Section 5.1.3. Therefore, the height of the radial shell, $h_s(t)$ (Figure 6.2), will be treated in terms of step-mediated growth as originally proposed by Burton et al. [7] in their theory of thin film crystal growth. The diagram in Figure 6.2 illustrates the possible paths for an adatom that has impinged in the upper part of the NW (segment $L(t)$). Once formed, the short segment $L(t)$ is maintained by the step and the Au particle acting as strong

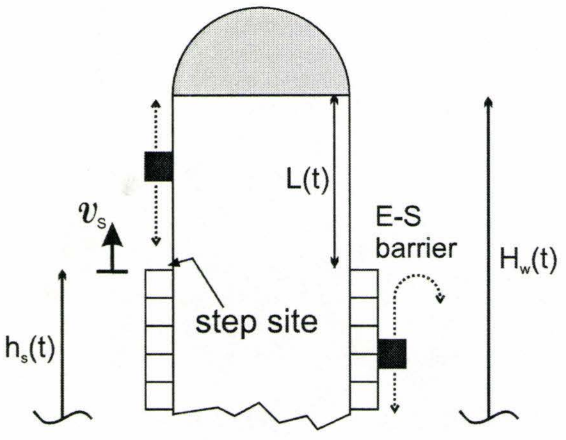

Figure 6.2: Evolution of the shell height $h_s(t)$ as a result of step-mediated growth. Adatoms from the upper layers do not contribute, and are reflected at the step edge (E-S barrier).

sinks for adatom incorporation. Therefore, the adatoms contribute either to the axial growth of the nanowire, or the axial growth of the shell by attaching to the step, with less probability of nucleation on the sidewall of the segment $L(t)$. Equivalently, the step velocity, v_s, does not deviate significantly from the axial growth rate $dH_w(t)/dt$, as will be seen in Section 6.3. As in Regime A, we assume the top of the NW and the Au particle will maintain the same radius R_o. As a first approximation, it is assumed that adatoms moving toward the step from upper layers will be reflected, as shown in Figure 6.2, due to an Ehrlich-Schwoebel (E-S) barrier [164–166].

The rate at which the height of the shell $h_s(t)$ progresses is thus equal to the velocity of the step due to adatom attachment, i.e., $dh_s(t)/dt = v_s$. This constant velocity is the result of atoms impinging on the surface at a constant rate, and attaching to a single step, as derived by Tu and co-workers [167]. Assuming that the first shell monolayer that formed around the NW at $t \approx t_c$ has an initial height h_{si}, a simple expression for $h_s(t)$ is obtained:

$$h_s(t) = v_s\,(t - t_c) + h_{si}, \tag{6.9}$$

6.2.2.1 NW Axial Growth $H_w(t)$

In Regime B the same three mechanisms described above for Regime A still prevail as described by the parameters χ_A, ξ_A, and φ_A. Due to the presence of steps, it must be recognized that the analogous parameters for Regime B may be modified and are therefore described by the parameters χ_B, ξ_B, and φ_B. Notably, since in this regime the NW height exceeds the diffusion length for the adatoms coming from the substrate surface, φ_B now refers to the fraction of adatom that contribute to the NW radial growth, and not the NW axial growth as was the case in Regime A.

Beyond $t = t_c$ the NW starts growing radially, while axial growth is sustained by the direct impingement on the seed particle ($\chi_B \pi R_o^2 V \cos\alpha$) and the diffusion of the adatoms from the upper segment $L(t)$ to the particle ($2\xi_B R_o L(t) V \sin\alpha$). In the latter case, the fraction of the adatoms reaching the particle (ξ_B) will be affected by the growing shell due to step sites which constitutes a sink for the adatoms. Similar to Regime A, the variation of the NW volume with time $\pi R_o^2\,(dH_T/dt)$ may be derived with the assumption of the same constant growth rate of the 2D layer dH_{2D}/dt, so:

$$\begin{aligned}\frac{dH_w(t)}{dt} - \frac{2\xi_B V \sin\alpha}{\pi R_o} H_w(t) = {}& \frac{-2\xi_B v_s V \sin\alpha}{\pi R_o} t \\ & + V\left[\chi_B \cos\alpha - \frac{2\xi_B\,(h_{si} - v_s t_c)\sin\alpha}{\pi R_o} - \eta\right],\end{aligned} \tag{6.10}$$

with the boundary condition $H_w(t_c) = H_c$ (see Figure 6.1c). Using the same approach to solve Equation 6.10 as was used for Regime A (i.e., adding the homogeneous and particular solutions), the final expression for $H_w(t)$ for $t > t_c$ is therefore given by

$$H_w(t) = (H_c - v_s t_c - \kappa)\exp\left[\frac{2\xi_B V\sin\alpha}{\pi R_o}(t - t_c)\right] + v_s t + \kappa, \tag{6.11}$$

where

$$\kappa = \frac{\pi R_o}{2\xi_B \sin\alpha}\left[v_s\left(\frac{1}{V} - \frac{2\xi_B t_c \sin\alpha}{\pi R_o}\right) - \chi_B\cos\alpha + \frac{2\xi_B h_{si}\sin\alpha}{\pi R_o} + \eta\right].$$

Both an exponential and a linear time dependence for the NW height appear in Regime B, whereas only the exponential behavior resulted from the derivation for Regime A (Equation 6.8). It is interesting to note that Sears, in the mid-1950's, had already made some predictions for the growth of whiskers [8]. An exponential trend was then obtained in the early stage of the growth (analogous to our Regime A), but an essentially linear dependence was established when the whisker exceeded a certain length/height (condition analogous to our Regime B), due to adatoms desorbing before reaching the tip via diffusion. As will be further discussed in Section 6.3, the mechanism proposed here, with two exponential regimes, is more representative of the trend observed in the VLS growth of NWs.

6.2.2.2 Radial Growth, $R(t)$

Having determined how the height of the shell that forms around the NW core varies with time (Equation 6.9), the description of the morphology is now completed by elaborating a relationship for the evolution of its radius $R(t)$. For that purpose, the approach of material conservation is used in the same manner as above. It is assumed that the shell forms a hollow cylinder of inner radius R_o, outer radius $R(t)$, and height $h_s(t)$, which means that the layers subsequently depositing on the first monolayer reach the same height as the latter. The taper experimentally observed in the vicinity of the shell edge is therefore neglected in this first approximation. Moreover, all atoms adsorbed on the shell surface contribute to the radial growth, meaning that desorption is neglected. The volume variation of the NW associated with the segment where the shell develops is simply given by

$$\frac{d(\mathrm{Vol})}{dt} = \pi \frac{d\left\{\left[R^2(t) - R_o^2\right] h_s(t)\right\}}{dt} = 2\pi R(t) h_s(t) \frac{dR(t)}{dt} + \pi \left[R^2(t) - R_o^2\right] \frac{dh_s(t)}{dt}. \tag{6.12}$$

Direct impingement on the shell surface amounts to a volume variation rate of the shell equal to $2R(t)h_s(t)V \sin\alpha$. As previously postulated, an E-S barrier prevents atoms from attaching at the lower level, or migrating to the particle to take part in the axial growth of the NW. Similar to the mechanism considered for the axial growth described in both Regime A and Regime B, a fraction φ_B of the atoms adsorbed in the collection area will migrate toward the NW and will contribute to the shell volume (through an increase of its thickness) by $\varphi_B \pi V \left[(R(t) + r_o)^2 - R^2(t)\right] \cos\alpha$. Note that this latter contribution was neglected by Tchernycheva et al. [77] on the basis of a very short (25 nm) diffusion length of the adatoms on the surface of the 2D layer. This latter value was determined by fitting of experimental data to a model developed by Dubrovskii and co-workers [168]. In the present analysis, the contribution will be maintained for the sake of completeness. The following non-linear differential equation thus governs the radial growth:

$$\frac{dR(t)}{dt} + \frac{v_s\left[R^2(t) - R_o^2\right] - \varphi_B V r_o^2 \cos\alpha}{2R(t)\left[v_s\left(t - t_c\right) + h_{si}\right]} = V\left[\frac{\sin\alpha}{\pi} + \frac{\varphi_B r_o \cos\alpha}{\left[v_s\left(t - t_c\right) + h_{si}\right]}\right], \tag{6.13}$$

which is valid for $t \geq t_c$, with the boundary condition $R(t_c) = R_o$. The solution to Equation 6.13 is obtained via a standard adaptive Runge-Kutta-Fehlberg algorithm [169].

6.3 Comparison with Experiment

To assess the above model, its numerical behavior is compared to actual measurements obtained from a series of growths done on two material systems, GaAs and InAs. While the experimental details concerning the former are presented below, the results for the latter were directly extracted from Reference [77], where the fabrication procedure can also be found.

6.3.1 Fabrication and Characterization Details for GaAs NWs

Surfaces of n-type (111)B-oriented GaAs substrates were prepared as per the procedure described in Section 3.2.1, and a 1 nm (as measured by a quartz crystal monitor) layer of Au was deposited at room temperature in an electron-beam evaporator. Each substrate was then transported, in ambient air, to a gas source MBE (GS-MBE) system, where they were first degassed at a temperature of 300°C for 15 minutes. A subsequent 10-minute anneal at 550°C in the growth chamber was performed under an As_2 overpressure and a hydrogen plasma to activate the nanoparticle formation, and desorb any native oxide that could have formed in a previous step. The temperature and As_2 flux were then set to the desired values, and the NW growth was initiated by opening the Ga effusion cell shutter.

All the specimens were grown at a substrate temperature of 600°C, a V/III flux ratio of $\sim$2.3 and a Ga atom flux yielding a nominal 2D growth rate of 0.28 nm/s (as determined from previous growth calibrations done on GaAs (1 0 0) surfaces). These conditions were maintained for durations of 180 (Growth #519), 600 (Growth #521), 1200 (Growth #633), 1800 (Growth #508), and 3600 (Growth #520) seconds in five separate growths, after which the substrates were cooled under the As_2 flux, and slowly brought back to ambient conditions (except for the 1200-second sample, which was quenched, and the As_2 flux terminated simultaneously with the Ga flux, for the purpose of experiments described in Section 4.2).

Post-growth characterization was primarily done using a JEOL JSM-7000F field emission scanning electron microscope (FE-SEM) operated in the secondary electron mode, with accelerating voltages of 3 and 4 kV. For the 3600-second sample, most of the analysis was done with a Philips CM12 conventional transmission electron microscope (CTEM) operated at 120 kV for bright-field imaging. The various dimensions (shell height, NW height and diameter) were measured directly on the micrographs.

6.3.2 Results and Discussion

6.3.2.1 GaAs

SEM images in Figure 6.3 show the evolution in morphology of GaAs NWs for growth durations between 180 and 3600 seconds. Up to 1200 seconds (Figures 6.3a to c), the NWs maintained a uniform diameter over their entire length. For growth durations exceeding 1200 seconds, a "pencil shape" due to radial growth could be distinguished for a variety of wires (as shown in Figures 6.3d and e). This latter morphology continues to evolve, and after 3600 seconds the NWs were not only longer, but their diameter also increased due to the radial growth. It thus appears that the transition from Regime A to Regime B occurs sometime between 1200 and 1800 seconds of growth (i.e., $1200 < t_c < 1800$).

Focusing first on Regime A, the data points in Figure 6.4a show the NW height evolution (i.e., H_w as a function of the growth duration) for the case $D_o = 2R_o = (40 \pm 4)$ nm, while the ones in Figure 6.4b show the NW height versus its diameter (for $t = 1200$ s), as measured directly on the SEM images. For the purpose of comparison

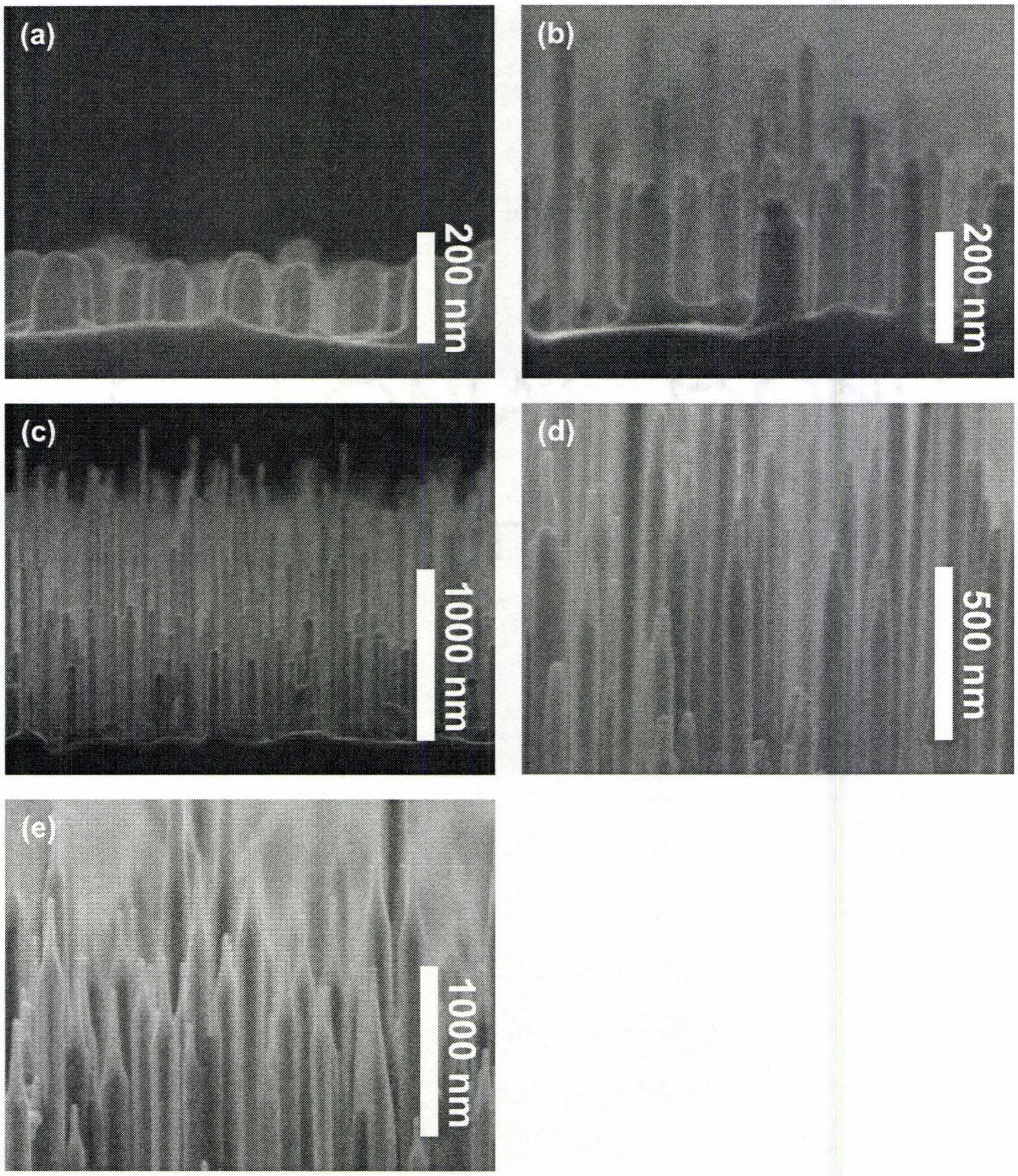

Figure 6.3: Cross-sectional SEM micrographs illustrating the morphology and size of GaAs NWs after (a) 180, (b) 600, (c) 1200, (d) 1800, and (e) 3600 seconds of growth. The growth temperature was 600°C, the V/III flux ratio ~2.3, and the nominal 2D growth rate 0.28 nm/s.

with Equation 6.8, various parameters need to be established. The physical design of the MBE system provides us with a value for the impingement angle, α, of 35°, while the growth rate, V, was set by the incident Ga flux (0.28 nm/s). The size of the collection area r_o surrounding the NW was fixed to 25 nm, a value based on the work done by Dubrovskii and co-workers [168]. For η (i.e., the fraction of incident flux contributing to the growth of the 2D film), estimation from film thickness measurements by cross-sectional TEM, coupled to calculations based on NW density and average NW height, yielded a value of 0.8, which is consistent with the value of 0.77 obtained by Dubrovskii and co-workers [168].

Under normal MBE growth conditions such as the ones that prevailed in the present experiment, desorption of impinging group III atoms is usually assumed to be negligible. This was verified in work by Dubrovskii et al. [168], whereby a numerical model was fit to experimental data, resulting in an estimated desorption rate of the Ga atoms from the Au droplet that was only 12% of the deposition rate under similar MBE growth conditions as employed in our study. Tchernycheva et al. [77] also assumed in their model of InAs nanowires that In desorption was negligible. Similar to these authors, and in the same manner as was first modeled by Wagner and Ellis [16], the Au particle is treated as an essentially perfect sink for impinging adatoms. Therefore, all adatoms impinging on the Au surface will directly contribute to the axial growth of the NW; i.e., $\chi_A = 1$. Furthermore, we expect $\xi_A > \varphi_A$ (i.e., the fraction of adatoms impinging on the NW sidewalls that contribute to axial growth will be greater than the corresponding fraction impinging on the 2D surface between NWs) due to the closer proximity of the sidewalls to the Au particle, as well as to the presence of strongly adsorbing kink sites at the intersection of the NW with the 2D film. Finally, values must be chosen that will not only reasonably fit the data in Regime A, but also ensure a realistic transition to Regime B (i.e., the

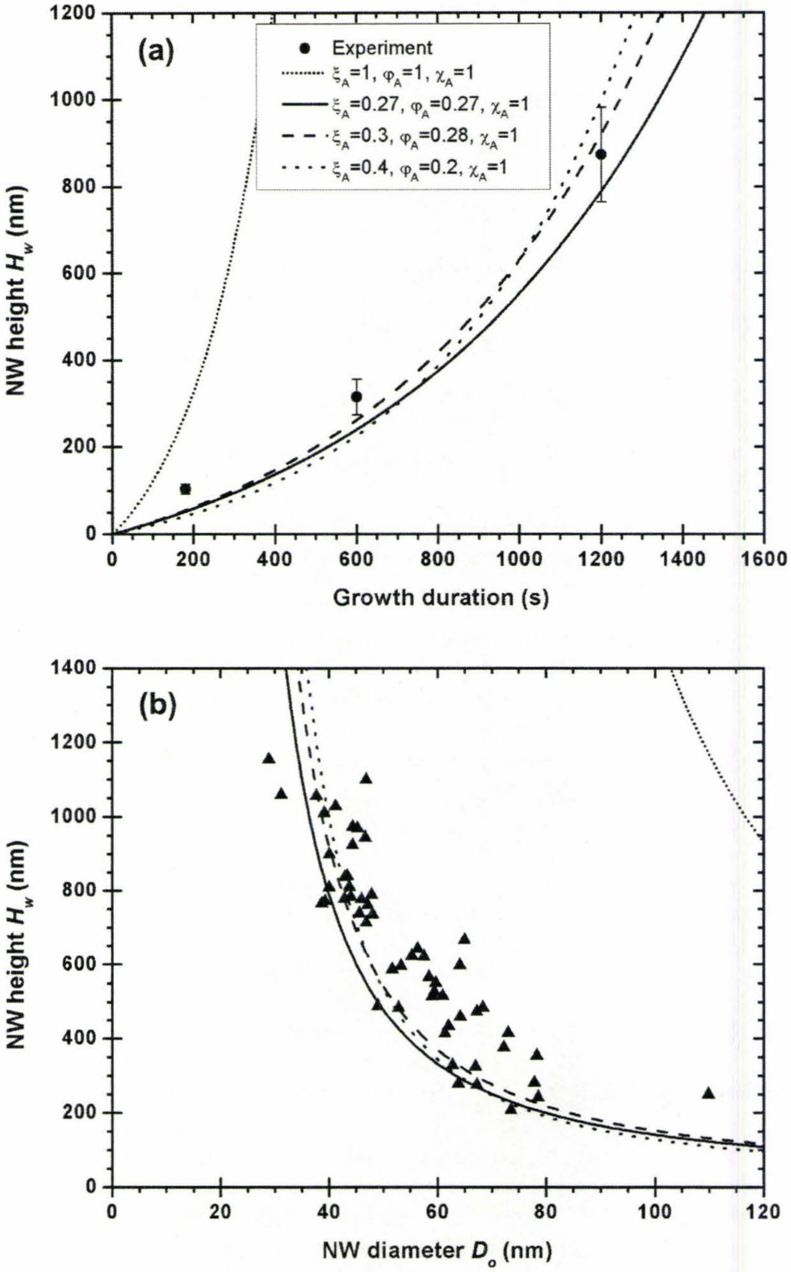

Figure 6.4: Evolution of the GaAs NW height H_w as a function of: (a) the growth duration (for the case $D_o = 2R_o = 40$ nm), and (b) the NW diameter D_o in Regime A for $\chi_A = 1$ and various values of ξ_A and φ_A. The data points in (a) are experimental measurements for NWs having a diameter $D_o = (40 \pm 4)$ nm, with the error bars corresponding to one standard deviation. Each point in (b) corresponds to a single NW measurement.

exponential behavior in Regime A is not too strong such that H_w near t_c does not exceed measurements made in Regime B).

With the above provisions, the remaining parameters, ξ_A and φ_A, may be systematically varied for comparison with the data in Figures 6.4a and b. The scenario where all values are set to unity, $\chi_A = \xi_A = \varphi_A = 1$ (short dotted curves in Figure 6.4), is first discussed, which corresponds to the case where all adatoms contribute to the axial growth of the NW. This is equivalent to the model initially proposed by Tchernycheva and co-workers [77]. As can be seen, this significantly overestimates the actual growth rate. While this was already acknowledged in Reference [77], it constitutes an argument in favor of the present model. The other curves shown in Figure 6.4 illustrate the sensitivity of the two parameters ξ_A and φ_A. Reasonable and physically meaningful fits to the experimental data were obtained with ξ_A between ~0.27 and ~0.4 (φ_A between ~0.2 and ~0.3), with best fit values of $\xi_A = 0.3$ and $\varphi_A = 0.28$. Note that this choice of parameters is able to fit simultaneously the data of Figure 6.4a and b.

Moving to Regime B, Figures 6.5a and b show the NW height and diameter, respectively, versus the growth duration, which includes the subset of data from Figure 6.4 for Regime A. The solid line in Figure 6.5a is the model fit to Regime A using $\xi_A = 0.3$ and $\varphi_A = 0.28$ as just described. Note that since no radial growth occurs in this regime, a straight line was plotted for the evolution of the NW diameter as a function of the growth duration in Figure 6.5b, i.e., at the average measured value, so $D \approx D_o$. For comparison of the data with Equations 6.11 and 6.13, the identical parameter values as established for Regime A were chosen; i.e., $\alpha = 35^\circ$, $V = 0.28$ nm/s, $r_o = 25$ nm, and $\eta = 0.8$. Note that the composition of the Au particle may change with evolution of the NW height due to changes in supply of adatoms diffusing from the 2-D surface or from the NW sidewalls. However, as was assumed for Regime A, we set $\chi_B = 1$, meaning that all atoms impinging on the Au particle contribute to axial growth. In addition, it will be assumed that $\varphi_B = \varphi_A$, since between the two regimes the only difference with regards to the contribution from the substrate is that in the latter case the adatoms reach the particle (Regime A), while in the former case they do not, contributing solely to radial growth instead (Regime B).

Using direct measurements on the NWs, the step velocity v_s can be estimated by measuring the height of the shell between the growth durations of 1800 and 3600 s. A value of 0.56 nm/s is obtained, and is therefore fixed in Equations 6.11 and 6.13. Note that H_c is not considered a free parameter, as it is determined by replacing the value of t_c in Equation 6.8. Performing additional growths with durations between 1200 and 1800 s would enable a more precise evaluation of t_c, but for the present exercise an intermediate value of 1450 s was chosen (yielding $H_c \approx 1430$ nm). With only two data points available for this regime, and two parameters remaining (h_{si} and ξ_B), no unique values for the latter could be identified. The curves in Figure 6.5a therefore provide the range of possible values to fit the $H_w(t)$ data. For ξ_B values less than ~0.08, the expected increasing exponential behavior (which will be more evident in the following section on InAs NWs) numerically disappeared for any value of h_{si}. The overestimation of the model compared to the measured radial growth, shown in Figure 6.5b, may be explained by the very dense population of NWs on the surface, inducing shadowing effects and/or competition for adatoms between neighboring NWs [77], which is not included in the model. This aspect will be further discussed below.

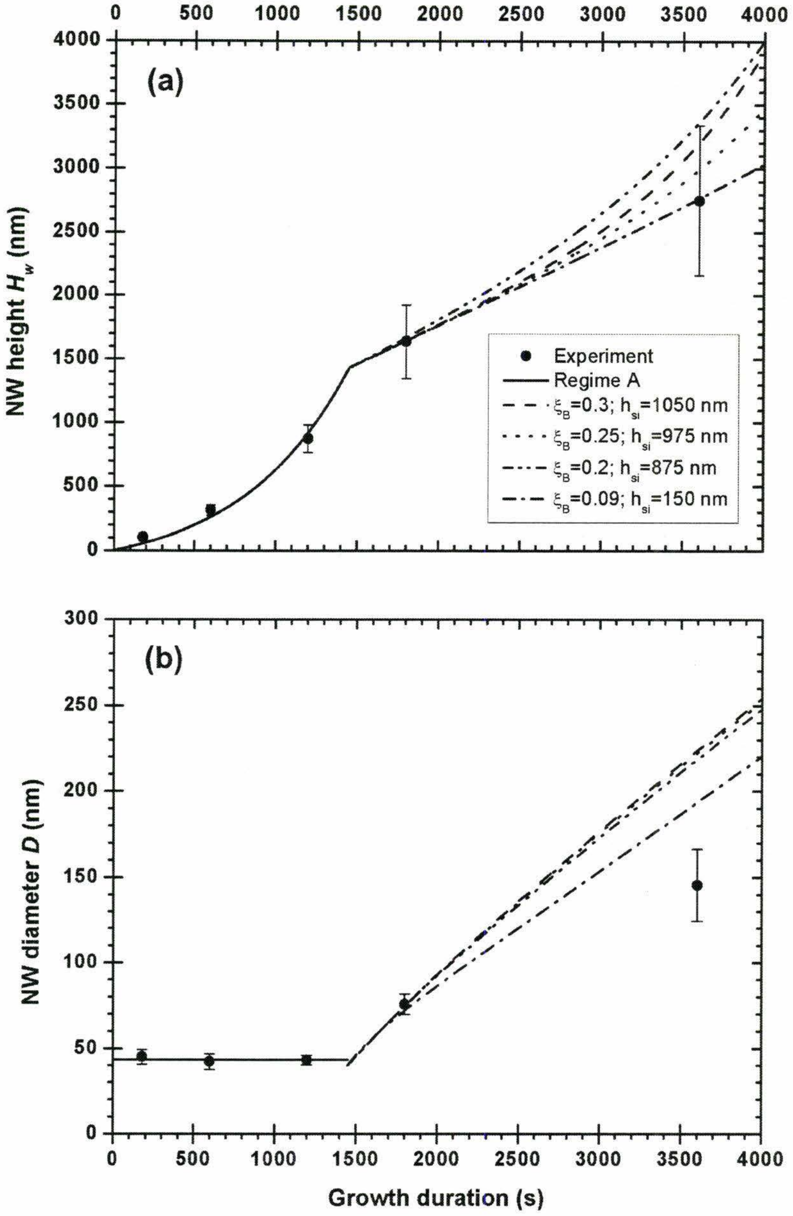

Figure 6.5: Evolution of the GaAs NW height H_w (a) and diameter $D = 2R$ (b), as a function of the growth duration, for NWs with initial diameter $D_o = 2R_o = (40 \pm 4)$ nm. The error bars correspond to one standard deviation. The various curves are fits to the data based on the proposed model. Four sets of parameters were used for Regime B, illustrating the effect of varying ξ_B and h_{si} when t_c is kept constant at 1450 s.

6.3.2.2 InAs

To further assess the model, a similar analysis as the one for GaAs was performed on a series of experimental data obtained by Tchernycheva and co-workers for MBE-grown InAs NWs [77]. The experimental conditions provided by the authors ($D_o =$ 30 nm, $\alpha = 33°$, $V = 0.2$ nm/s) were used as model parameters. Information on 2D growth was not available, so η was assumed to be on the same order of magnitude as our GaAs NWs (i.e., $\eta = 0.8$). χ_A was assumed to be unity as previously discussed. The size of the collection area was set to $r_o = 25$ nm, following Reference [168]. An analysis was performed by varying the two remaining parameters (ξ_A and φ_A). Note that results on H_w vs D_o were not available in this case, so the values were assessed only on the basis of time evolution.

As illustrated in Figure 6.6, the scenario $\xi_A = \varphi_A = \chi_A = 1$ greatly overestimates the measurements, as was also the case for GaAs. A fit to the data could be obtained with ξ_A between ~0.35 and ~0.65 (φ_A between ~0.1 and ~0.33). More experimental information on radial growth rate and initiation time t_c would allow more precise fitting. However, selecting an intermediate value for t_c of 1625 s based on the data of Reference [77], the best fit is obtained with $\xi_A = 0.37$ and $\varphi_A = 0.35$ (solid curve in Figure 6.7a). These higher incorporation factors obtained for the InAs NWs, as compared to the previous case of GaAs, could have their origin in the typical longer diffusion length of In adatoms relative to Ga. Additionally, the experimental conditions could have played a role; for instance, the InAs growths were done at a nominally higher V/III flux ratio of 3 (compared to 2.3 for GaAs) and relatively low temperature (410°C). The greater availability of group V species at the seed particle may thus allow for more group III atoms to contribute to the NW axial growth.

The experimental behavior of the H_w data for $t \geq 1800$ s (Regime B), displayed in Figure 6.7a, indicates a non-linear progression, contrary to some of the initial models

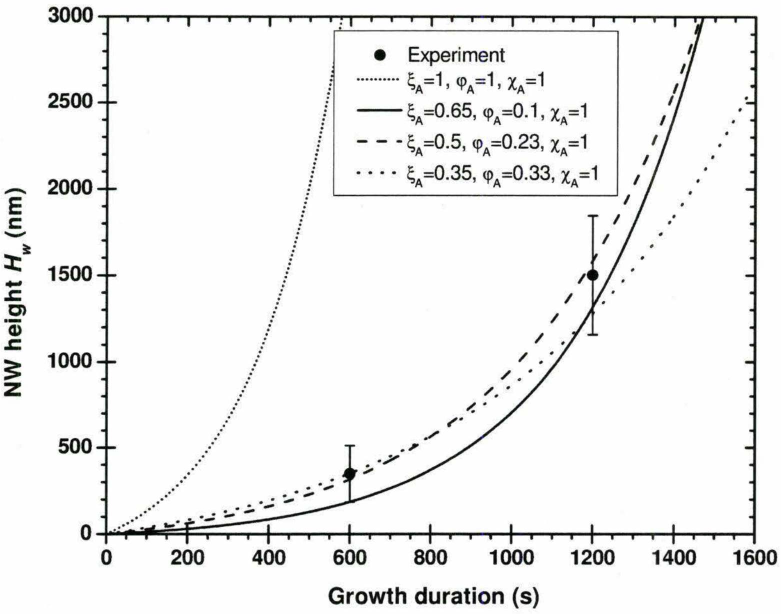

Figure 6.6: Evolution of the InAs NW height H_w as a function of the growth duration (for the case $D_o = 2R_o = 30$ nm), in Regime A for $\chi_A = 1$ and various values of ξ_A and φ_A. The data points are experimental measurements retrieved from Reference [77], with the error bars corresponding to one standard deviation.

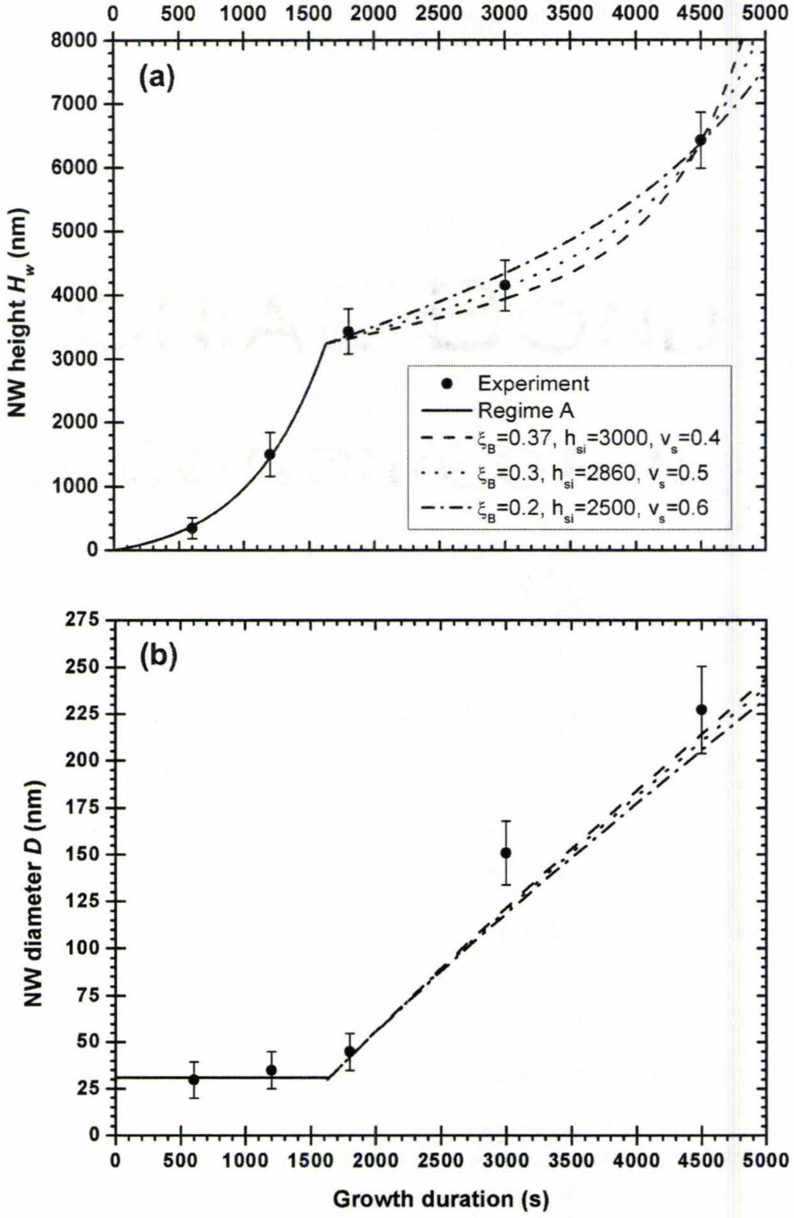

Figure 6.7: Evolution of the InAs NW height H_w (a) and diameter $D = 2R$ (b), as a function of the growth duration, for NWs with initial diameter $D_o = 2R_o \approx 30$ nm. The data points are experimental measurements retrieved from Reference [77], with the error bars corresponding to one standard deviation. The various curves are fits to the data based on the proposed model (h_{si} in nm, v_s in nm/s).

proposed for whisker and NW growth [8, 11, 77]. The shortcomings of these previous approaches are addressed in the present model by accounting for the diffusion of species landing in the upper part of the NW, the time dependence variation of the segment $L(t)$ via the step-mediated growth, and the non-unity probability of adatom contribution to the NW axial growth. Due to the lack of data, notably to quantify the step velocity, unique values for the parameters could not be identified. Figure 6.7a therefore illustrates possible fits for the three sets of values, ξ_B, h_{si} (in nm), and v_s (in nm/s). In all cases t_c was set at 1625 s. Note that an increase in ξ_B is associated with a decrease in the step velocity v_s, thus necessitating a lower initial shell height h_{si}. The effect on the radial growth is shown in Figure 6.7b. In all three cases a reasonable fit was also achieved for $D(t)$, which may be related to the lower NW density on the surface in the case of InAs (between 0.5 and 2.5 $\times 10^8$ cm^{-2}, more than an order of magnitude lower than for the GaAs specimens), thus making the actual situation closer to the "isolated NW" scenario assumed in the development of the model.

6.4 Chapter Summary

In summary, a model describing the axial and radial growth of III-V NWs from metal seed particles was presented. While a diffusion-controlled mechanism was assumed (as suggested by experimental results), no explicit derivation of diffusion equations was required, and instead only simple material balance relations were developed to obtain the time evolution of the NW height and radius. Two distinct regimes were identified and analyzed, differentiated by the amount of adatoms diffusing to the axial growth interface and the triggering of radial growth. In the first regime, the NWs grow exclusively in an axial manner, with the growth sustained by three sources of materials: direct impingement on the seed particle, impingement on the sidewalls followed by diffusion to the particle, and impingement on the substrate surface (in a collection area surrounding the NW) followed by diffusion to the particle. Once the NW height exceeds the adatom diffusion length on the sidewalls, the growth transitions to a second regime in which radial growth is initiated in the lower part of the NW, while axial growth is maintained at a lower rate (as the substrate adatoms no longer contribute). Due to the diffusive nature of adatom transport, not all atoms impinging on the substrate or NW sidewalls were assumed to contribute to the axial growth. Furthermore, due to the complexity of the growth processes, a phenomenological treatment was adopted using model parameters to describe the relative fraction of impinging adatoms that contribute to axial growth. This approach is reminiscent of atom incorporation models to describe epitaxial growth of III-V films [170].

The axial growth of the NW was assumed to depend on the flux of the group III species reaching the growth interface, with group V species supplied in excess, which is the usual case in thin film growth by MBE (see for instance Section 7.6.1 in Reference [171]). However, the model does not exclude the possible group V-limited aspect of NW growth as discussed previously [81] where the model parameters may depend on group V flux.

The general trends established by the model in terms of the time evolution of the axial and radial growths were assessed by comparing them to MBE-grown GaAs and InAs NWs. Although the model has a large number of free parameters and the data set is limited, we hope the phenomenological model presented here will lay the foundations toward a better understanding of the various NW growth mechanisms. In particular, the primary contribution of the model is the inclusion of the step-mediated axial growth of the shell and the fractional contribution of adatoms toward axial growth.

Chapter 7

Conclusion and Future Work

7.1 Thesis Summary

Through a series of growths performed on GaAs (1 1 1)B substrates under various conditions, the mechanisms operating during the metal-assisted growth of vertical III-V NWs by GS-MBE were investigated. Three major aspects could be established, resulting from the careful characterization of the as-grown structures by electron microscopy.

(i) The axial growth is sustained by three sources of materials; i.e., direct impingement of growth species on: the seed particle, the substrate surface (followed by diffusion to the seed particle), and the sidewalls of the growing NW (also followed by diffusion to the seed particle). From the measurement of the NW height H_w as a function of the seed particle diameter D, a clear dominance of the latter two processes is visible for the smallest values of D, characterized by a $H_w \propto 1/D$ behaviour. Beyond a certain critical diameter, a different regime sets in (first experimentally observed by the author) where thicker NWs grow faster. Transition from mononuclear- to polynuclear-mediated growth under the particle, coupled to the Gibbs-Thomson effect being more dominant in this size range, is probably at the origin of this observed trend, as was subsequently modeled by a different group [52].

(ii) When the NW height exceeds the diffusion length of adatoms coming from the substrate surface, and also the ones coming from the lower part of the NW, radial growth is triggered. A characteristic "pencil shape" morphology results from the latter, where the NW remarkably conserves a uniform diameter throughout most of its length, except near the tip, where a taper can often be observed. We postulated that this uniformity was due to the radial growth operating in a layer-by-layer fashion on the sidewalls, similar to the epitaxial growth of a film on the surface of a substrate. An observed evolution of the sidewall facets orientation from $\{\bar{1}\ 1\ 0\ 0\}$ to $\{\bar{2}\ 1\ 1\ 0\}$ is consistent with the previous postulate. Moreover, the presence of steps on the sidewalls in the tapered part suggest that the radially growing shell also progresses axially in a step-flow mode.

(iii) The axial growth and single-crystalline nature of the NWs strongly depend on a larger V/III flux ratio than is typically required for the growth of 2D layers. This suggests that the local flux ratio at the growth interface (under the particle) is effectively lower than the nominal value, possibly due to the significantly lower solubility of group V species in the metal particle. A more regulated supersaturation of the particle provided by an increase in the group V flux, accompanied by a lowered group III flux, resulted in the most regular structures with a minimized defect (stacking fault) occurrence, suggesting that the NW axial growth is group V stabilized. This latter aspect is of primary importance for future device fabrication, as it differs from the usual group III stabilized character of epitaxial layers.

From a practical point of view, generic fabrication guidelines could be established based on a systematic investigation of the effects of growth parameters (temperature, V/III flux ratio, and group III flux) on the morphology and crystal structure. In the case of GaAs, NWs with uniform diameter and minimized stacking fault frequency (and even in some instances complete absence of any stacking fault) were achieved at a temperature of 600°C, a V/III flux ratio of 2.3, and a Ga impingement rate on the surface of 0.07 nm/s. An increase of the flux ratio favored uniform sidewall growth (by limiting the diffusion of group III adatoms), thus making the process suitable for the fabrication of core-shell structures. Another possible strategy to achieve such a structure could be through the lowering of the effective V/III ratio at the axial growth interface (item (iii) above). After growing a core under the conditions just described, the group V flux could be lowered so to yield a nominal V/III flux ratio just above unity (e.g. $\sim$1.1). The NW axial growth thus becomes significantly lowered, if not completely inhibited, while the conditions are still favorable to 2D growth, and consequently also to NW radial growth.

Using all the information acquired from the experimental observations, an analytical description of the growth was finally elaborated, based on a simple material conservation model. Direct impingement of growth species on the particle, coupled to their diffusion from the sidewall and the substrate surface, were considered in the derivation of expressions for the time evolution of both axial and radial growths. Factors that take into account the non-unity probability of inclusion of group III adatoms in the axially growing crystal were introduced, and constitute one of the most original feature of the model. Additionally, a step-mediated growth was included to describe the axial evolution of the shell.

7.2 Future Work

While the purpose of this thesis was to establish the bases toward the controlled fabrication of NWs, more work is undoubtedly necessary toward a full understanding of all aspects of the growth, and, in the longer term, device consistency.

One process we think deserves more in-depth studying is the self-assembly of the seed metal particles on the substrate surface. The brief discussion on this topic that was presented in Section 2.1, while certainly providing a generic description of the mechanisms involved, still leaves some unanswered questions. Moreover, large differences in particle size and density following a similar heat treatment but different NW growth conditions, as reported in Chapter 4, would suggest that annealing be done at the desired growth temperature in order to avoid any additional surface migration between the time annealing is completed and growth is initiated. A more systematic Au-film annealing study, done with the MBE system instead of the RTA furnace in order to reproduce the exact conditions preceding the NW growth, could make the overall process more robust by optimizing the spatial and size distributions of particles. Notably, if the annealing and growth temperature are the same, effects of shadowing from neighbouring NWs could be minimized by establishing the proper initial film thickness and annealing duration. Additionally, the possible incubation time alluded to in Chapter 4 could be clarified. This study should even be extended to other substrates than GaAs (1 1 1)B, such as InP (1 1 1)B.

The generic guidelines for growth conditions, derived using the GaAs NWs, could also be extended to other materials systems. Preliminary results on In-based binary compounds like InAs (Section 4.3 of the present thesis) and InP (Chapter 4 of reference [139]) already provide a basis for further study. A more systematic analysis similar to the one presented in Chapter 4 could be in order to determine optimum conditions adapted for the type of structures, especially to trigger uniform radial growth for core-shell applications. In the longer term, a complete understanding of how the various growth species incorporate in ternary and quaternary alloyed NWs will further expand the range of applications. We believe that this will only be achieved though systematic studies of the various material systems of interest and their substrates.

To complement the electron microscopy characterization, important structural information could be gained with photoluminescence (PL) measurements. While these fell outside the scope of the current work, some preliminary results obtained using the micro-PL set-up at the Institute of Quantum Computing (University of Waterloo) are shown in Figure 7.1, clearly validating the importance of minimizing stacking faults. Extending the study to room temperature performances, and investigating possible ways to passivate the NWs, are all important aspects toward device development. X-ray diffraction (as was performed on CdTe nanorods [172]) could additionally provide a means to measure accurately the lattice parameters.

From a theoretical point of view, the validity of the proposed model was already successfully demonstrated, at least semi-quantitatively. Further refinements, notably with regards to the axial progression of the shell via the step-mediated growth process (e.g. a reduction in the assumed "perfectly reflecting" E-S barrier), would enhance the description of the growth. A more precise assessment of the ξ_x, φ_x, χ_x, and t_c parameters could be established by increasing the number of data points (i.e., do additional growths at different durations, maintaining the same growth conditions).

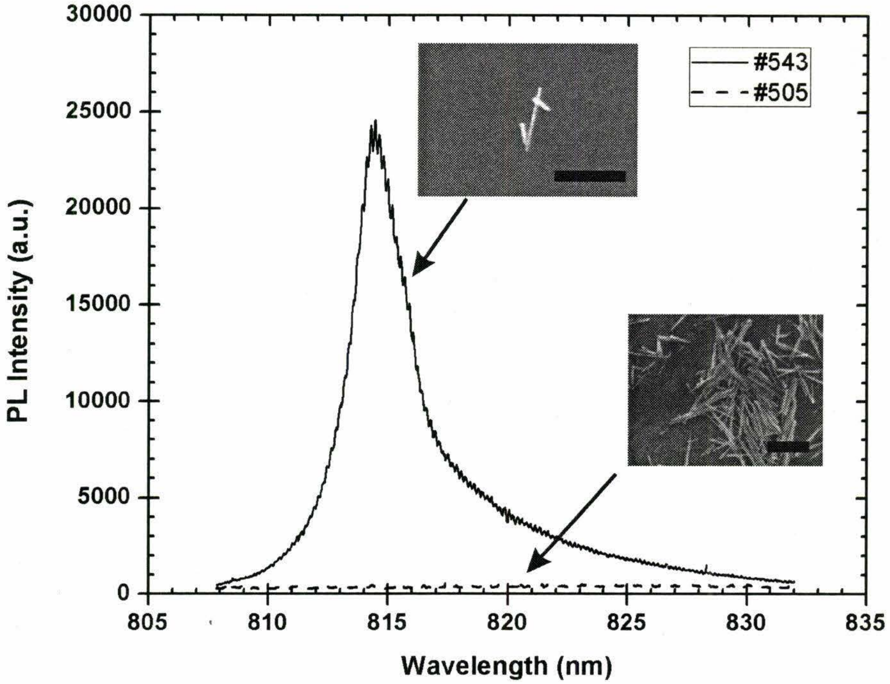

Figure 7.1: Low-temperature (7.3 K) photoluminescence from two sets of GaAs NWs having significantly different stacking fault density: sample #543 (solid line), with an average fault density of 0.008 nm^{-1}, and sample #505 (dashed line), with an average fault density > 0.2 nm^{-1}. Inset SEM images represent the NWs onto which the excitation laser was focused (scale bars represent 2 μm).

References

[1] M. Law, J. Goldberger, and P. D. Yang, Annual Rev. Mat. Res. **34**, 83 (2004).

[2] A. P. Levitt, *Introductory review*, 1–13, Whisker Technology, Wiley-Interscience, New York (1970).

[3] W. H. Sutton, *Principles and methods for fabricating whisker-reinforced composites*, 273–342, Whisker Technology, Wiley-Interscience, New York (1970).

[4] C. M. Lyon, C. M. Olson, and E. D. Lewis, Trans. Electrochem. Soc. **96**, 359 (1949).

[5] E. R. Johnson and J. A. Amick, J. Appl. Phys. **25**, 1204 (1954).

[6] F. C. Frank, Disc. Faraday Soc. **5**, 48 (1949).

[7] W. K. Burton, N. Cabrera, and F. C. Frank, Phil. Trans. Roy. Soc. Lond. A **243**, 299 (1951).

[8] G. W. Sears, Acta metallurgica **3**, 361 (1955).

[9] R. Gomer, J. Chem. Phys. **28**, 457 (1958).

[10] W. W. Webb and W. D. Forgeng, J. Appl. Phys. **28**, 1449 (1957).

[11] J. M. Blakely and K. A. Jackson, J. Chem. Phys. **37**, 428 (1962).

[12] V. Ruth and J. P. Hirth, J. Chem. Phys. **41**, 3139 (1964).

[13] W. W. Webb, *Dislocation structure of whiskers*, 230–237, Growth and perfection of crystals : proceedings, John Wiley and Sons, New York (1958).

[14] R. S. Wagner and W. C. Ellis, Appl. Phys. Lett. **4**, 89 (1964).

[15] R. S. Wagner, W. C. Ellis, K. A. Jackson, and S. M. Arnold, J. Appl. Phys. **35**, 2993 (1964).

[16] R. S. Wagner and W. C. Ellis, Trans. Metal. Soc. AIME **233**, 1053 (1965).

[17] E. I. Givargizov and A. A. Chernov, Kristallografiya **18**, 147 (1973).

[18] E. I. Givargizov, J. Cryst. Growth **31**, 20 (1975).

[19] K. Hiruma, T. Katsuyama, K. Ogawa, M. Koguchi, H. Kakibayashi, and G. P. Morgan, Appl. Phys. Lett. **59**, 431 (1991).

[20] M. Yazawa, M. Koguchi, A. Muto, M. Ozawa, and K. Hiruma, Appl. Phys. Lett. **61**, 2051 (1992).

[21] M. Koguchi, H. Kakibayashi, M. Yazawa, K. Hiruma, and T. Katsuyama, Jap. J. Appl. Phys. **31**, 2061 (1992).

[22] K. Hiruma, M. Yazawa, K. Haraguchi, K. Ogawa, T. Katsuyama, M. Koguchi, and H. Kakibayashi, J. Appl. Phys. **74**, 3162 (1993).

[23] K. Haraguchi, T. Katsuyama, and K. Hiruma, J. Appl. Phys. **75**, 4220 (1994).

[24] J. Westwater, D. P. Gosain, S. Tomiya, S. Usui, and H. Ruda, J. Vac. Sci. Technol. B **15**, 554 (1997).

[25] J. T. Hu, T. W. Odom, and C. M. Lieber, Acc. Chem. Res. **32**, 435 (1999).

[26] X. F. Duan and C. M. Lieber, Adv. Mat. **12**, 298 (2000).

[27] Y. Cui and C. M. Lieber, Science **291**, 851 (2001).

[28] M. S. Gudiksen, L. J. Lauhon, J. Wang, D. C. Smith, and C. M. Lieber, Nature **415**, 617 (2002).

[29] F. Qian, S. Gradecak, Y. Li, C. Y. Wen, and C. M. Lieber, Nano Lett. **5**, 2287 (2005).

[30] W. Lu and C. M. Lieber, Nature Mat. **6**, 841 (2007).

[31] M. T. Bjork, B. J. Ohlsson, T. Sass, A. I. Persson, C. Thelander, M. H. Magnusson, K. Deppert, L. R. Wallenberg, and L. Samuelson, Nano Lett. **2**, 87 (2002).

[32] K. A. Dick, K. Deppert, M. W. Larsson, T. Martensson, W. Seifert, L. R. Wallenberg, and L. Samuelson, Nature Mat. **3**, 380 (2004).

[33] A. Mikkelsen, N. Skold, L. Ouattara, M. Borgstrom, J. N. Andersen, L. Samuelson, W. Seifert, and E. Lundgren, Nature Mat. **3**, 519 (2004).

[34] A. I. Persson, M. W. Larsson, S. Stenstrom, B. J. Ohlsson, L. Samuelson, and L. R. Wallenberg, Nature Mat. **3**, 677 (2004).

[35] K. A. Dick, K. Deppert, L. S. Karlsson, L. R. Wallenberg, L. Samuelson, and W. Seifert, Adv. Funct. Mat. **15**, 1603 (2005).

[36] K. A. Dick, S. Kodambaka, M. C. Reuter, K. Deppert, L. Samuelson, W. Seifert, L. R. Wallenberg, and F. M. Ross, Nano Lett. **7**, 1817 (2007).

[37] Y. N. Xia, P. D. Yang, Y. G. Sun, Y. Y. Wu, B. Mayers, B. Gates, Y. D. Yin, F. Kim, and Y. Q. Yan, Adv. Mat. **15**, 353 (2003).

[38] N. Wang, Y. Cai, and R. Q. Zhang, Mat. Sci. Eng. R: Rep. **60**, 1 (2008).

[39] L. Brewer and J. S. Kane, J. Phys. Chem. **59**, 105 (1955).

[40] P. L. Edwards and R. J. J. Happel, J. Appl. Phys. **33**, 943 (1962).

[41] K. A. Dick, K. Deppert, T. Martensson, B. Mandl, L. Samuelson, and W. Seifert, Nano Lett. **5**, 761 (2005).

[42] S. A. Dayeh, E. T. Yu, and D. Wang, Nano Lett. **7**, 2486 (2007).

[43] J. L. Liu, S. J. Cai, G. L. Jin, S. G. Thomas, and K. L. Wang, J. Cryst. Growth **200**, 106 (1999).

[44] M. Ishida, T. Kawano, M. Futagawa, Y. Arai, H. Takao, and K. Sawada, Superlatt. Microstruc. **34**, 567 (2003).

[45] N. Wang, Y. F. Zhang, Y. H. Tang, C. S. Lee, and S. T. Lee, Appl. Phys. Lett. **73**, 3902 (1998).

[46] T. Y. Tan, S. T. Lee, and U. Gosele, Appl. Phys. A **74**, 423 (2002).

[47] W. Braun, V. M. Kaganer, A. Trampert, H. P. Schonherr, Q. Gong, R. Notzel, L. Daweritz, and K. H. Ploog, J. Cryst. Growth **227**, 51 (2001).

[48] J. E. Mahan, *Physical Vapor Deposition of Thin Films*, John Wiley & Sons, New York (2000).

[49] J. P. Hirth and G. M. Pound, J. Phys. Chem. **64**, 619 (1960).

[50] J. P. Hirth and G. M. Pound, Prog. Mat. Sci. **11**, 107 (1963).

[51] E. I. Givargizov, *Growth of whiskers by the vapor-liquid-solid mechanism*, 79–145, Current topics in materials science, vol.1, North-Holland (1978).

[52] V. G. Dubrovskii and N. V. Sibirev, Phys. Rev. E **70**, 031604 (2004).

[53] L. Schubert, P. Werner, N. D. Zakharov, G. Gerth, F. M. Kolb, L. Long, U. Gosele, and T. Y. Tan, Appl. Phys. Lett. **84**, 4968 (2004).

[54] M. C. Plante and R. R. LaPierre, J. Cryst. Growth **286**, 394 (2006).

[55] G. W. Sears, Acta Metallurgica **3**, 367 (1955).

[56] V. G. Dubrovskii, G. E. Cirlin, I. P. Soshnikov, A. A. Tonkikh, N. V. Sibirev, Y. B. Samsonenko, and V. M. Ustinov, Phys. Rev. B **71**, 205325 (2005).

[57] J. Johansson, C. P. T. Svensson, T. Martensson, L. Samuelson, and W. Seifert, J. Phys. Chem. B **109**, 13567 (2005).

[58] J. Johansson, B. A. Wacaser, K. A. Dick, and W. Seifert, Nanotechnology **17**, S355 (2006).

[59] V. G. Dubrovskii, N. V. Sibirev, G. E. Cirlin, J. C. Harmand, and V. M. Ustinov, Phys. Rev. E **73**, 021603 (2006).

[60] V. G. Dubrovskii and N. V. Sibirev, J. Cryst. Growth **304**, 504 (2007).

[61] L. R. Harriott, Proc. IEEE **89**, 366 (2001).

[62] I. Regolin, D. Sudfeld, S. Luttjohann, V. Khorenko, W. Prost, J. Kastner, G. Dumpich, C. Meier, A. Lorke, and F. J. Tegude, J. Cryst. Growth **298**, 607 (2007).

[63] T. Martensson, C. P. T. Svensson, B. A. Wacaser, M. W. Larsson, W. Seifert, K. Deppert, A. Gustafsson, L. R. Wallenberg, and L. Samuelson, Nano Lett. **4**, 1987 (2004).

[64] E. P. A. M. Bakkers, M. T. Borgstrom, and M. A. Verheijen, MRS Bull. **32**, 117 (2007).

[65] *http://www.itrs.net/reports.html.*

[66] T. Bryllert, L. E. Wernersson, T. Lowgren, and L. Samuelson, Nanotechnology **17**, S227 (2006).

[67] M. T. Bjork, B. J. Ohlsson, C. Thelander, A. I. Persson, K. Deppert, L. R. Wallenberg, and L. Samuelson, Appl. Phys. Lett. **81**, 4458 (2002).

[68] E. D. Minot, F. Kelkensberg, M. van Kouwen, J. A. van Dam, L. P. Kouwenhoven, V. Zwiller, M. T. Borgstrom, O. Wunnicke, M. A. Verheijen, and E. P. A. M. Bakkers, Nano Lett. **7**, 367 (2007).

[69] C. J. Barrelet, J. M. Bao, M. Loncar, H. G. Park, F. Capasso, and C. M. Lieber, Nano Lett. **6**, 11 (2006).

[70] T. J. Kempa, B. Tian, D. R. Kim, J. Hu, X. Zheng, and C. M. Lieber, Nano Lett. **8**, 3456 (2008).

[71] M. D. Kelzenberg, D. B. Turner-Evans, B. M. Kayes, M. A. Filler, M. C. Putnam, N. S. Lewis, and H. A. Atwater, Nano Lett. **8**, 710 (2008).

[72] F. Patolsky, B. P. Timko, G. F. Zheng, and C. M. Lieber, MRS Bull. **32**, 142 (2007).

[73] E. Stern, J. F. Klemic, D. A. Routenberg, P. N. Wyrembak, D. B. Turner-Evans, A. D. Hamilton, D. A. LaVan, T. M. Fahmy, and M. A. Reed, Nature **445**, 519 (2007).

[74] Y. F. Chan, X. F. Duan, S. K. Chan, I. K. Sou, X. X. Zhang, and N. Wang, Appl. Phys. Lett. **83**, 2665 (2003).

[75] D. M. Cornet and R. R. LaPierre, Nanotechnology **18**, 385305 (2007).

[76] M. Tchernycheva, G. E. Cirlin, G. Patriarche, L. Travers, V. Zwiller, U. Perinetti, and J.-C. Harmand, Nano Lett. **7**, 1500 (2007).

[77] M. Tchernycheva, L. Travers, G. Patriarche, F. Glas, J. C. Harmand, G. E. Cirlin, and V. G. Dubrovskii, J. Appl. Phys. **102**, 094313 (2007).

[78] A. I. Persson, M. T. Bjork, S. Jeppesen, J. B. Wagner, L. R. Wallenberg, and L. Samuelson, Nano Lett. **6**, 403 (2006).

[79] M. C. Plante, J. Garrett, S. C. Ghosh, P. Kruse, H. Schriemer, T. Hall, and R. R. LaPierre, Appl. Surf. Sci. **253**, 2348 (2006).

[80] M. C. Plante and R. R. LaPierre, J. Cryst. Growth **310**, 356 (2008).

[81] M. C. Plante and R. R. LaPierre, Nanotechnology **19**, 495603 (2008).

[82] C. Chen, M. C. Plante, C. Fradin, and R. R. LaPierre, J. Mat. Res. **21**, 2801 (2006).

[83] M. C. Plante and R. R. LaPierre, J. Appl. Phys. (submitted Nov. 2008) .

[84] S. Bhunia, T. Kawamura, Y. Watanabe, S. Fujikawa, and K. Tokushima, Appl. Phys. Lett. **83**, 3371 (2003).

[85] A. I. Hochbaum, R. Fan, R. R. He, and P. D. Yang, Nano Lett. **5**, 457 (2005).

[86] Z. H. Wu, X. Y. Mei, D. Kim, M. Blumin, and H. E. Ruda, Appl. Phys. Lett. **81**, 5177 (2002).

[87] T. Martensson, M. Borgstrom, W. Seifert, B. J. Ohlsson, and L. Samuelson, Nanotechnology **14**, 1255 (2003).

[88] M. H. Magnusson, K. Deppert, J.-O. Malm, J.-O. Bovin, and L. Samuelson, J. Nanopart. Res. **1**, 243 (1999).

[89] Y. C. Kang and S. B. Park, J. Aerosol Sci. **26**, 1131 (1995).

[90] H. Shtrikman, R. Popovitz-Biro, A. Kretinin, and M. Heiblum, Nano Lett. **9**, 215 (2009).

[91] *http://www.axt.com/.*

[92] *http://www.uvocs.com/.*

[93] G. Hollinger, R. Skheyta-Kabbani, and M. Gendry, Phys. Rev. B **49**, 11159 (1994).

[94] S. C. Ghosh, M. C. Biesinger, R. R. LaPierre, and P. Kruse, J. Appl. Phys. **101**, 114321 (2007).

[95] *http://rsb.info.nih.gov/ij/.*

[96] C. G. Granqvist and R. A. Buhrman, J. Catal. **42**, 477 (1976).

[97] A. K. Datye, Q. Xu, K. C. Kharas, and J. M. McCarty, Catal. Today **111**, 59 (2006).

[98] M. A. Herman, W. Richter, and H. Sitter, *Epitaxy: Physical Principles and Technical Implementation*, Springer, New York (2004).

[99] M. B. Panish, J. Electrochem. Soc. **127**, 2729 (1980).

[100] A. S. Jordan and A. Robertson, J. Vac. Sci. Technol. A **12**, 204 (1994).

[101] *http://www.svta.com/.*

[102] D. B. Williams and C. B. Carter, *Transmission electron microscopy : a textbook for materials science*, Plenum Press, New York (1996).

[103] *http://www.jeol.com/.*

[104] J. Goldstein, D. E. Newbury, P. Echlin, C. E. Lyman, D. C. Joy, E. Lifshin, L. Sawyer, and J. R. Michael, *Scanning electron microscopy and x-ray microanalysis*, Kluwer Academic/Plenum Publishers, New York (2003).

[105] *http://www.coleparmer.com/*.

[106] J. Johansson, L. S. Karlsson, C. P. T. Svensson, T. Martensson, B. A. Wacaser, K. Deppert, L. Samuelson, and W. Seifert, Nature Mater. **5**, 574 (2006).

[107] *Digitalmicrograph, version 1.71.38 (1996-2007), gatan inc., pleasantson, ca, usa, http://www.gatan.com/*.

[108] R. F. Egerton, *Physical principles of electron microscopy: an introduction to TEM, SEM, and AEM*, Springer Science+Business Media, Inc., New York (2007).

[109] *Inca microanalysis suite - issue 14, version 4.04 (1998-2003), oxford instruments analytical limited, http://www.oxford-instruments.com/*.

[110] S. Bhunia, T. Kawamura, S. Fujikawa, and Y. Watanabe, Physica E **24**, 138 (2004).

[111] Y. Nomura, Y. Morishita, S. Goto, Y. Katayama, and T. Isu, Appl. Phys. Lett. **64**, 1123 (1994).

[112] T. Shitara, E. Kondo, and T. Nishinaga, J. Cryst. Growth **99**, 530 (1990).

[113] H. Y. Wang and G. S. Fischman, J. Appl. Phys. **76**, 1557 (1994).

[114] A. I. Persson, B. J. Ohlsson, S. Jeppesen, and L. Samuelson, J. Cryst. Growth **272**, 167 (2004).

[115] K. Hiruma, M. Yazawa, T. Katsuyama, K. Ogawa, K. Haraguchi, M. Koguchi, and H. Kakibayashi, J. Appl. Phys. **77**, 447 (1995).

[116] J. H. Neave, P. J. Dobson, B. A. Joyce, and J. Zhang, Appl. Phys. Lett. **47**, 100 (1985).

[117] M. Tchernycheva, J. C. Harmand, G. Patriarche, L. Travers, and G. E. Cirlin, Nanotechnology **17**, 4025 (2006).

[118] M. Piccin, G. Bais, V. Grillo, F. Jabeen, S. D. Franceschi, E. Carlino, M. Lazzarino, F. Romanato, L. Businaro, S. Rubini, F. Martelli, and A. Franciosi, Physica E **37**, 134 (2007).

[119] R. Notzel, L. Daweritz, and K. Ploog, Phys. Rev. B **46**, 4736 (1992).

[120] K. Jacobi, L. Geelhaar, J. Marquez, J. Platen, and C. Setzer, Appl. Surf. Sci. **166**, 173 (2000).

[121] N. Skld, J. B. Wagner, G. Karlsson, T. Hernn, W. Seifert, M. E. Pistol, and L. Samuelson, Nano Lett. **6**, 2743 (2006).

[122] J. C. Harmand, G. Patriarche, N. Pr-Laperne, M. N. Mrat-Combes, L. Travers, and F. Glas, Appl. Phys. Lett. **87**, 203101 (2005).

[123] J. B. Hannon, S. Kodambaka, F. M. Ross, and R. M. Tromp, Nature **440**, 69 (2006).

[124] Q. H. Xiong, J. Wang, and P. C. Eklund, Nano Lett. **6**, 2736 (2006).

[125] Y. F. Hao, G. W. Meng, Z. L. Wang, C. H. Ye, and L. D. Zhang, Nano Lett. **6**, 1650 (2006).

[126] F. Glas, J.-C. Harmand, and G. Patriarche, Phys. Rev. Lett. **99**, 146101 (2007).

[127] S. Helveg, C. Lopez-Cartes, J. Sehested, P. L. Hansen, B. S. Clausen, J. R. Rostrup-Nielsen, F. Abild-Pedersen, and J. K. Norskov, Nature **427**, 426 (2004).

[128] V. G. Dubrovskii, I. P. Soshnikov, N. V. Sibirev, G. E. Cirlin, V. M. Ustinov, M. Tchernycheva, and J. C. Harmand, Semiconductors **41**, 865 (2007).

[129] V. G. Dubrovskii, N. V. Sibirev, R. A. Suris, G. E. Cirlin, J. C. Harmand, and V. M. Ustinov, Surf. Sci. **601**, 4395 (2007).

[130] F. Martelli, M. Piccin, G. Bais, F. Jabeen, S. Ambrosini, S. Rubini, and A. Franciosi, Nanotechnology **18**, 125603 (2007).

[131] B. Kalache, P. R. Cabarrocas, and A. F. Morral, Jap. J. Appl. Phys. **45**, L190 (2006).

[132] X. Q. Shen, D. Kishimoto, and T. Nishinaga, Jap. J. Appl. Phys. **33**, 11 (1994).

[133] C. Colombo, D. Spirkoska, M. Frimmer, G. Abstreiter, and A. F. I. Morral, Phys. Rev. B **77**, 155326 (2008).

[134] L. Geelhaar, C. Cheze, W. M. Weber, R. Averbeck, H. Riechert, T. Kehagias, P. Komninou, G. P. Dimitrakopulos, and T. Karakostas, Appl. Phys. Lett. **91**, 093113 (2007).

[135] M. Jeppsson, K. A. Dick, J. B. Wagner, P. Caroff, K. Deppert, L. Samuelson, and L.-E. Wernersson, J. of Cryst. Growth **310**, 4115 (2008).

[136] M. B. Panish and H. Temkin, *Gas Source Molecular Beam Epitaxy*, Springer-Verlag, Berlin and Heidelberg (1993).

[137] C. A. Verschuren, M. R. Leys, H. Vonk, and J. H. Wolter, Applied Physics Letters **74**, 2197 (1999).

[138] Y. Kim, H. J. Joyce, O. Gao, H. H. Tan, C. Jagadish, M. Paladugu, J. Zou, and A. A. Suvorova, Nano Letters **6**, 599 (2006).

[139] D. M. Cornet, *Characterization of InGaAs/InP heterostructure nanowires grown by gas source molecular beam epitaxy*, Master's thesis, McMaster University (2007).

[140] M. Paladugu, J. Zou, Y.-N. Guo, X. Zhang, Y. Kim, H. J. Joyce, Q. Gao, H. H. Tan, and C. Jagadish, Applied Physics Letters **93**, 101911 (2008).

[141] W. Seifert, M. Borgstrom, K. Deppert, K. A. Dick, J. Johansson, M. W. Larsson, T. Martensson, N. Skold, C. P. T. Svensson, B. A. Wacaser, L. R. Wallenberg, and L. Samuelson, J. Cryst. Growth **272**, 211 (2004).

[142] M. Borgstrom, K. Deppert, L. Samuelson, and W. Seifert, J. Cryst. Growth **260**, 18 (2004).

[143] L. Reimer, *Electron Scattering and Diffusion*, 57–127, Scanning Electron Microscopy - Physics of Image Formation and Microanalysis, Springer-Verlag, New York (1985).

[144] S. Bhunia, T. Kawamura, S. Fujikawa, H. Nakashima, K. Furukawa, K. Torimitsu, and Y. Watanabe, Thin Solid Films **464-65**, 244 (2004).

[145] B. J. Ohlsson, M. T. Bjork, A. I. Persson, C. Thelander, L. R. Wallenberg, M. H. Magnusson, K. Deppert, and L. Samuelson, Physica E **13**, 1126 (2002).

[146] M. J. Yacaman, J. A. Ascencio, H. B. Liu, and J. Gardea-Torresdey, J. Vac. Sci. Technol. B **19**, 1091 (2001).

[147] T. B. Massalski, *Binary Alloy Phase Diagrams*, volume 5, American Society for Metals, Metals Park, Ohio (1986).

[148] U. Krishnamachari, M. Borgstrom, B. J. Ohlsson, N. Panev, L. Samuelson, W. Seifert, M. W. Larsson, and L. R. Wallenberg, Appl. Phys. Lett. **85**, 2077 (2004).

[149] Z. H. Wu, X. Mei, D. Kim, M. Blumin, H. E. Ruda, J. Q. Liu, and K. L. Kavanagh, Appl. Phys. Lett. **83**, 3368 (2003).

[150] M. T. Bjork, B. J. Ohlsson, T. Sass, A. I. Persson, C. Thelander, M. H. Magnusson, K. Deppert, L. R. Wallenberg, and L. Samuelson, Appl. Phys. Lett. **80**, 1058 (2002).

[151] L. E. Jensen, M. T. Bjork, S. Jeppesen, A. I. Persson, B. J. Ohlsson, and L. Samuelson, Nano Lett. **4**, 1961 (2004).

[152] R. R. LaPierre, B. J. Robinson, and D. A. Thompson, J. Appl. Phys. **79**, 3021 (1996).

[153] M. Hata, T. Isu, A. Watanabe, Y. Kajikama, and Y. Katayama, J. Cryst. Growth **114**, 203 (1991).

[154] S. C. Shi, S. Chattopadhyay, C. F. Chen, K. H. Chen, and L. C. Chen, Chem. Phys. Lett. **418**, 152 (2006).

[155] M. A. Verheijen, G. Immink, T. de Smet, M. T. Borgstrom, and E. P. A. M. Bakkers, J. Am. Chem. Soc. **128**, 1353 (2006).

[156] D. J. Milliron, S. M. Hughes, Y. Cui, L. Manna, J. B. Li, L. W. Wang, and A. P. Alivisatos, Nature **430**, 190 (2004).

[157] I. P. Soshnikov, G. E. Tsyrlin, A. A. Tonkikh, Y. B. Samsonenko, V. B. Dubovskii, V. M. Ustinov, O. M. Gorbenko, D. Litvinov, and D. Gerthsen, Phys. Sol. State **47**, 2213 (2005).

[158] M. Paladugu, J. Zou, G. J. Auchterlonie, Y. N. Guo, Y. Kim, H. J. Joyce, Q. Gao, H. H. Tan, and C. Jagadish, Appl. Phys. Lett. **91**, 133115 (2007).

[159] *http://www2.uca.es/grup-invest/sic/straintool.htm.*

[160] *http://www.hremresearch.com/eng/plugin/gpaeng.html.*

[161] M. Paladugu, J. Zou, Y.-N. Guo, Q. Gao, H. H. Tan, C. Jagadish, and Y. Kim, Small **3**, 1873 (2007).

[162] X. L. Chen, Y. C. Lan, J. Y. Li, Y. G. Cao, and M. He, J. Cryst. Growth **222**, 586 (2001).

[163] V. G. Dubrovskii, N. V. Sibirev, G. E. Cirlin, M. Tchernycheva, J. C. Harmand, and V. M. Ustinov, Phys. Rev. E **77**, 031606 (2008).

[164] R. L. Schwoebel and E. J. Shipsey, J. Appl. Phys. **37**, 3682 (1966).

[165] R. L. Schwoebel, J. Appl. Phys. **40**, 614 (1969).

[166] G. Ehrlich and F. G. Hudda, J. Chem. Phys. **44**, 1039 (1966).

[167] K. N. Tu, J. W. Mayer, and L. C. Feldman, *Electronic thin film science for engineers and materials scientists*, Macmillan Publishing Company, New York (1992).

[168] V. G. Dubrovskii, N. V. Sibirev, R. A. Suris, G. E. Cirlin, V. M. Ustinov, M. Tchernysheva, and J. C. Harmand, Semiconductors **40**, 1075 (2006).

[169] D. Kincaid and W. Cheney, *Numerical Analysis: Mathematics of Scientific Computing (2nd ed.)*, Brooks/Cole Publishing Company, Pacific Grove, CA (1996).

[170] R. R. LaPierre, B. J. Robinson, and D. A. Thompson, J. Cryst. Growth **191**, 319 (1998).

[171] M. Ohring, *The Materials Science of Thin Films*, Academic Press, San Diego (1992).

[172] S. Neretina, R. A. Hughes, J. F. Britten, N. V. Sochinskii, J. S. Preston, and P. Mascher, Nanotechnology **18**, 275301 (2007).